Master's Thesis

Unpaired Majorana Fermions in Disordered p-wave Superconductor and Random Matrix Theory

Esben Bork Hansen

Supervisors: Prof. Karsten Flensberg, Ass. Prof. Kim Splittorff and Prof. Poul Henrik Damgaard

Center for Quantum Devices, Niels Bohr Institute
University of Copenhagen

22 September 2014

Abstract

Hamiltonians describing topological insulator and superconductor systems can like random matrices ensembles from random matrix theory be classified into the ten Altland-Zirnbauer symmetry classes. Hamiltonians which exhibits a number of unpaired zero-energy Majorana states share symmetry class with a random matrix ensemble with an equal number of zero eigenvalues. In this thesis, we show that a one-dimensional p-wave superconductor Hamiltonian is able to host unpaired Majorana bound states. Two numerical models of the p-wave Hamiltonian are presented, and disorder effects on the the Majorana bound states are examined. We show that the p-wave Hamiltonian belongs to the BDI symmetry class and attempt to design an equivalent random matrix description of the Majorana physics. We observe a compelling similarity between the average spectral density of the p-wave models and the proposed random matrix models. We believe it is possible to eliminate the remaining discrepancies by finding a more suitable random matrix model.

Acknowledgements

First and foremost, I would like to thank my supervisors Prof. Karsten Flensberg, Ass.Prof. Kim Splittorff and Prof. Poul Henrik Damgaard. Part of the project has been to build a bridge of understanding from condended matter theory at the HCØ to random matrix theory at NBI and would not have been possible without the commitment of all three of you.
I thank the entire condenced matter theory group for providing a great work environment and making me feel like a part of the research group.
Special thanks goes to Samuel Alejandro Sanchez Viveros, Konrad Udo Hannes Wölms, Anine Laura Borger and Marius Folden Simonsen for corrections and feedback on my thesis manuscript.
Jeg vil desuden takke mine samboer for at have udholdt at have en frustreret specialeskriver boende.
Tak til min familie for at bære over med mit fravær i min tid som travl studerende.
En helt særlig tak til Anine, der med sit gode selskab paa kontoret har gjort de uudholdelige perioder i specialeskrivningen udholdelige.

Esben Bork Hansen
Center for Quantum Devices, Niels Bohr Institute
University of Copenhagen
22 September 2014

Contents

Chapter 1

Introduction

It has been proposed that fault tolerant quantum computations can be carried out by braiding operations of anyons with non-abelian statistics[1]. (Abelian) Anyons are particles with the property that upon exchange of two anyons, the global wave function acquire a phase factor $e^{i\theta}$. Unlike fermions and bosons which acquire a phase factor of -1 and $+1$ respectively upon exchange, the anyons can acquire any phase[2]. In certain systems with (non-abelian) anyons, the exchange of two anyons results not only in a change of phase in the wavefunction but also in a change of the internal state of the modes. This type of anyons are called non-abelian due to the fact that exchange operations of different non-abelian anyons in general do not commute. The non-abelian nature of these anyons arises from the degenerateness of the ground state. A ground state can be transformed into a different ground state through a process of adiabatically moving non-abelian anyons around each other. This is called braiding. Quantum computations can then be performed through a series of braiding operations involving several anyons, and measurements are performed by joining pairs of anyons[1].

Quasi-particle excitations called Majorana fermions or Majorana bound states with such non-abelian anyonic properties have been suggested to exist in certain condensed matter systems[3]. In particle physics, Majorana fermions are particles which are their own anti-particle meaning that the creation operator $a^\dagger$ of a Majorana fermion is equal to its hermitian conjugate a and therefore has to be real valued. The existence of elementary particle Majorana fermions is still undecided, but quasi-particle excitations with the same properties are proposed to exist in certain topological superconductor systems[3]. Generally, any fermion operator $c_j^\dagger$ can be written in terms of two real valued Majorana operators

$$c_j^\dagger = \tfrac{1}{2}(a_{j,1}^\dagger - i a_{j,2}) \ , \qquad c_j = \tfrac{1}{2}(a_{j,1}^\dagger + i a_{j,2}), \tag{1.1}$$

$$a_{j,1}^\dagger = c_j^\dagger + c_j = a_{j,1} \ , \qquad a_{j,2}^\dagger = i(c_j^\dagger - c_j) = a_{j,2}, \tag{1.2}$$

which means that the Majorana operators are just the real and imaginary part of a fermion operator split into two[4]. The Majorana fermions therefore only carry half a degree of freedom each, and even though they satisfy fermion anti-commutation relations

$$\{a_{j,k} \, , \, a_{j',k'}^\dagger\} = 2\delta_{j,j'}\delta_{k,k'}, \tag{1.3}$$

they do not obey the usual Pauli principle of fermions due to $a_{j,k}^\dagger = a_{j,k}$. Instead, the Majorana operators have the property

$$a_{j,k}^\dagger a_{j,k} = (a_{j,k})^2 = 1. \tag{1.4}$$

In this sense a Majorana state is always filled and always empty and counting does not make sense. The non-abelian feature of these Majorana modes comes about when there exists a fermionic state which it costs no (or very little) additional energy to occupy. This leads to a degenerate ground state which must be separated from all other excited states by an energy gap. The ground states are still fermionic states with a definite number of fermions and can be distinguished by their fermion occupation number.

Usually, the spatial distribution of the real and imaginary part of a fermionic state are predominantly overlapping, but it only becomes interesting from a Majorana perspective when a fermion is comprised of two spatially separated Majorana fermions. Such a highly delocalized fermionic state will be protected from most types of decoherence since it cannot be altered by local perturbations affecting only one of its constitutive Majorana fermions. It is these spatially separated Majorana fermions we refer to when we use the term Majorana fermion.This protected fermionic state can be manipulated through the physical exchange of Majorana fermions due to their non-abelian nature. This is the founding idea for low-decoherence topological quantum computation[5].

Non-interacting fermionic systems can be classified according to their symmetries in a scheme consisting of ten symmetry classes[6, 7]. Some of these systems have non-trivial topological ground states depending on the symmetries and the dimension of the system[8]. The term "topology" or "topological" refers to a property of the system called a topological invariant which is invariant under smooth changes of the system parameters. One example of such a topological invariant is the presence of Majorana fermions. Majorana fermions however are not present throughout the entire parameter space, but only in a restricted part. This domain is called the topological non-trivial phase. In the topological non-trivial phase any smooth changes of parameters will not affect the Majorana states until a topological phase transition occurs, after which the system will be in a different topological phase with a different ground state. Majorana bound states are located at the physical boundary of the topological phase, and manipulations of the Majorana states can be performed by altering the shape of the topological phase.

Two physical systems that are suggested to host Majorana fermions are the one-dimensional spinless p-wave superconductor and the two-dimensional $p_x \pm ip_y$ superconductor. Such superconductors however are not readily available in nature or laboratory, but it has been shown that strong topological insulators brought in tunneling contact with an s-wave superconductor effectively exhibit the required p-wave pairing[9].
In the two-dimensional $p_x \pm ip_y$ superconductor the Majorana fermions are bound to topological defects at vortices in the superconductor [10]. It has been proposed that the system can be realized by placing a thin (effectively two-dimensional) topological insulator on top of an s-wave superconductor[9].
In the one-dimensional spinless p-wave superconductor the Majorana fermions will be located at the ends of the topological phase[11], and quantum computations can be done using a network of these quantum wires where Majorana fermions are braided by moving them around in the network[12]. A possible realization of such a system is proposed to be a (one-dimensional) semiconductor quantum wire with strong spin-orbit coupling and proximity induced s-wave pairing subject to a magnetic field orthogonal to the spin-orbit vector [13].

As mentioned, the fermionic state consisting of spatially separated Majorana fermions will be protected from weak local disorder induced decoherence. Stronger disorder, however, will cause the constituent Majorana fermions to hybridize when the overlap between their wavefunctions increase and their energy becomes non-zero. This is accompanied by a closing

of the superconducting energy gap and disruption of the degenerate ground state[14].
One of the main signatures of Majorana fermions is a zero energy mode inside the superconducting gap. There has been observations of a zero bias peak in the differential conduction at zero voltage which is believed to be a signature of Majorana fermions[15]. Zero energy modes however can also originate from different mechanisms such as Griffith effects[16] and Andreev bound states[17]. Disorder and finite temperature effects make it difficult to determine the mechanism behind the observed zero energy modes.

The properties of Majorana fermions are to a large extent independent of the system parameters as long as the system is in a topological non-trivial phase where Majorana fermions exist. Similar features are also seen in the theory of random matrices.
Random matrix theory is the study of random matrices and their statistical properties. Say we consider a random matrix which possesses certain symmetries, *i.e.* the matrix is invariant under a transformation that is unitary, orthorgonal or symplectic, just to name a few. The matrix is classified into one of the 10 universal symmetry classes corresponding to the symmetries of the matrix[7, 6]. The elements of the matrix are random variables of a given probability distribution.
There can then be found certain universal statistical properties of the eigenvalues of the matrix closest to zero and their corresponding eigenvectors. In the case of a large matrix, these properties will to a large extent be independent of the given probability distribution and only depend on the symmetries of the matrix[18]. These universal properties include the distribution of eigenvalues close to zero and the number of zero eigenvalues of the matrix.

Hamiltonians of non-interacting fermion systems can also be classified by one of the 10 universal symmetry classes according to the symmetries of the Hamiltonian[8]. Among these Hamiltonians are those describing topological insulator and superconductor systems, some of which exhibits zero energy Majorana fermions. It is therefore natural to ask if there exists random matrix models able to describe the Majorana physics observed in certain topological condensed matter systems.

1.1 Outline

In this thesis we will attempt to construct a random matrix model that is able to describe the Majorana physics of a disordered one-dimensional spinless p-wave superconductor. We derive a low-energy effective model for the Hamiltonian of the one-dimensional semiconductor-superconductor quantum wire system mentioned above. This effective model will be equivalent to the Hamiltonian of a one-dimensional spinless p-wave superconductor.

In chapter 2 we will investigate the topological properties of this model and show that it can host zero-energy bound edge modes. We will not be concerned with proving the non-abelian nature of these zero-energy modes but assume that they are the Majorana fermions we are interested in.
In chapter 3 we construct two numerical models of the p-wave Hamiltonian and examine the behaviour of the zero-energy mode in these models. So far the models are non-disordered but in chapter 4 we implement disorder and examine how it affects the zero-energy modes.
In chapter 5 we will discuss the connections between topological condensed matter systems and random matrix theory. We investigate the possibility of constructing a random matrix model with zero-modes corresponding to the Majorana modes of the disordered p-wave Hamiltonian. Two random matrix models are proposed and compared to the numerical p-wave Hamiltonian models.

1.2 The effective p-wave Hamiltonian

As part of the introduction we will derive a low-energy effective Hamiltonian of the Hamiltonian model of the semiconductor-superconductor quantum wire system mentioned above. The effective low-energy model will be equivalent to the Hamiltonian describing a p-wave superconductor which is a simpler model, but still captures the Majorana physics we are interested in.

A one dimensional system with strong spin-orbit coupling, s-wave superconductor pairing and Zeeman field can in theory exhibit unpaired Majorana fermions (MF) [13]. This system can be realised by a semiconductor quantum wire with a strong Rashba spin-orbit coupling, brought in tunneling contact with an s-wave superconductor and subject to a magnetic field. Possible signatures of MFs have been observed in this system [15].
The original model could be analyzed by the same methods that we will use on the effective low-energy model. The effective low-energy model is however much simpler because it depends on fewer parameters and has a simpler gap closing mechanism, and features the same physics as the original model. We will therefore work with this simpler effective model to explore the possibility of finding a correspondence to random matrix theory.

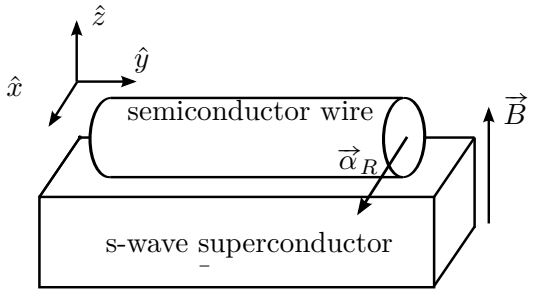

Figure 1.1: Simple illustration of the semiconductor-superconductor quantum wire system. The nano wire is placed in tunneling contact with the s-wave superconductor in the y-direction and the magnetic field B is applied in the z-direction perpendicular to the Rashba spin-orbit vector α_R which points in the x-direction.

The Hamiltonian of the quantum wire consists of four terms [13]:

$$H = H_{\text{kin}} + H_{\text{SO}} + H_{\text{Z}} + H_{\text{SC}}. \tag{1.5}$$

The first term is the kinetic energy and chemical potential, the second a Rashba spin-orbit term, the third a Zeeman term, and the fourth an s-wave pairing term. We place the wire in the y-direction and the magnetic field in the z-direction, such that the spin-orbit coupling is in the x-direction as illustrated in the figure 1.1. The four parts of the Hamiltonian are:

- The kinetic energy and chemical potential term

$$H_{\text{kin}} = \sum_{\sigma} \int \psi_{\sigma}^{\dagger}(y) \left(\frac{(-i\hbar\partial_y)^2}{2m} - \mu \right) \psi_{\sigma}(y) \, \mathrm{d}y, \tag{1.6}$$

  where m is the effective electron mass and μ is the chemical potential. The operator $\psi_{\sigma}^{\dagger}(y)$ creates an electron of spin $\sigma = \uparrow / \downarrow$ at position y.

- The spin-orbit term

$$H_{\mathrm{SO}} = -i\alpha_R\hbar \sum_{\sigma,\sigma'} \int \psi^\dagger_\sigma(y)(\sigma_x)_{\sigma\sigma'}\partial_y\psi_{\sigma'}(y)\,\mathrm{d}y, \tag{1.7}$$

  where α_R is the Rashba spin-orbit coupling, $\sigma_{x,y,z}$ are the Pauli matrices, and the x-axis is chosen to lie along the spin-orbit vector.

- The Zeeman term arising from the B-field along the z-axis

$$H_{\mathrm{Z}} = \Delta_Z \sum_{\sigma,\sigma'} \int \psi^\dagger_\sigma(y)(\sigma_z)_{\sigma\sigma'}\psi_{\sigma'}(y)\,\mathrm{d}y, \tag{1.8}$$

  where $\Delta_Z = \frac{g\mu_B B}{2}$ is the Zeeman energy, g is the Landé factor and μ_B is the Bohr magneton.

- The term from the s-wave BCS Hamiltonian is

$$H_{\mathrm{SC}} = \frac{1}{2}\Delta_{SC} \sum_{\sigma,\sigma'} \int \psi^\dagger_\sigma(y)(i\sigma_y)_{\sigma\sigma'}\psi^\dagger_{\sigma'}(y) + \mathrm{h.c.}\,\mathrm{d}y, \tag{1.9}$$

  where we assume that the proximity induced superconductivity gap Δ_{SC} is real. Otherwise it can be made real by a global gauge transformation $\psi_\sigma(y) \to \psi_\sigma(y)e^{-i\frac{\theta}{2}}$ where $\Delta_{SC} \to e^{i\theta}\Delta_{SC}$ since we consider only a single superconductor.

The Hamiltonian can be written in a more compact form by introducing Nambu spinors:

$$\begin{aligned} H &= \frac{1}{2}\int \Psi^\dagger(y)\,\mathcal{H}\Psi(y)\;\mathrm{d}y\,, \qquad \Psi^\dagger = \left(\psi^\dagger_\uparrow, \psi^\dagger_\downarrow, \psi_\downarrow, -\psi_\uparrow\right), \\ \mathcal{H} &= \left(\frac{-\hbar^2\partial_y^2}{2m} - \mu\right)\tau_z - i\alpha_R\hbar\partial_y\tau_z\sigma_x + \Delta_Z\sigma_z + \Delta_{SC}\tau_x. \end{aligned} \tag{1.10}$$

Here the Pauli matrices σ and τ operate in spin and particle-hole space respectively. Δ_Z, μ, α_R and Δ_{SC} could vary over the length of the chain, but we will at present assume them to be constant. For a translational invariant system, we Fourier transform to momentum basis and obtain the energy spectrum by squaring $\mathcal{H}$:

$$\begin{aligned} (E(k))^2 &= \left(\xi_k\tau_z + \alpha_R\hbar k\tau_z\sigma_x + \Delta_Z\sigma_z + \Delta_{SC}\tau_x\right)^2 \\ &= \xi_k^2 + (\alpha_R\hbar k)^2 + \Delta_Z^2 + \Delta_{SC}^2 + 2\left(\xi_k(\alpha_R\hbar k)\sigma_x + \xi_k\Delta_Z\tau_z\sigma_z + \Delta_Z\Delta_{SC}\tau_x\sigma_z\right) \\ &\qquad + (\alpha_R\hbar k)\Delta_Z\tau_z\left\{\sigma_z,\sigma_x\right\} + (\alpha_R\hbar k)\Delta_{SC}\left\{\tau_x,\tau_x\right\}\sigma_x + \xi_k\Delta_{SC}\left\{\tau_z,\tau_x\right\} \\ &= \xi_k^2 + (\alpha_R\hbar k)^2 + \Delta_Z^2 + \Delta_{SC}^2 + 2\left(\xi_k(\alpha_R\hbar k)\sigma_x + \xi_k\Delta_Z\tau_z\sigma_z + \Delta_Z\Delta_{SC}\tau_x\sigma_z\right). \end{aligned} \tag{1.11}$$

where k is the wave number and we have defined $\xi_k = \frac{\hbar^2k^2}{2m} - \mu$. The last three terms in the bracket still contain τ and σ matrices but these can be removed by writing the terms containing them as:

$$\begin{aligned} (E_\pm(k))^2 &= \xi_k^2 + (\alpha_R\hbar k)^2 + \Delta_Z^2 + \Delta_{SC}^2 \pm 2\sqrt{\left[\xi_k(\alpha_R\hbar k)\sigma_x + \xi_k\Delta_Z\tau_z\sigma_z + \Delta_Z\Delta_{SC}\tau_x\sigma_z\right]^2} \\ &= \xi_k^2 + (\alpha_R\hbar k)^2 + \Delta_Z^2 + \Delta_{SC}^2 \pm 2\Big[\xi_k^2(\alpha_R\hbar k)^2 + \xi_k^2\Delta_Z^2 + \Delta_Z^2\Delta_{SC}^2 \\ &\qquad + \left[\xi_k^2(\alpha_R\hbar k)\Delta_Z\tau_z + \xi_k(\alpha_R\hbar k)\Delta_Z\Delta_{SC}\tau_x\right]\left\{\sigma_z,\sigma_x\right\} + \xi_k\Delta_Z^2\Delta_{SC}\left\{\tau_z,\tau_x\right\}\sigma_z\Big]^{\frac{1}{2}} \\ &= \xi_k^2 + (\alpha_R\hbar k)^2 + \Delta_Z^2 + \Delta_{SC}^2 \pm 2\sqrt{\xi_k^2(\alpha_R\hbar k)^2 + \xi_k^2\Delta_Z^2 + \Delta_Z^2\Delta_{SC}^2}. \end{aligned} \tag{1.12}$$

The $\pm$ comes from the rewriting "terms" $= \pm\sqrt{[\text{"terms"}]^2}$. We used the anti-commutation relations of the Pauli matrices $\{\sigma_i, \sigma_j\} = \{\tau_i, \tau_j\} = 2\delta_{ij}$.

The dispersion relation is illustrated in five cases in figure 1.2. The energy spectrum $E_-(k)$ is gapped for all k when $\Delta_Z, \Delta_{SC}, \alpha_R \neq 0$ except if $\Delta_Z^2 = \Delta_{SC}^2 + \mu^2$ where the energy gap closes at $k = 0$. We mention (even though it is not our main focus at the moment) that the system goes through a topological phase transition at $\Delta_Z^2 = \Delta_{SC}^2 + \mu^2$[13]. For $\Delta_Z^2 > \Delta_{SC}^2 + \mu^2$, the system is in a topological non-trivial phase where zero energy bound states also known as MFs exists at the ends of the wire. When $\Delta_Z^2 < \Delta_{SC}^2 + \mu^2$, the system is in the topological trivial phase where no MFs exist in the wire. We will elaborate more on topological phases in chapter 2.
Figure 1.2 illustrates how an effective spin-polarized Hamiltonian can describe the low energy physics when the chemical potential can be placed between the two bands.

We will now show that for a certain range of parameters this model becomes an effective spinless p-wave superconductor in the low energy limit. In momentum space, the Hamiltonian takes the form

$$H = \frac{1}{2}\int \mathbf{c}_p^\dagger \mathscr{H} \mathbf{c}_p \, \mathrm{d}p; \qquad \mathbf{c}_p^\dagger = \left(c_{p\uparrow}^\dagger, c_{p\downarrow}^\dagger, c_{-p\uparrow}, c_{-p\downarrow}\right) \tag{1.13}$$

$$\begin{aligned}\mathscr{H} &= \xi_p \tau_z\sigma_0 + \alpha_R p \tau_0\sigma_x + \Delta_Z \tau_0\sigma_z + \Delta_{SC}\tau_y\sigma_y \\ &= \begin{bmatrix} \xi_p\sigma_0 + \alpha_R p\sigma_x + \Delta_Z\sigma_z & \Delta_{SC}(i\sigma_y) \\ -\Delta_{SC}(i\sigma_y) & -\xi_p\sigma_0 + \alpha_R p\sigma_x - \Delta_Z\sigma_z \end{bmatrix},\end{aligned} \tag{1.14}$$

where $-i\hbar\partial_y \to p$, and we have rearranged the order of the operators in the Nambu spinor such that the kinetic term, spin-orbit term and Zeemann term are diagonal in particle-hole space (the τ-matrices).

We start by considering the non-superconducting case of $\Delta_{SC} = 0$ where the Hamiltonian can be diagonalized straight forwardly. Then we "turn on" Δ_{SC} as a small perturbation and find the domain where the Hamiltonian is spin-polarized. When $\Delta_{SC} = 0$, the Hamiltonian reduces to

$$H = (c_{p\uparrow}^\dagger, c_{p\downarrow}^\dagger)\mathscr{H}\begin{pmatrix} c_{p\uparrow} \\ c_{p\downarrow} \end{pmatrix} \tag{1.15}$$

$$\mathscr{H} = \begin{bmatrix} \xi_p + \Delta_Z & \alpha_R p \\ \alpha_R p & \xi_p - \Delta_Z \end{bmatrix} = \xi_p\sigma_0 + \alpha_R p\sigma_x + \Delta_Z\sigma_z. \tag{1.16}$$

This Hamiltonian has the dispersion relation $E_{n,\pm}(p) = \xi_p \pm \sqrt{(\alpha_R p)^2 + \Delta_Z^2}$ and can be diagonalized by the unitary transformation

$$\mathcal{U} = \begin{bmatrix} \cos\frac{\theta}{2} & \sin\frac{\theta}{2} \\ -\sin\frac{\theta}{2} & \cos\frac{\theta}{2} \end{bmatrix} = \sigma_0\cos\tfrac{\theta}{2} + i\sigma_y\sin\tfrac{\theta}{2} \tag{1.17}$$

where $\tan(\theta) = \frac{\alpha_R p}{\Delta_Z}$, and the new spinors are $(c_{p+}, c_{p-})^T = (c_{p\uparrow}, c_{p\downarrow})\mathcal{U}^\dagger$ and $(c_{p+}^\dagger, c_{p-}^\dagger) = \mathcal{U}(c_{p\uparrow}^\dagger, c_{p\downarrow}^\dagger)$. We now go back to the original Hamiltonian with $\Delta_{SC} \neq 0$ and write it in terms of these spinors, $\tilde{\mathbf{c}}_p^\dagger = (c_{p+}^\dagger, c_{p-}^\dagger, c_{-p+}, c_{-p-})$. We have

$$H = \tfrac{1}{2}\tilde{\mathbf{c}}_p^\dagger \widetilde{\mathscr{H}} \tilde{\mathbf{c}}_p, \tag{1.18}$$

where

$$\widetilde{\mathscr{H}} = \begin{bmatrix} \mathcal{U}(\xi_p\sigma_0 + \alpha_R p\sigma_x + \Delta_Z\sigma_z)\mathcal{U}^\dagger & \mathcal{U}(\Delta_{SC}(i\sigma_y))\mathcal{U} \\ \mathcal{U}^\dagger(-\Delta_{SC}(i\sigma_y))\mathcal{U}^\dagger & \mathcal{U}^\dagger(-\xi_p\sigma_0 + \alpha_R p\sigma_x - \Delta_Z\sigma_z)\mathcal{U} \end{bmatrix}$$
$$= \begin{bmatrix} \overline{\overline{A}} & \overline{\overline{B}} \\ \overline{\overline{C}} & \overline{\overline{D}} \end{bmatrix}. \tag{1.19}$$

$\overline{\overline{A}}$, $\overline{\overline{B}}$, $\overline{\overline{C}}$ and $\overline{\overline{D}}$ are 2×2 matrices which we simplify using

$$\cos\theta = \cos\arctan\frac{\alpha_R p}{\Delta_Z} = \frac{\Delta_Z}{\sqrt{\Delta_Z^2 + (\alpha_R p)^2}} \tag{1.20}$$

and

$$\sin\theta = \sin\arctan\frac{\alpha_R p}{\Delta_Z} = \frac{\alpha_R p}{\sqrt{\Delta_Z^2 + (\alpha_R p)^2}}. \tag{1.21}$$

The matrices $\overline{\overline{A}}$, $\overline{\overline{B}}$, $\overline{\overline{C}}$ and $\overline{\overline{D}}$ are

$$\begin{aligned} \overline{\overline{A}} &= \xi_p\sigma_0 + \alpha_R p(\sigma_x\cos\theta + \sigma_z\sin\theta) + \Delta_Z(\sigma_z\cos\theta - \sigma_x\sin\theta) \\ &= \xi_p\sigma_0 + \alpha_R p\sigma_z\sin\theta + \Delta_Z\sigma_z\cos\theta \\ &= \xi_p\sigma_0 + \frac{(\alpha_R p)^2 + \Delta_Z^2}{\sqrt{\Delta_Z^2 + (\alpha_R p)^2}}\sigma_z \\ &= \xi_p\sigma_0 + \sqrt{\Delta_Z^2 + (\alpha_R p)^2}\sigma_z \end{aligned} \tag{1.22}$$

$$\begin{aligned} \overline{\overline{B}} &= \Delta_{SC}((i\sigma_y)\cos\theta - \sigma_0\sin\theta) \\ &= \frac{\Delta_{SC}}{\sqrt{\Delta_Z^2 + (\alpha_R p)^2}}(\Delta_Z(i\sigma_y) - \alpha_R p\sigma_0) \end{aligned} \tag{1.23}$$

$$\begin{aligned} \overline{\overline{C}} &= -\Delta_{SC}((i\sigma_y)\cos\theta + \sigma_0\sin\theta)) \\ &= -\frac{\Delta_{SC}}{\sqrt{\Delta_Z^2 + (\alpha_R p)^2}}(\Delta_Z(i\sigma_y) + \alpha_R p\sigma_0) = \overline{\overline{B}}^T \end{aligned} \tag{1.24}$$

$$\begin{aligned} \overline{\overline{D}} &= -\xi_p\sigma_0 + \alpha_R p(\sigma_x\cos\theta + \sigma_z\sin\theta) - \Delta_Z(\sigma_z\cos\theta - \sigma_x\sin\theta) \\ &= -\xi_p\sigma_0 - \alpha_R p\sigma_z\sin\theta - \Delta_Z\sigma_z\cos\theta \\ &= -\xi_p\sigma_0 - \frac{(\alpha_R p)^2 + \Delta_Z^2}{\sqrt{\Delta_Z^2 + (\alpha_R p)^2}}\sigma_z \\ &= -\xi_p\sigma_0 - \sqrt{\Delta_Z^2 + (\alpha_R p)^2}\sigma_z = -\overline{\overline{A}}. \end{aligned} \tag{1.25}$$

We insert the matrices $\overline{\overline{A}}$, $\overline{\overline{B}}$, $\overline{\overline{C}}$ and $\overline{\overline{D}}$ in eq. (1.19) and rotate the Nambu spinor to $(c_{p-},\ c^\dagger_{-p-},\ c_{p+},\ c^\dagger_{-p+})$, such that the low energy band is described in four elements in the

upper left corner (marked with red):

$$\widetilde{\mathscr{H}} = \begin{bmatrix} \xi_p - \beta(p) & -\Delta_{SC}\alpha_R p\beta^{-1}(p) & 0 & \Delta_{SC}\Delta_Z\beta^{-1}(p) \\ -\Delta_{SC}\alpha_R p\beta^{-1}(p) & -\xi_p + \beta(p) & -\Delta_{SC}\Delta_Z\beta^{-1}(p) & 0 \\ 0 & -\Delta_{SC}\Delta_Z\beta^{-1}(p) & \xi_p + \beta(p) & -\Delta_{SC}\alpha_R p\beta^{-1}(p) \\ \Delta_{SC}\Delta_Z\beta^{-1}(p) & 0 & -\Delta_{SC}\alpha_R p\beta^{-1}(p) & -\xi_p - \beta(p) \end{bmatrix}, \tag{1.26}$$

where $\beta = \sqrt{\Delta_Z^2 + (\alpha_R p)^2}$.

When $\Delta_Z \gg E_{SO}, \Delta_{SC}$, where $E_{SO} = \frac{m\alpha_R^2}{2}$ is the spin-orbit energy, the states in the lower and upper band are spin polarized. We write the Hamiltonian in eq. (1.26) on the same form as in eq. (1.19):

$$\widetilde{\mathscr{H}} = \begin{bmatrix} \widetilde{\mathscr{H}}_{--} & \widetilde{\mathscr{H}}_{-+} \\ \widetilde{\mathscr{H}}_{+-} & \widetilde{\mathscr{H}}_{++} \end{bmatrix}. \tag{1.27}$$

The lower band is described by the matrix $\widetilde{\mathscr{H}}_{--}$ and the upper band by $\widetilde{\mathscr{H}}_{++}$ while $\widetilde{\mathscr{H}}_{+-}$ and $\widetilde{\mathscr{H}}_{-+}$ describe the interaction between states in different bands.
In the limit $\Delta_Z \gg E_{SO}, \Delta_{SC}$ only states in the lower band are occupied for $\mu < 2\Delta_Z$, and we can construct a effective low energy Hamiltonian

$$\widetilde{\mathscr{H}}_{--} \approx \begin{bmatrix} \xi_p - \Delta_Z & -\alpha_R p\frac{\Delta_{SC}}{\Delta_Z} \\ -\alpha_R p\frac{\Delta_{SC}}{\Delta_Z} & -\xi_p + \Delta_Z \end{bmatrix} \tag{1.28}$$

$$= \begin{bmatrix} \frac{p^2}{2m} - \mu^* & p\Delta_{SC}^* \\ p\Delta_{SC}^* & -\frac{p^2}{2m} + \mu^* \end{bmatrix}, \tag{1.29}$$

where $\mu^* = \Delta_Z + \mu$ and $\Delta_{SC}^* = -\alpha_R\frac{\Delta_{SC}}{\Delta_Z}$. This is equal to the Hamiltonian of a p-wave superconductor (p. 80 in [19]). This model retains the same features as the original Hamiltonian, as we will see in the next chapter, namely a gapped energy spectrum for $\Delta_{SC}^*, \mu^* \neq 0$ and a topological phase transition at $\mu^* = 0$ from a topological phase ($\mu^* > 0$) containing MFs to a non-topological phase ($\mu^* < 0$) with no MFs.

Depending on the chosen parameters, the smallest gap can either be at $p = 0$ or $p = p_F$, but in both cases it is possible to make a effective low-energy approximation about the point where the gap is smallest which is equal to the Hamiltonian of a p-wave superconductor, assuming the gap is small[20]. We can see this happen in figure 1.2e in the case of $\Delta_Z \approx \Delta_{SC} \approx E_{SO}$ where the energy spectrum is linear close to $p = 0$. For $\Delta_Z \neq \Delta_{SC}$ as small gap will open at $p = 0$. We therefore conclude that the spinless p-wave Hamiltonian is a valid effective low-energy Hamiltonian for the original system when only the lower band is occupied and the energy gap is small.

From here on we will drop the asterisk on Δ_{SC}^* and μ^*.

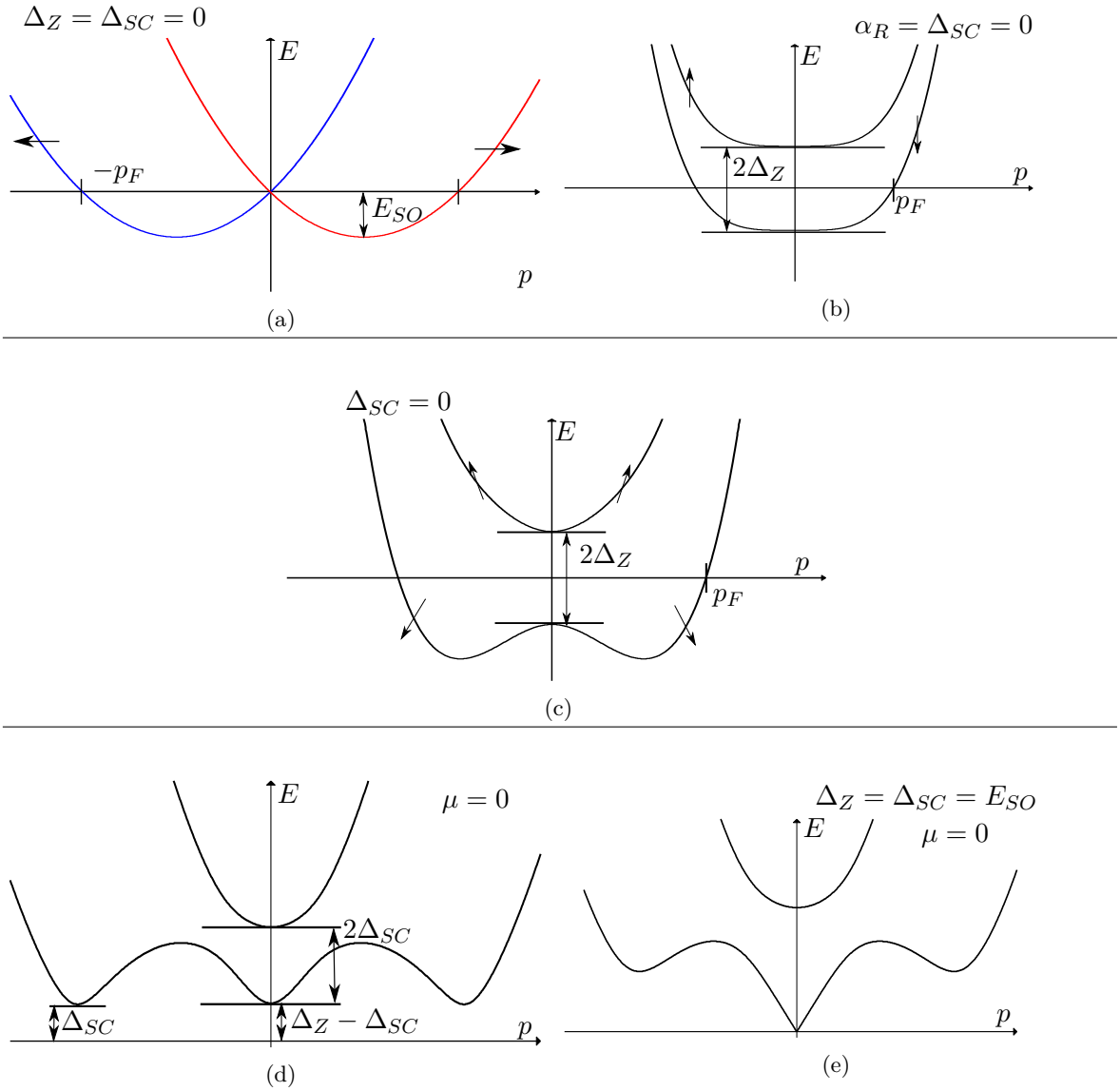

Figure 1.2: Dispersion relation in eq. (1.12) of the Hamiltonian ineq. (1.10) in five cases. The alignment of the spin has been marked for each band in (a), (b) and (c) with arrows. (a): $\Delta_Z = \Delta_{SC} = 0$. Spin-orbit interaction changes the energy of the electron depending on the orientation of the spin relative to its momentum. The red and blue curves are for electrons with opposite spin. (b): $\alpha_R = \Delta_{SC} = 0$. The Zeeman field induces an energy splitting between electrons with opposite spin. (c): $\Delta_{SC} = 0$. For $\Delta_Z \gg E_{SO}$, the spins will mostly be aligned parallel to the B-field. (d): If Δ_Z, Δ_{SC}, $\alpha_R \neq 0$ the energy spectrum will be gapped for $\Delta_Z^2 \neq \Delta_{SC}^2 + \mu^2$. (e) If $\Delta_Z = \Delta_{SC} = E_{SO}$ and $\mu = 0$ the dispersion is linear close to $p = 0$. There exist are wide range of parameters where the chemical potential can be placed between bands of electrons with almost opposite spin and the low energy limit can be described by a spin-polarized Hamiltonian.

Chapter 2

One dimensional spinless p-wave superconductor

In the introduction we showed that the effective low-energy Hamiltonian of the Hamiltonian describing a semiconductor-superconductor quantum wire system is equivalent to the Hamiltonian describing a one-dimensional spinless p-wave superconductor. In the rest of this thesis we will only be concerned with the Hamiltonian describing one-dimensional p-wave superconductor and we will refer to this Hamiltonian as the p-wave Hamiltonian for short. Since the physical realization of the system is a quantum wire in proximity contact with a superconductor we will also refer to the system as the quantum wire or just wire, but the p-wave Hamiltonian is always the governing equation. We therefore commence this chapter by taking a step back to perform a more general inspection of a superconductor with spinless fermions and see that the lack of spin results to first order in p-wave pairing. We will then proceed to investigate topological properties of the p-wave Hamiltonian and determine the existence of zero energy Majorana bound end states.

We start by considering the general Hamiltonian of a 1D spinless superconductor put along the x-direction, which has the form

$$\begin{aligned} H &= \int \Psi^\dagger(x')\delta(x-x')\left(\frac{-\hbar^2\partial_x^2}{2m}-\mu\right)\Psi(x)+\frac{1}{2}\Psi^\dagger(x')\Delta(x,x')\Psi^\dagger(x)+\text{h.c.}\ \mathrm{d}x\,\mathrm{d}x' \\ &= H_0+H_\Delta, \end{aligned} \tag{2.1}$$

where the first part is the kinetic term and chemical potential and the second part is the effective pairing potential. $\Psi^{(\dagger)}(x)$ annihilates (creates) a spinless fermion at position x, with mass m and μ is the chemical potential. We will not be concerned with the microscopic origin of the pairing potential, but merely state that Δ is the effective pairing potential of the superconductor. It does not need to be local and will in fact have to be non-local in the present model as the fermions are spinless and obey Fermi-Dirac-statistics. This can be shown by considering the obviously true equation

$$\int \Psi^\dagger(x')\Delta(x,x')\Psi^\dagger(x)\ \mathrm{d}x\,\mathrm{d}x' = \int \Psi^\dagger(x)\Delta(x',x)\Psi^\dagger(x')\ \mathrm{d}x\,\mathrm{d}x' \tag{2.2}$$

where the coordinates just have been relabeled. We rewrite the left-hand side

$$\begin{aligned}\int \Psi^\dagger(x')\Delta(x,x')\Psi^\dagger(x)\,\mathrm{d}x\,\mathrm{d}x' &= \int \Psi^\dagger(x')\Psi^\dagger(x)\Delta(x,x') + \Psi^\dagger(x')\left[\Delta(x,x'),\Psi^\dagger(x)\right]\,\mathrm{d}x\,\mathrm{d}x' \\ &= -\int \Psi^\dagger(x)\Psi^\dagger(x')\Delta(x,x') + \Psi^\dagger(x')\left[\Delta(x,x'),\Psi^\dagger(x)\right]\,\mathrm{d}x\,\mathrm{d}x' \\ &= -\int \Psi^\dagger(x)\Delta(x,x')\Psi^\dagger(x') + \Psi^\dagger(x')\left[\Delta(x,x'),\Psi^\dagger(x)\right] \\ &\qquad + \Psi^\dagger(x)\left[\Delta(x,x'),\Psi^\dagger(x')\right]\,\mathrm{d}x\,\mathrm{d}x'. \end{aligned} \tag{2.3}$$

The right-hand side of eq. (2.2) and eq. (2.3) have to be equal, which is true when Δ is antisymmetric in the coordinates, $\Delta(x,x') = -\Delta(x',x)$. This gives us that $\Delta(x,x) = -\Delta(x,x) \Rightarrow \Delta(x,x) = 0$ and Δ therefore has to be non-local. If the fermions had been spinfull, Δ could have been antisymmetric in the spin indices instead of the coordinates and Δ would not need to be non-local. Next we assume that Δ only depends on the distance between x and x' and that it is short ranged:

$$\Delta(x,x') = (x-x')f(x-x')\Delta_0, \tag{2.4}$$

where f is a very narrow symmetric distribution about zero and is normalized as $\int f(x'-x)(x'-x)^2\,\mathrm{d}x' = 1$ and Δ_0 is a complex constant. We insert this into H_Δ and Taylor expand $\Psi^\dagger(x)$ to first order around x' and $\Psi^\dagger(x')$ to first order around x:

$$H_\Delta = \frac{1}{2}\int \Psi^\dagger(x')(x-x')f(x-x')\Delta_0\Psi^\dagger(x) + \text{h.c.}\;\mathrm{d}x\,\mathrm{d}x' \tag{2.5}$$

$$\begin{aligned} &\approx \frac{1}{4}\int \left(\Psi^\dagger(x) + \partial_x\Psi^\dagger(x)(x'-x)\right)(x-x')f(x-x')\Delta_0\Psi^\dagger(x) \\ &\qquad + \Psi^\dagger(x')(x-x')f(x-x')\Delta_0\left(\Psi^\dagger(x') + \partial_{x'}\Psi^\dagger(x')(x-x')\right) + \text{h.c.}\;\mathrm{d}x\,\mathrm{d}x' \\ &= \frac{1}{4}\int \Psi^\dagger(x)(x'-x)^2 f(x'-x)\Delta_0\partial_x\Psi^\dagger(x) \\ &\qquad - \left(\partial_x\Psi^\dagger(x')\right)(x-x')^2 f(x-x')\Delta_0\Psi^\dagger(x') + \text{h.c.}\;\mathrm{d}x\,\mathrm{d}x'. \end{aligned} \tag{2.6}$$

Terms containing $\Psi^\dagger(x)\Psi^\dagger(x)$ or $\Psi(x)\Psi(x)$ are equal to zero when the integration is performed due to Fermi-Dirac-statistics. One of the remaining two integration is done using the normalization of f and we relabel the variable in the second term such that the variables are the same. The result is:

$$H_\Delta = \frac{1}{4}\int \Psi^\dagger(x)\Delta_0\partial_x\Psi^\dagger(x) - \left(\partial_x\Psi^\dagger(x)\right)\Delta_0\Psi^\dagger(x) + \text{h.c.}\;\mathrm{d}x. \tag{2.7}$$

This symmetric expansion of Ψ about both x and x' might seem redundant, but it will become important later when we write H in a basis of eigenmodes of a one-dimensional box. We insert eq. (2.7) into eq. (2.1) to get the full Hamiltonian in real space:

$$\begin{aligned} H &= \int \Psi^\dagger(x)\left(\frac{-\hbar^2\partial_x^2}{2m} - \mu\right)\Psi(x) + \frac{1}{4}\left[\Psi^\dagger(x)\Delta(-i\hbar\partial_x)\Psi^\dagger(x) - \left(-i\hbar\partial_x\Psi^\dagger(x)\right)\Delta\Psi^\dagger(x) + \text{h.c.}\right]\,\mathrm{d}x \\ &= H_0 + H_\Delta, \end{aligned} \tag{2.8}$$

where we have redefined $\Delta_0 \to -i\hbar\Delta$. Henceforth we will often set $\hbar = 1$ to simplify the expressions, but it can be restored by considering the units.

For a translational invariant system, we can Fourier transform to the momentum basis by $\Psi^\dagger(x) = \sum_p \mathrm{e}^{-ipx}c_p^\dagger$, where $c_p^\dagger$ creates a fermion at momentum p. The Hamiltonian then becomes

$$H = \sum_p \left(\frac{p^2}{2m} - \mu\right)c_p^\dagger c_p + \frac{1}{2}\left(p\Delta c_p^\dagger c_{-p}^\dagger + \text{h.c.}\right), \tag{2.9}$$

which is recognized to be the Hamiltonian for a p-wave superconductor (as seen on p. 80 in [19]).

Topological phases are characterized by a topological invariant which is a property of the system that is invariant under adiabatic changes of parameters. Different topological invariants can be defined depending on the system at hand. Examples of topological invariants are: Chern numbers, the existence of some definite number of in-gap states or the winding number of a vector with respect to changing a parameter. A topological phase transition takes place when the topological invariant changes. This is usually accompanied by a closing of a gap in the energy spectrum if the phase transition involves a creation/annihilation of some in-gap states[4]. Possible topological phase transitions can therefore often be located by searching for gap closings in the energy spectrum.
In the next section we will examine the energy spectrum of the p-wave Hamiltonian of locate any gap closings.

2.1 Dispersion relation

We calculate the dispersion relation of the p-wave Hamiltonian i eq. (2.9) to investigate the how it depends on the model parameters and locate gap closing points.

For notational simplicity we sometimes denote $\frac{p^2}{2m} - \mu \equiv \xi(p)$. First we rewrite the Hamiltonian in the Bogoliubov-de-Gennes formalism. Using the anti-commutations relations for the fermion operators

$$\{c_p^\dagger, c_{p'}\} = \delta_{pp'}, \qquad \{c_p, c_{p'}\} = \{c_p^\dagger, c_{p'}^\dagger\} = 0 \tag{2.10}$$

we write eq. (2.9) as

$$H = \sum_p \xi(p)\frac{1}{2}(c_p^\dagger c_p - c_p c_p^\dagger + 1) + \sum_p \frac{1}{2}(p\Delta c_p^\dagger c_{-p}^\dagger + p\Delta^* c_{-p} c_p) \tag{2.11}$$

$$= \frac{1}{2}\sum_p \xi(p)(c_p^\dagger c_p - c_{-p} c_{-p}^\dagger) + \sum_p (p\Delta c_p^\dagger c_{-p}^\dagger + p\Delta^* c_{-p} c_p) + \frac{1}{2}\sum_p \xi(p), \tag{2.12}$$

where the momentum p has been relabelled in the second term in the first sum. The last term is simply a constant which shift all energy levels of H and we will omit it since we are not concerned about the total energy of the system. We introduce the spinor $\mathbf{c}_p \equiv (c_p, c_{-p}^\dagger)^T$ and write H in the simple form

$$H = \frac{1}{2}\sum_p \mathbf{c}_p^\dagger \mathscr{H} \mathbf{c}_p, \tag{2.13}$$

$$\mathscr{H} = \begin{bmatrix} \xi(p) & p\Delta \\ p\Delta^* & -\xi(p) \end{bmatrix} \tag{2.14}$$

$$= \xi(p)\tau_z + p\Delta\tau_x, \tag{2.15}$$

where τ_i are Pauli matrices and we have assumed that the pairing potential is real, $\Delta = \Delta^*$. $\mathscr{H}$ is called the single particle Hamiltonian.

The eigenvalues of $\mathscr{H}$ are:

$$E_{\pm}(p) = \pm\sqrt{\xi(p)^2 + (p\Delta)^2}. \tag{2.16}$$

and are plotted in figure (2.1). The energy spectrum is gapped for $\Delta \neq 0$ and $\mu \neq 0$, but the gap closes when μ passes through zero, indicating a possible topological phase transition.

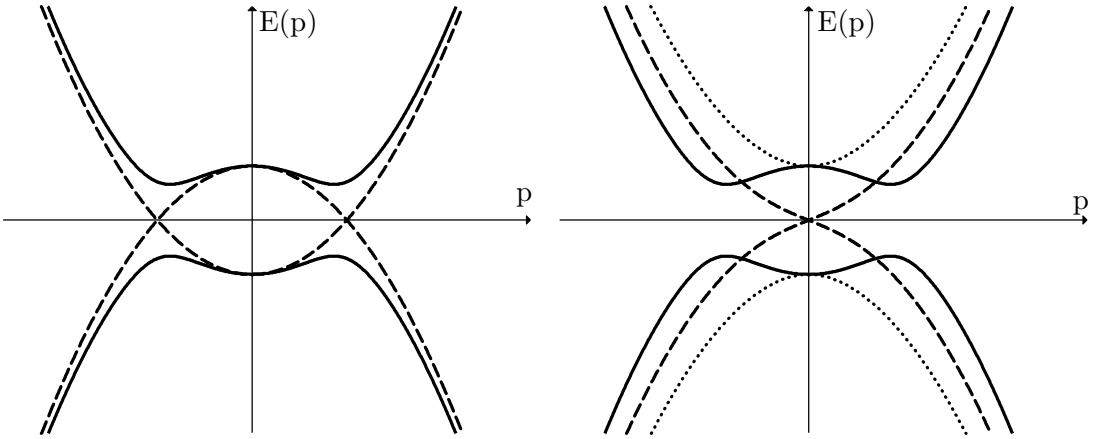

(a) $\mu > 0$ and $m = 1$. Dashed line is for $\Delta = 0$, while the solid line is for $\Delta \neq 0$.

(b) $\Delta \neq 0$. Solid line $\mu > 0$, Dashed and $\mu = 0$ and dotted $\mu < 0$.

Figure 2.1: Dispersion relation of p-wave Hamiltonian in different cases.

2.2 Topoligical invariant

As mentioned above, a topological phase is characterized by a topological invariant which is invariant under adiabatic change of parameters and only changes when a topological phase transition occurs. In the present case it is convenient to define a winding number which characterizes how many times a given vector rotates around zero.

Consider the vector

$$\vec{v} = C\left[\left(\frac{p^2}{2m} - \mu\right)\hat{z} + p\Delta\hat{x}\right], \tag{2.17}$$

where $C = \sqrt{\left(\frac{p^2}{2m} - \mu\right)^2 + (p\Delta)^2}^{-1}$ is a normalization factor and $\hat{z}$ and $\hat{x}$ are eigenvectors of τ_z and τ_x, and $\hat{z} \cdot \hat{x} = 0$. Now let $\hat{z}$ and $\hat{x}$ be unitvectors in a euclidean coordinate system and define θ as the angle which $\vec{v}$ makes with the x-axis:

$$\tan\theta = \frac{p\Delta}{\frac{p^2}{2m} - \mu}. \tag{2.18}$$

We assume $\Delta, m > 0$. In figure (2.2) we have plotted the dependence of θ on p as p goes from $-\infty$ to $+\infty$ for $\mu < 0$ and $\mu > 0$ and selected values of $\theta(p)$ are listed in table 2.1.
If $\mu > 0$, the vector $\vec{v}$ rotates one time around the origin giving us a winding number of 1 while in the case $\mu < 0$, $\vec{v}$ does not cross the z-axis and the winding number is 0. The winding number constant throughout each domain $\mu > 0$ and $\mu < 0$ separately and changes value only at $\mu = 0$ which tells us that a topological phase transition occur at $\mu = 0$.

Now that we have a way to label different topological phases, we need to determine which of the phases is topologically trivial and which is non-trivial.

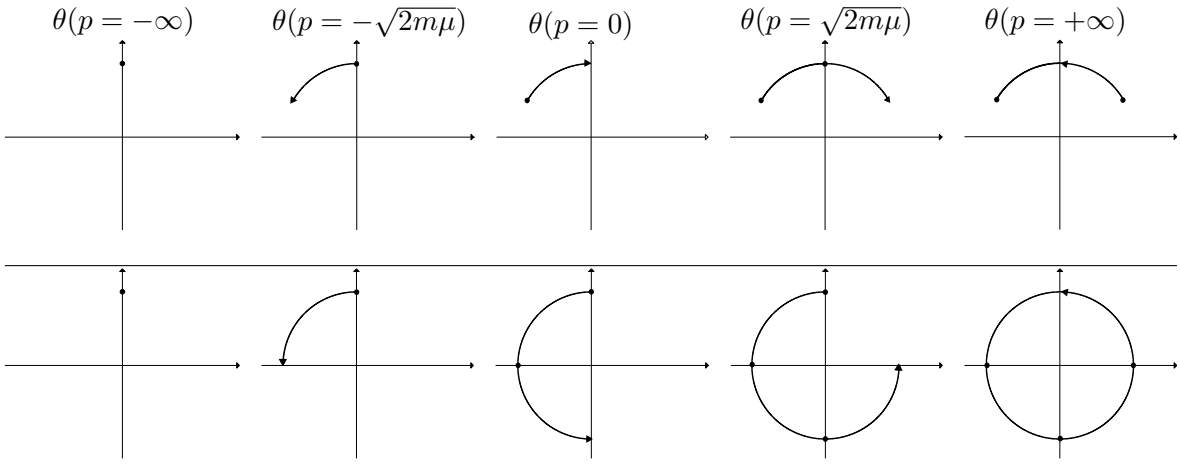

Figure 2.2: The x-axis points upwards and the z-axis points to the right. $\theta(p)$ for p going from $-\infty$ to $+\infty$ for $\mu < 0$ in the upper panel and $\mu > 0$ in the lower.

p	$\theta(p)$ for $\mu > 0$	$\theta(p)$ for $\mu < 0$
$-\infty$	0	0
$-\sqrt{2m\mu}$	$-\frac{\pi}{2}$	$\arctan\left(-\sqrt{\frac{m}{2\lvert\mu\rvert}}\right)$
0	$-\pi$	0
$\sqrt{2m\mu}$	$-\frac{3\pi}{2}$	$\arctan\left(\sqrt{\frac{m}{2\lvert\mu\rvert}}\right)$
∞	-2π	0

Table 2.1: Selected values of $\theta(p)$ in the case $\mu > 0$ and $\mu < 0$.

2.3 Zero energy edge modes

We will now show that the p-wave Hamiltonian can host zero energy bound states at the boundary of the topological non-trivial phase. We consider the single particle Hamiltonian from eq. (2.14) in real space representation ($p \to -i\hbar\partial_x$),

$$\mathscr{H} = \left(\frac{-\hbar^2\partial_x}{2m} - \mu\right)\tau_z - i\hbar\partial_x\Delta\tau_x \tag{2.19}$$

in the case of a semi-infinite wire with hard wall boundary condition. That is, the superconductor starts at $x = 0$ and extends to $+\infty$ and wavefunctions must be zero at $x = 0$. We follow the procedure in section 2.5.1 of [19] and look for zero energy solutions to the time-independent Schrödinger equation

$$\mathscr{H}\vec{\varphi}(x) = \left[\left(\frac{-\hbar^2\partial_x^2}{2m} - \mu\right)\tau_z - i\hbar\partial_x|\Delta|\tau_x\right]\vec{\varphi}(x) = 0. \tag{2.20}$$

Multiplying from the left by τ_z and rearranging yields

$$\left[\left(\frac{\hbar^2}{2m}\partial_x^2+\mu\right)\tau_0-\hbar\Delta\partial_x\tau_y\right]\vec{\varphi}(x)=0. \tag{2.21}$$

It is now clear that we can write $\vec{\varphi}(x)=\vec{\chi}_\nu\phi(x)$, where $\vec{\chi}$ is an eigenvector of τ_y, i.e. $\tau_y\vec{\chi}_\nu=\nu\vec{\chi}_\nu$, $\nu=\pm1$ and eq. (2.21) then becomes an ordinary differential equation

$$\left(\frac{\hbar^2}{2m}\partial_x^2+\mu-\nu\hbar\Delta\partial_x\right)\varphi(x)=0, \tag{2.22}$$

which we can solve with an appropriate trial function. We take the trial function $\phi\propto \mathrm{e}^{-\lambda x}$ and get the secular equation

$$0=\frac{\hbar^2}{2m}\lambda^2+\nu\hbar\Delta\lambda+\mu \tag{2.23}$$

$$\Downarrow$$

$$\lambda_\pm=\frac{m\Delta}{\hbar}\left(-\nu\pm\sqrt{\nu^2-2\frac{\mu}{m\Delta^2}}\right) \tag{2.24}$$

Since we are looking for edge modes, we require that $\phi(0)=\phi(+\infty)=0$ which gives us the condition $\mathrm{Re}(\lambda_\pm)>0$. If ϕ is localised at the left end of the wire ($x=0$), this can only be satisfied for $\nu=-1$ and

$$\left|1-2\frac{\mu}{m\Delta^2}\right|<1 \qquad \Rightarrow \qquad 0<\mu<m\Delta^2, \tag{2.25}$$

assuming $m>0$ and $\mathrm{Im}\Delta=0$. The eigenvector of τ_y with eigenvalue -1 is $\frac{1}{\sqrt{2}}\begin{pmatrix}-1\\ i\end{pmatrix}$. Hence there exists a bound state solution with zero energy of the form

$$\vec{\varphi}(x)=\frac{C}{\sqrt{2}}\begin{pmatrix}-1\\ i\end{pmatrix}\left(\mathrm{e}^{-\lambda_+x}-\mathrm{e}^{-\lambda_-x}\right), \tag{2.26}$$

with $\lambda_\pm=\frac{m\Delta}{\hbar}\left(1\pm\sqrt{1-2\frac{\mu}{m\Delta^2}}\right)$ and C being a normalization constant. $|\phi(x)|^2$ is plotted in figure (2.3).

We also see that the constraint on μ can be relaxed to $\mu>0$ as $\lambda_\pm$ can take on complex values as long as its real part is strictly positive, since this still yields a bound solution. These zero energy solutions exist in the entire domain of $\Delta\neq0$ and $\mu>0$, but only for a semi-infinite wire. If the wire is finite, there will be a bound state at each end of the wire which decays exponentially from the edge. In the case of a short wire, there will be a non-negligible overlap between the two edge states and the states will hybridize. The energy of the Majorana edge states $\pm E_0$ will be exponentially small in the length of the wire[11]. This will be elaborated in section 3.2.

In figure 2.4 we have plotted the energy spectrum of the Hamiltonian (2.15 as a function of chemical potential μ with fixed wire length L, pairing potential Δ and mass m. The model from which the numerical data is obtained will be elaborated in section 3.3. We see that there exist zero energy modes in the domain $\mu>0$ while they are absent for $\mu<0$ in agreement of the findings in this section. The numerically obtained bulk spectrum matches in both cases the bulk spectrum obtained from the analytical expression in eq. (2.16).

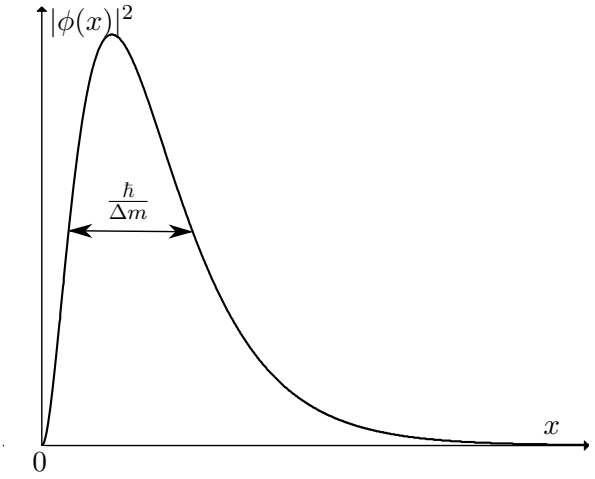

Figure 2.3: The qualitative feature of the norm squared of the wave function of the zero energy state $|\phi(x)|^2$ at the boundary of the wire at $x = 0$.

In this chapter we have shown that the 1D p-wave Hamiltonian model can exhibit two distinct topological phases: A non-trivial phase in which there exists zero energy bound states at the ends of the wire and a trivial state where they are absent.
The next step will be to develop numerical methods in order to investigate the dynamics of these bound edge states.

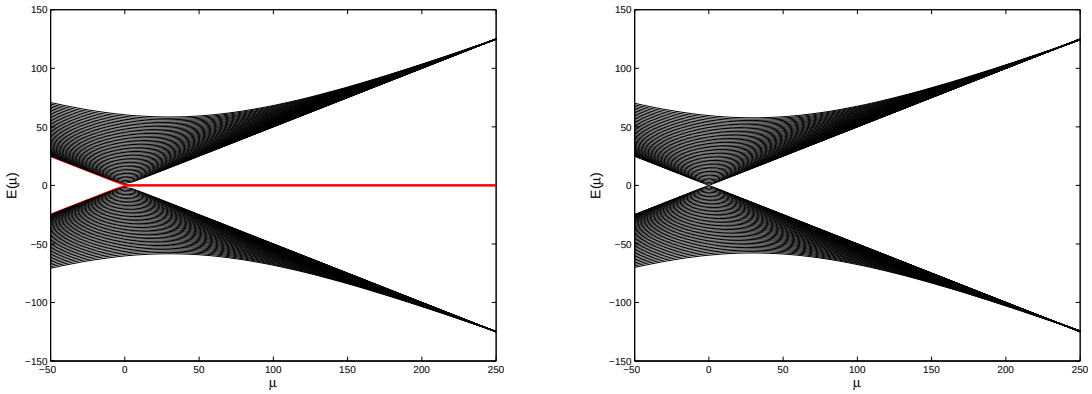

Figure 2.4: Energy spectrum as a function of chemical potential μ for a wire of length $L = 20$ and pairing potential $\Delta = 15$. We set mass m and $\hbar$ equal to one. The left plot is obtained by numerical diagonalisation of eq. (3.56) with $N = 500$ eigenmodes and the Majorana bound state is highlighted red. The right plot is obtained by the dispersion relation in eq. (2.16). Only the 50 lowest energy states are displayed.

Chapter 3

Numerical studies of the p-wave Hamiltonian

In this chapter we will introduce two numerical methods for examining the p-wave superconductor which enables us to obtain the energy eigenvalues and eigenvectors of the Hamiltonian by numerical diagonalization. Disorder will be included in the next chapter while we will in consider the clean wire case in this chapter and compare numerical result with theoretical predictions from the literature.

Initially we began our work with a tight-binding model. This model has a different phase diagram than the original Hamiltonian model and is equivalent to the model introduced by Kitaev [11]. We will go through the basics of this model in order get a more detailed understanding of the Majorana bound states.
Later we thought of providing further support for the numerical results by using a different model and decided to use the eigenmode model. It is though not new model but merely a representation of the p-wave Hamiltonian in the basis of eigenmodes of a 1D box of length L. However, we will be referred to this as the eigenmode model. This model retain the phase diagram of the original Hamiltonian.

In the end of the chapter we will compare the two numerical methods and discuss their relative advantages and drawbacks.

3.1 The tight-binding model

We model the p-wave superconductor as a one dimensional chain of N sites. A tight-binding model is created by mapping the continuous p-wave Hamiltonian into a discrete lattice model. This is done by substituting

$$p \to \frac{1}{a}\sin(pa), \qquad p^2 \to \frac{4}{a^2}\sin^2\left(\frac{pa}{2}\right) = \frac{2}{a^2}(1-\cos(pa)), \tag{3.1}$$

where $a = \frac{L}{N}$ is the lattice spacing, L is the length of the chain and N is the number of sites. This substitution is an equality in the long wavelength limit $pa \to 0$. The tight-binding model captures the relevant low-energy physics of the original model and is valid in limit $pa \ll 1$ which is the case when N is large. In this limit we can take the momenta to be continuous and change the sum to an integral $\sum_p \to \int \mathrm{d}p$. We write the p-wave Hamiltonian from eq. (2.13)

and (2.15) here to avoid scrolling backwards

$$H = \frac{1}{2}\sum_p \mathbf{c}_p^\dagger \mathscr{H} \mathbf{c}_p, \tag{3.2}$$

$$\mathscr{H} = \left(\frac{p^2}{2m} - \mu\right)\tau_z + p\Delta\tau_x, \tag{3.3}$$

and we insert the approximation from eq. (3.1) along with a Fourier transformation to real space:

$$\mathbf{c}_p = \begin{pmatrix} c_p \\ c_{-p}^\dagger \end{pmatrix} = \sum_i \begin{pmatrix} \mathrm{e}^{ipR_i}\tilde{c}_i \\ \mathrm{e}^{-i(-p)R_i}\tilde{c}_i^\dagger \end{pmatrix} = \sum_i \mathrm{e}^{ipR_i}\begin{pmatrix} \tilde{c}_i \\ \tilde{c}_i^\dagger \end{pmatrix} = \sum_i \mathrm{e}^{ipR_i}\tilde{\mathbf{c}}_i \tag{3.4}$$

$$H = \frac{1}{2}\sum_{ij}\int \mathrm{e}^{-ipR_i}\tilde{\mathbf{c}}_i^\dagger \left[\left(\frac{\hbar^2}{ma^2}(1-\cos(pa)) - \mu\right)\tau_z + \frac{\Delta}{a}\sin(pa)\tau_x\right]\mathrm{e}^{ipR_j}\tilde{\mathbf{c}}_j \,\mathrm{d}p, \tag{3.5}$$

where $R_j = aj\,,\ j = 1, ..., N$ is a lattice vector. We now rewrite sine and cosine in terms of exponential functions and perform the integral over p:

$$\begin{aligned} H &= \frac{1}{2}\sum_{ij}\int \mathrm{e}^{-ipR_i}\tilde{\mathbf{c}}_i^\dagger \left[\left(\frac{\hbar^2}{ma^2}\left(1 - \frac{1}{2}\left(\mathrm{e}^{ipa} + \mathrm{e}^{-ipa}\right)\right) - \mu\right)\tau_z \right. \\ &\qquad \left. -\frac{i\Delta}{2a}\left(\mathrm{e}^{ipa} - \mathrm{e}^{-ipa}\right)\tau_x\right]\mathrm{e}^{ipR_j}\tilde{\mathbf{c}}_j \,\mathrm{d}p \qquad (3.6) \\ &= \frac{1}{2}\sum_{ij}\tilde{\mathbf{c}}_i^\dagger \left[\left(\frac{\hbar^2}{ma^2}\left(\delta_{i,j} - \frac{1}{2}(\delta_{i,j+1} + \delta_{i+1,j})\right) - \mu\delta_{i,j}\right)\tau_z \right. \\ &\qquad \left. -\frac{i\Delta}{2a}(\delta_{i,j+1} - \delta_{i+1,j})\tau_x\right]\tilde{\mathbf{c}}_j \qquad (3.7) \\ &= \frac{1}{2}\sum_i \tilde{\mathbf{c}}_i^\dagger\left(\frac{\hbar^2}{ma^2} - \mu\right)\tau_z\tilde{\mathbf{c}}_i + \tilde{\mathbf{c}}_{i+1}^\dagger\left(-\frac{\hbar^2}{2ma^2}\tau_z - \frac{i\Delta}{2a}\tau_x\right)\tilde{\mathbf{c}}_i \\ &\qquad + \tilde{\mathbf{c}}_i^\dagger\left(-\frac{\hbar^2}{2ma^2}\tau_z + \frac{i\Delta}{2a}\tau_x\right)\tilde{\mathbf{c}}_{i+1} \qquad (3.8) \\ &= \frac{1}{2}\sum_{i=1}^{N}\tilde{\mathbf{c}}_i^\dagger D\tilde{\mathbf{c}}_i + \frac{1}{2}\sum_{i=1}^{N-1}\tilde{\mathbf{c}}_{i+1}^\dagger T\tilde{\mathbf{c}}_i + \tilde{\mathbf{c}}_i^\dagger T^\dagger\tilde{\mathbf{c}}_{i+1}, \qquad (3.9) \end{aligned}$$

where

$$D = \left(\frac{\hbar^2}{ma^2} - \mu\right)\tau_z\,, \qquad T = \left(-\frac{\hbar^2}{2ma^2}\tau_z - \frac{i\Delta}{2a}\tau_x\right), \tag{3.10}$$

for a more compact notation. We write the Hamiltonian as a $2N \times 2N$ matrix by defining the Nambu spinor $\vec{\tilde{c}} = (\tilde{\mathbf{c}}_1, \tilde{\mathbf{c}}_2, ..., \tilde{\mathbf{c}}_N)^T$ which is of length $2N$ since each $\tilde{\mathbf{c}}_i$ is a 2-spinor

$\tilde{\mathbf{c}}_i = (\tilde{c}_i, \tilde{c}_i^\dagger)^T$. Using these Nambu spinos, the Hamiltonian can be written as

$$H = \frac{1}{2}\vec{\tilde{c}}^\dagger \mathcal{H} \vec{\tilde{c}}, \tag{3.11}$$

$$\mathcal{H} = \begin{pmatrix} D & T & 0 & 0 & \cdots & 0 \\ T^\dagger & D & T & 0 & \cdots & 0 \\ 0 & T^\dagger & D & T & \cdots & 0 \\ \vdots & \vdots & \ddots & \ddots & \ddots & \vdots \\ 0 & 0 & 0 & T^\dagger & D & T \\ 0 & 0 & 0 & 0 & T^\dagger & D \end{pmatrix}. \tag{3.12}$$

The eigenvectors and eigenvalues can then be obtained by numerical diagonalization of this tight-binding Hamiltonian. Next we will examine the tight-binding model in more detail and see that it is equivalent to the Kitaev toy model[11]. This enables us to compare the numerical results with predictions for the Kitaev chain and other related models before we move into less charted territory.

We note that the tight-binding has a different dispersion relation than the p-wave Hamiltonian. By inserting by inserting eq. (3.1) in eq. (2.16) we get the dispersion relation for the tight-binding model:

$$E(p)_\pm^{\text{TBA}} = \pm\sqrt{\left(\frac{1}{ma^2}\left(1-\cos(pa)\right)-\mu\right)^2 + \left(\frac{\Delta}{a}\sin(pa)\right)^2}, \tag{3.13}$$

As a consequence there has been introduced a second point where the gap closes and another phase transition occurs at $\mu = \frac{2}{ma^2}$. We will address this in the next section.

3.2 Kitaev Toy Model

We will in this section show that the tight-binding model is equivalent to the Kitaev toy model[11] and then review this model. We relabel the parameters in eq. (3.8) by

$$\frac{1}{ma^2} - \mu \to -\tilde{\mu} \quad , \qquad \frac{1}{2ma^2} \to \tilde{t} \quad , \qquad \frac{i\Delta}{2a} \to \tilde{\Delta} \tag{3.14}$$

and expand the matrix products $\tilde{\mathbf{c}}_i^\dagger \tau_j \tilde{\mathbf{c}}_k$:

$$\begin{aligned} H = \frac{1}{2}\sum_i \Big[&-\tilde{\mu}(c_i^\dagger c_i - c_i c_i^\dagger) - \tilde{t}(c_{i+1}^\dagger c_i - c_{i+1}c_i^\dagger + c_i^\dagger c_{i+1} - c_i c_{i+1}^\dagger) \\ &+\tilde{\Delta}(c_{i+1}^\dagger c_i^\dagger + c_{i+1}c_i - c_i^\dagger c_{i+1}^\dagger - c_i c_{i+1})\Big] \end{aligned} \tag{3.15}$$

We use the anti-commutation relations of the fermion operators to write the operators in normal order and get

$$H = \sum_i \left[-\tilde{\mu}\left(c_i^\dagger c_i - \frac{1}{2}\right) - \tilde{t}(c_i^\dagger c_{i+1} + c_{i+1}^\dagger c_i) + \tilde{\Delta}(c_{i+1}^\dagger c_i^\dagger + c_i c_{i+1})\right] \tag{3.16}$$

which is equivalent to the model in eq. (4) in [11].

We will recap on the results of [11], as they will provide some additional insight to the nature of the Majorana fermions. To do this, we define a new set of operators called Majorana operators

$$a_{2j-1} = c_j^\dagger + c_j \ , \qquad a_{2j} = i(c_j^\dagger - c_j) \qquad (j = 1, ..., N), \tag{3.17}$$

which are hermitian

$$a_m^\dagger = a_m \qquad (m = 1, ..., 2N). \tag{3.18}$$

We derive their anti-commutations relations from the anti-commutations relations of the original fermion operators, $\{c_k^\dagger, c_l\} = \delta_{kl}$ and $\{c_k^\dagger, c_l^\dagger\} = \{c_k, c_l\} = 0$, $(k, l = 1, ..., N)$:

$$\begin{aligned}\{a_{2k-1}, a_{2l-1}\} &= \{(c_k^\dagger + c_k), (c_l^\dagger + c_l)\} = \{c_k^\dagger, c_l^\dagger\} + \{c_k, c_l\} + \{c_k, c_l^\dagger\} + \{c_k, c_l^\dagger\} \\ &= 2\delta_{kl}\end{aligned} \tag{3.19}$$

$$\begin{aligned}\{a_{2k}, a_{2l}\} &= \{i(c_k^\dagger - c_k), i(c_l^\dagger - c_l)\} = -\{c_k^\dagger, c_l^\dagger\} - \{c_k, c_l\} + \{c_k, c_l^\dagger\} + \{c_k, c_l^\dagger\} \\ &= 2\delta_{kl}\end{aligned} \tag{3.20}$$

$$\begin{aligned}\{a_{2k}, a_{2l-1}\} &= \{i(c_k^\dagger - c_k), c_l^\dagger + c_l\} = i\{c_k^\dagger, c_l^\dagger\} - i\{c_k, c_l\} - i\{c_k, c_l^\dagger\} + i\{c_k, c_l^\dagger\} \\ &= 0,\end{aligned} \tag{3.21}$$

which combines to

$$\{a_m, a_n\} = 2\delta_{mn} \qquad \text{for} \qquad (m, n = 1, ..., 2N) \tag{3.22}$$

These new operators correspond to splitting the original fermion operators into real and imaginary parts. As a consequence, the operators a_j only contain half a degree of freedom and does not abide the usual Pauli exclusion principle of ordinary fermions, but instead

$$a_i^2 = (a_i^\dagger)^2 = a_i^\dagger a_i = a_i a_i^\dagger = 1. \tag{3.23}$$

It is therefore meaningless to speak of the occupancy of a Majorana mode in terms of a number operator of the usual form. If we define a Majorana number operator, $n_i^{\mathrm{MF}} = a_i^\dagger a_i$, it would always return $n_i^{\mathrm{MF}} = 1$. The same applies to the operator $a_i a_i^\dagger = 1$ and the Majorana mode always appears to be both full and empty. In terms of Majorana operators, the Hamiltonian takes the form

$$\begin{aligned}H = \sum_j \Big\{ &- \tilde{\mu} \left[\tfrac{1}{4} \left(a_{2j-1} - i a_{2j}\right) \left(a_{2j-1} + i a_{2j}\right) - \tfrac{1}{2}\right] \\ &- \tilde{t} \left[\tfrac{1}{4} \left(a_{2j-1} - i a_{2j}\right) \left(a_{2j+1} + i a_{2j+2}\right) + \tfrac{1}{4} \left(a_{2j+1} - i a_{2j+2}\right) \left(a_{2j-1} + i a_{2j}\right)\right] \\ &+ |\tilde{\Delta}| \left[\tfrac{1}{4} \left(a_{2j+1} - i a_{2j+2}\right) \left(a_{2j-1} - i a_{2j}\right) + \tfrac{1}{4} \left(a_{2j-1} + i a_{2j}\right) \left(a_{2j+1} + i a_{2j+2}\right)\right] \Big\} \\ = \frac{i}{2} \sum_j \Big\{ &-\tilde{\mu} a_{2j-1} a_{2j} + (\tilde{\Delta} + \tilde{t}) a_{2j} a_{2j+1} + (\tilde{\Delta} - \tilde{t}) a_{2j-1} a_{2j+2} \Big\},\end{aligned} \tag{3.24}$$

where we have used eq. (3.22).

3.2.1 Special cases

We now consider two special cases:

a) For $\tilde{\Delta} = \tilde{t} = 0$, $\tilde{\mu} < 0$ the Hamiltonian in eq. (3.24) become

$$H = -\frac{i\tilde{\mu}}{2}\sum_{j=1}^{N} a_{2j-1}a_{2j} = -\tilde{\mu}\sum_{j=1}^{N}(c_j^\dagger c_j - \frac{1}{2}), \tag{3.25}$$

where Majorana operators from the same site are paired together and form a trivial ground state.

b) For $\tilde{\Delta} = \tilde{t} > 0$, $\tilde{\mu} = 0$ we have the Hamiltonian

$$H = i\tilde{t}\sum_{j=1}^{N-1} a_{2j}a_{2j+1}, \tag{3.26}$$

which contains only terms with pairs of Majorana operators from different sites. We define a new set of fermion operators made of two Majorana operators from different sites

$$d_j = \tfrac{1}{2}(a_{2j} + ia_{2j+1}) \qquad , \qquad d_j^\dagger = \tfrac{1}{2}(a_{2j} - ia_{2j+1}). \tag{3.27}$$

In terms of these fermion operators the Hamiltonian takes the form

$$H = 2\tilde{t}\sum_{j=1}^{N-1}\left(d_j^\dagger d_j - \tfrac{1}{2}\right). \tag{3.28}$$

The difference between case a) and b) is illustrated in figure 3.1.

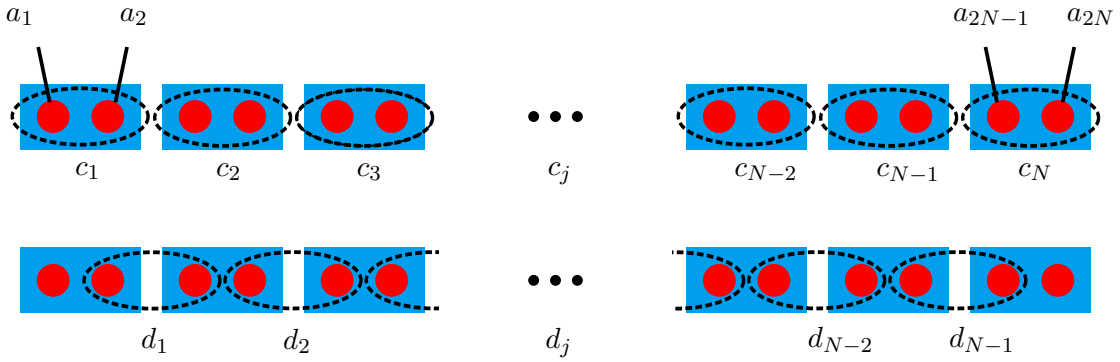

Figure 3.1: Illustration of the Kitaev chain. In the special case a), the Majorana operators a_j from same fermion sites c_j are paired together. In the special case b), the Majorana operators from neighbouring fermion sites are paired together and form the composite fermion operators d_j while leaving the two unpaired Majorana operators a_1 and a_{2N} at opposite ends of the chain.

The energy of the ground state is $\epsilon_0 = \tilde{t}(1-N)$ and hence for a state $|\psi_0\rangle$ to be a ground state it must satisfy

$$\mathrm{d}_j|\psi_0\rangle = 0 \qquad \text{for} \qquad j = 1, .., N-1. \tag{3.29}$$

There are two Majorana operators, a_1 and a_{2N} which no longer appear in the Hamiltonian in eq. (3.26). This makes it possible to find two orthogonal states $|\psi_0\rangle$ and $|\psi_1\rangle$ which satisfy the condition in eq. (3.29). We define the fermion operators

$$d_0 = \tfrac{1}{2}(a_1 + ia_{2N}) \qquad , \qquad d_0^\dagger = \tfrac{1}{2}(a_1 - ia_{2N}). \tag{3.30}$$

The two ground states $|\psi_0\rangle$ and $|\psi_1\rangle$ are related by this fermion operator:

$$|\psi_0\rangle = \tfrac{1}{2}(a_1 + ia_{2N})|\psi_1\rangle = d_0|\psi_1\rangle \tag{3.31}$$

$$|\psi_1\rangle = \tfrac{1}{2}(a_1 - ia_{2N})|\psi_0\rangle = d_0^\dagger|\psi_0\rangle. \tag{3.32}$$

This relation between the two ground states reveals that the fermionic state created by $d_0^\dagger$ is non-local as it involves Majorana operator from each end of the wire. Orthogonality of the states is seen by using eq. (3.22):

$$\begin{aligned}\langle\psi_0|\psi_1\rangle &= \tfrac{1}{4}\langle\psi_1|(a_1 - ia_{2N})(a_1 - ia_{2N})|\psi_0\rangle = \tfrac{1}{4}\langle\psi_1|a_1^2 - a_{2N}^2 - ia_1a_{2N} - ia_{2N}a_1|\psi_0\rangle \\ &= -i\tfrac{1}{4}\langle\psi_1|a_1a_{2N} - a_1a_{2N}|\psi_0\rangle = 0.\end{aligned} \tag{3.33}$$

As mentioned earlier, it is not possible to define an occupancy number of a Majorana mode using the usual number operator with Majorana operators. The fermioninc states however contains a definite number of fermions and they are eigenstates of the parity operator

$$\hat{P} = \prod_{j=1}^{N} -ia_{2j-1}a_{2j} = \prod_{j=0}^{N-1}(1 - 2d_j^\dagger d_j). \tag{3.34}$$

with eigenvalue ± 1 depending on whether the given state contains an even or and odd number of fermions. We note that

$$\left\{\hat{P}, d_j^\dagger\right\} = \hat{P}d_j^\dagger + d_j^\dagger\hat{P} = 0 \tag{3.35}$$

and use it to find

$$\hat{P}|\psi_0\rangle = d_0|\psi_1\rangle = -d_0\hat{P}|\psi_1\rangle = (-d_0)(\pm|\psi_1\rangle) = \mp|\psi_0\rangle, \tag{3.36}$$

from which we can conclude, that $|\psi_0\rangle$ and $|\psi_1\rangle$ have opposite parity. This means that the state $|\psi_{0/1}\rangle$ can only be a superposition of states with either an even or and odd number of fermions.

These two special cases represent different topological phases as one case exhibits zero energy edge modes consisting of two Majorana fermions, one at each end of the wire, while the other has no such state of unpaired Majorana fermions. The bulk properties of both phases are the same as we see from the dispersion relation which we write here in the notation of the Kitaev toy model

$$E(k)_\pm^{\mathrm{TBA}} = \pm\sqrt{\left(2\tilde{t}\cos(k) + \tilde{\mu}\right)^2 + \left(2\tilde{\Delta}\sin(k)\right)^2}, \qquad k \in [-\pi, \pi] \tag{3.37}$$

As noted before, the tight binding approximation has introduced another gap closing point. The first gap closing happens at $k = 0$ for $\tilde{\mu} = -2\tilde{t}$. In the original parameters, this corresponds to $\mu = 0$ so it is the phase transition found in section 2.2. There is another gap closing for $\tilde{\mu} = 2\tilde{t}$ (or $\mu = \frac{2}{ma^2}$) at $k = \pm\pi$ which indicates another phase transition. The topological non-trivial phase is then limited to a smaller domain in parameter space $|\tilde{\mu}| < 2|\tilde{t}|$ and $\Delta \neq 0$. We will see that this is the case when we next consider the general case and determine the conditions for the existence of zero energy bound states.

3.2.2 General case

The general Hamiltonian for the Kitaev toy model in eq. (3.24) can be written in the form of a matrix like eq. (3.12). We use the anti-commutations relations of the operators a_j to write the Hamiltonian as

$$H = \frac{i}{4}\sum_{j,l=1}^{2N} A_{jl}a_j a_l = \sum_{j,l=1}^{2N} M_{jl}a_j a_l, \tag{3.38}$$

where A is a real anti-symmetric (this means $iA = (iA)^\dagger$ or $A^* = A = -A^T$) and M is hermitian. We can solve the eigenvalue problem by finding the orthogonal transformation WAW^T which bring the Hamiltonian into the canonical form.

$$H = \frac{i}{2}\sum_{j=1}^{N} E_j b'_j b''_j = \sum_{j=1}^{N} E_j (d_j^\dagger d_j - \tfrac{1}{2}), \tag{3.39}$$

where

$$d_j = \frac{1}{2}(b'_j + ib''_j)\ , \qquad d_j^\dagger = \frac{1}{2}(b'_j - ib''_j) \tag{3.40}$$

are fermion operators and b'_j and b''_j are linear combinations of the Majorana operators a_{2k-1} and a_{2k}. We can write this as

$$\begin{pmatrix} b'_1 \\ b''_1 \\ \vdots \\ b'_N \\ b''_N \end{pmatrix} = W \begin{pmatrix} a_1 \\ a_2 \\ \vdots \\ a_{2N-1} \\ a_{2N} \end{pmatrix}, \qquad WAW^T = \begin{pmatrix} 0 & E_1 & & & \\ -E_1 & 0 & & & \\ & & \ddots & & \\ & & & 0 & E_N \\ & & & -E_N & 0 \end{pmatrix} \tag{3.41}$$

where W is a $2N \times 2N$ orthogonal matrix whose rows are eigenvectors of A[11]. The eigenvalues appears in pairs of $\pm E_j$ due to the particle-hole symmetry of the Hamiltonian. If zero energy edge states exist, they are of the form[11]

$$\begin{aligned} b' &= \textstyle\sum_j (\alpha'_+ x_+^j + \alpha'_- x_-^j) c_{2j-1} \\ b'' &= \textstyle\sum_j (\alpha''_+ x_+^{-j} + \alpha''_- x_-^{-j}) c_{2j} \end{aligned}, \qquad x_\pm = \frac{-\tilde{\mu} \pm \sqrt{\tilde{\mu}^2 - 4\tilde{t}^2 + 4\tilde{\Delta}^2}}{2(\tilde{t} + \tilde{\Delta})}, \tag{3.42}$$

where the coefficients α'_+, α'_-, α''_+ and α''_- are determined by the boundary conditions. Hard wall boundary conditions at $j = 0$ and $j = N + 1$ gives these four equations

$$\alpha'_- + \alpha'_+ = 0 \tag{3.43}$$

$$\alpha''_- + \alpha''_+ = 0 \tag{3.44}$$

$$\alpha'_- x_-^{-(N+1)} + \alpha'_+ x_+^{-(N+1)} = 0 \tag{3.45}$$

$$\alpha''_- x_-^{-(N+1)} + \alpha''_+ x_+^{-(N+1)} = 0. \tag{3.46}$$

We consider the two domains $|\tilde{\mu}| > 2|\tilde{t}|$ and $|\tilde{\mu}| < 2|\tilde{t}|$ in order to determine if a zero-energy edge state of the form in eq. (3.42) can satisfy the boundary conditions. In both cases we have $\tilde{\Delta} \neq 0$.

a) In the domain $|\tilde{\mu}| > 2|\tilde{t}|$ we have

$$|x_+| = \left| \frac{1 + \sqrt{1 - \left(\frac{2\tilde{t}}{\tilde{\mu}}\right)^2 + \left(\frac{2\tilde{\Delta}}{\tilde{\mu}}\right)^2}}{\frac{2\tilde{t}}{|\tilde{\mu}|} + \frac{2\tilde{\Delta}}{|\tilde{\mu}|}} \right| > \left| \frac{1 + \frac{2\tilde{\Delta}}{|\tilde{\mu}|}}{\frac{2\tilde{t}}{|\tilde{\mu}|} + \frac{2\tilde{\Delta}}{|\tilde{\mu}|}} \right| > \left| \frac{1 + \frac{2\tilde{\Delta}}{|\tilde{\mu}|}}{1 + \frac{2\tilde{\Delta}}{|\tilde{\mu}|}} \right| = 1 \tag{3.47}$$

$$|x_+ x_-| = \left| \frac{\tilde{\mu}^2 - \tilde{\mu}^2 + 4\tilde{t}^2 - 4\tilde{\Delta}^2}{4(\tilde{t} + \tilde{\Delta})^2} \right| = \left| \frac{\tilde{t} - \tilde{\Delta}}{\tilde{t} + \tilde{\Delta}} \right| < 1, \tag{3.48}$$

where we have used that $\frac{2\tilde{t}}{|\tilde{\mu}|} < 1$. These two equations combines to $|x_-| < 1$. For $\tilde{\mu} > 0$ it will be $|x_+| < 1$ and $|x_-| > 1$. It is therefore not possible to find a normalizable solution with non-zero values for both α'_- and α'_+ (or α''_- and α''_+) that satisfy the boundary conditions and we can conclude that this phase contains no zero energy edge states.

b) For $|\tilde{\mu}| < 2|\tilde{t}|$ we have $|x_+|, |x_-| < 1$ which makes it possible to have a zero-energy bound state of the form given in eq. (3.42) satisfying the boundary conditions with both α'_- and α'_+ (and α''_- and α''_+) non-zero.

Having determined the domain in which Majorana edge modes exist in the Kitaev chain, we turn back to our tight binding model. In our original parameters, the Majorana edge modes exist in the domain

$$0 < \mu < \frac{2}{ma^2} \qquad , \qquad \Delta \neq 0, \tag{3.49}$$

where $a = L/N$ is the lattice constant. We solve the Hamiltonian in 3.12 by numerical diagonalisation and plot the energy spectrum in figure 3.2 as a function of μ with fixed wire length L, pairing potential Δ and mass m. We see that there exists zero energy modes in the expected domain and that they are absent outside the domain. The bulk spectra obtained by numerics and from the analytical expression in (3.13 coincide.
The tight-binding approximation introduced another phase transition point at $\mu = \frac{2}{ma^2}$, which was not present in the p-wave Hamiltonian. We see in figure 3.2 that the energy spectrum is symmetric about $\mu = \frac{1}{ma^2}$. It is therefore only necessary to consider values of $\mu \leq \frac{1}{ma^2}$ since no new information can be obtained for μ larger than this. Increasing the number of lattice sites N will of course make the lattice spacing a smaller and this makes it possible use the tight-binding model to get new information for larger values of μ.

3.3 The eigenmode model

In order to provide further support for the numerical results, we introduce a second method for obtaining numerical results for the p-wave Hamiltonian. This time we work on the original Hamiltonian in eq. (2.8)

$$H = \int \left\{ \Psi^\dagger(x) \left(\frac{-\hbar^2 \partial_x^2}{2m} - \mu \right) \Psi(x) + \frac{1}{4} \left[\Psi^\dagger(x) \Delta(-i\hbar\partial_x) \Psi^\dagger(x) \right. \right. \\ \left. \left. - \left(-i\hbar\partial_x \Psi^\dagger(x)\right) \Delta \Psi^\dagger(x) + \text{h.c.} \right] \right\} \mathrm{d}x \tag{3.50}$$

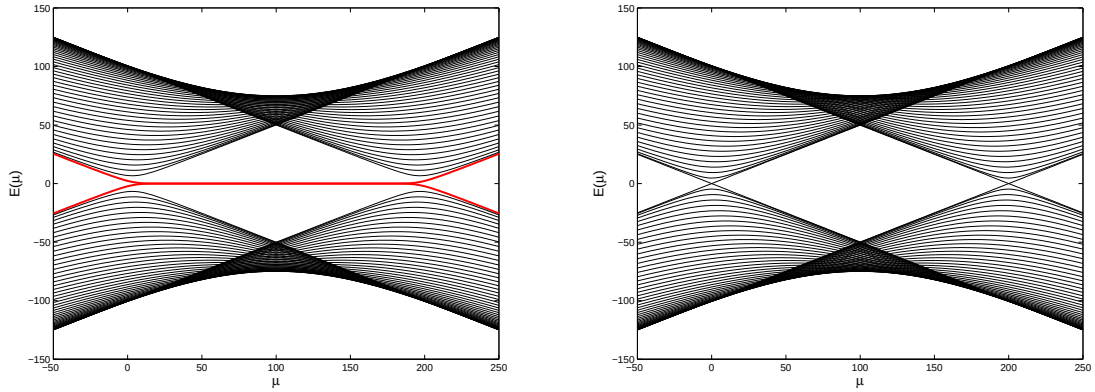

Figure 3.2: Energy spectrum as a function of chemical potential μ for a wire of length $L = 5$, lattice constant $a = L/N = 0.1$, pairing potential $\Delta = 15$ and $m = \hbar = 1$. The left plot is obtained by numerical diagonalisation of eq. (3.12) and the Majorana bound state is highlighted red. The right plot is obtained by evaluating the dispersion relation eq. (3.13).

Choosing our basis to be the eigenmodes of a 1D box of length L, $\Psi(x) = \sqrt{\frac{2}{L}} \sum_{p_n} \sin(p_n x)\, c_{p_n}$ with $p_n = \frac{n\pi}{L}$, we write the Hamiltonian as

$$
\begin{aligned}
H = \sum_{p_n p_m} \Bigg\{ & \frac{2}{L} \int \sin(p_m x) c^\dagger_{p_m} \left(\frac{-\partial_x^2}{2m} - \mu \right) \sin(p_n x) c_{p_n} \\
& + \frac{i}{4} \Big(\sin(p_m x) c^\dagger_{p_m} \Delta \partial_x \sin(p_n x) c^\dagger_{p_n} \\
& \quad - \left(\partial_x \sin(p_m x) c^\dagger_{p_m} \right) \Delta \sin(p_n x) c^\dagger_{p_n} + \text{h.c.} \Big) \Bigg\} \, \mathrm{d}x \qquad (3.51) \\
= \sum_{p_n p_m} & \left(\frac{p_n^2}{2m} - \mu \right) \delta_{p_n p_m} c^\dagger_{p_m} c_{p_n} + \frac{i\Delta}{2L} \Bigg[c^\dagger_{p_m} c^\dagger_{p_n} \Bigg(p_n \int_0^L \sin(p_m x) \cos(p_n x)\, \mathrm{d}x \\
& - p_m \int_0^L \cos(p_m x) \sin(p_n x)\, \mathrm{d}x \Bigg) + \text{h.c.} \Bigg] \qquad (3.52) \\
= \sum_{p_n p_m} & \left(\frac{p_n^2}{2m} - \mu \right) c^\dagger_{p_n} c_{p_n} + \frac{i\Delta}{2L} \left[-2 p_n p_m \frac{1 - \cos\left((p_n - p_m)L\right)}{p_m^2 - p_n^2} c^\dagger_{p_m} c^\dagger_{p_n} + \text{h.c.} \right] \\
= \sum_{p_n p_m} & \left(\frac{p_n^2}{2m} - \mu \right) c^\dagger_{p_n} c_{p_n} + \frac{i\Delta}{2L} \left[-2nm \frac{1 - (-1)^{n-m}}{m^2 - n^2} c^\dagger_{p_m} c^\dagger_{p_n} + \text{h.c.} \right] \qquad (3.53)
\end{aligned}
$$

We note that the symmetric Taylor expansion of $\Psi(x)$ in eq. (4.43) ensures that the Δ-term in eq. (3.53) is anti-symmetric in the indices n, m, as it should be. We write the Hamiltonian

in terms of Nambu spinors

$$H = \frac{1}{2}\vec{c}^{\dagger}\mathscr{H}\vec{c}, \tag{3.54}$$

$$\mathscr{H} = \tau_z \otimes \mathscr{H}_0 + \tau_x \otimes \mathscr{H}_\Delta, \tag{3.55}$$

$$= \begin{bmatrix} \mathscr{H}_0 & i\mathscr{H}_\Delta \\ -i\mathscr{H}_\Delta^T & -\mathscr{H}_0 \end{bmatrix} \tag{3.56}$$

$$(\mathscr{H}_0)_{nm} = \left(\frac{p_n^2}{2m} - \mu\right)\delta_{nm}, \tag{3.57}$$

$$(\mathscr{H}_\Delta)_{nm} = \frac{-2\Delta nm}{L(m^2-n^2)}(1-(-1)^{n-m}), \tag{3.58}$$

where $c^\dagger = (c_{p_0}^\dagger, c_{p_1}^\dagger, \ldots, c_{p_0}, c_{p_1}, \ldots)$ is the Nambu spinor and τ_i are Pauli matrices. The eigenvectors and eigenvalues of the this Hamiltonian can be obtained by numerical diagonalization. As we saw in figure 2.4, the energy spectrum of the eigenmode model coincide with the spectrum obtained by evaluating the analytical expression on eq. (2.16).

Now that we have introduced the two numerical models of the p-wave Hamiltonian, we will proceed to test the models against theoretical predictions.

3.4 Majorana end state in finite wire

We saw in section 3.2 that in a system of finite size, there will be two Majorana edge states one located at each end of the wire. The wave functions of these states decay exponentially from the edge, but there will always be some finite overlap causing the states to hybridize and acquire non-zero energy $\pm E_0$. This interaction between the two edge states can according to Kitaev [11] be described by the effective Hamiltonian

$$H_{\text{eff}} = \frac{i}{2}E_0 b' b'' , \qquad E_0 \propto e^{-\chi L} , \qquad \chi = \min(|\ln|x_+||\,, |\ln|x_-||) \tag{3.59}$$

where L is the length of the wire and $x_\pm$ are given in (3.42). Using the tight binding model and the eigenmode model we compute the energy eigenvalue E_0 of the Majorana edge state as a function of L and plot the result in figure 3.3. Both models agree with the theoretical prediction of eq. (3.59), except in the case of a very short wire, where finite size effects lead to deviations. The rounding errors in the numerics becomes non-negligible when the wire becomes very long which we see in the figure as the data starts to oscillate randomly for large L. We will therefore have to pay attention to the finite size effects and pick parameters carefully to avoid rounding errors if we need very precise values of the Majorana state energy in our future investigations. A smaller value of Δ was used in the eigenmode model in order to keep the required computational matrix size N of a feasible size and we will comment on this in section 3.5.

However, this is not the complete picture of how the Majorana end state energy depends on the wire length. It is shown in [21] for a continuous model, that the energy of the Majorana end state oscillates as a function of wire length besides the exponential decay and the oscillations have the form

$$E_0 \propto |\sin(p_F L)|, \tag{3.60}$$

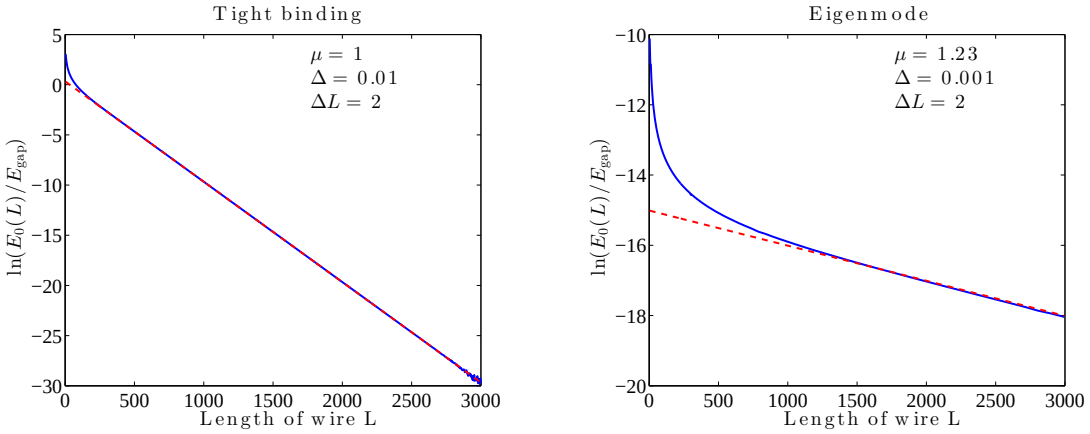

Figure 3.3: Lowest energy eigenvalue E_0 as a function of the length of the wire L obtained by numerical diagonalization. Other parameters are $m = \hbar = 1$. The lattice constant is $a = 1$ in the tight-binding model and the computational matrix size $N \propto L$ in the eigenmode model. The red dashed line is the theoretical prediction from (3.59) and E_{gap} is given in eq. (3.74). Note the difference in scale on the y-axis and value of Δ.

where p_F is the Fermi momentum. In figure 3.3, the parameters were chosen such that $p_F = \pi/2$ and the oscillations are therefore not observable for the chosen sampling rate $\Delta L = 2$.

We will now derive the period of these oscillations using a rather naive but very simple approach. We look for a bound edge state solution with finite energy $E_0 > 0$ in a finite wire of length L with hard wall boundary conditions. That is we use the same procedure as in section 2.3 to solve the Scrödinger equation in eq. (2.20), but now we look for solutions of finite energy $E_0 > 0$. We then obtain a secular equation

$$\lambda_\pm = \frac{m\Delta}{\hbar}\left(1 \pm \sqrt{1 - 2\frac{(\mu + E_0)}{m\Delta^2}}\right) \tag{3.61}$$

The hard wall boundary conditions gives us two equations that the wavefunction $\phi(x)$ must satisfy: $\phi(x = 0) = \phi(x = L) = 0$. We have used the same trial function as in the case of the semi-infinite wire and by constructing a solution of the same form as in eq. (2.26) the condition $\phi(x = 0) = 0$ is automatically satisfied. In order to satisfy $\phi(x = L) = 0$, $\lambda_\pm$ must have a non-zero imaginary part which we define as

$$\pm\theta \equiv \text{Im}(\lambda_\pm) = \text{Im}\left(\pm\frac{m\Delta}{\hbar}\sqrt{1 - 2\frac{(\mu + E_0)}{m\Delta^2}}\right). \tag{3.62}$$

The imaginary must satisfy $\theta = i\frac{\pi}{L}n$ for $n \in \mathbb{N}$ in order to obtain a solution which satisfies $\phi(x = L) = 0$. $\lambda_\pm$ has a non-zero imaginary part when the radicand in eq. (3.61) is negative:

$$1 - 2\frac{(\mu + E_0)}{m\Delta^2} < 0. \tag{3.63}$$

Assuming this equation holds θ is given by

$$\theta = \frac{i}{\hbar}\sqrt{2m(\mu + E_0) - m\Delta^2}. \tag{3.64}$$

We write the equation $\theta = i\frac{\pi}{L}n$ and solve for E_0:

$$\begin{aligned} i\frac{\pi}{L}n &= \frac{i}{\hbar}\sqrt{2m(\mu + E_0) - m\Delta^2} \\ &\Downarrow \\ E_0(n) &= \frac{\pi^2 n^2 \hbar^2}{2L^2 m} + \frac{m\Delta^2}{2} - \mu \qquad \text{for} \qquad n \in \mathbb{N}. \end{aligned} \tag{3.65}$$

This looks like an equation for the allowed energies of a particle in a box. There is of course only a single bound edge state at each end of the wire and not an entire spectrum as the equation would suggest. We therefore define E_0 to be the smallest $|E_0(n)|$ of all possible n:

$$E_0 \equiv \min(|E_0(n)|). \tag{3.66}$$

In figure 3.4 we plot E_0 with the numerically obtained values of the Majorana state as a function of wire length. We see that even though the values of E_0 and the numerics does not coincide they both oscillates with the same frequency. We find the period of the oscillations by setting $E_0(n) = 0$ and solve for L:

$$\begin{aligned} 0 &= \frac{\pi^2 n^2 \hbar^2}{2L^2 m} + \frac{m\Delta^2}{2} - \mu \\ &\Downarrow \\ L(n) &= \frac{\pi\hbar}{\sqrt{2m\mu - m^2\Delta^2}}n, \end{aligned} \tag{3.67}$$

which tells us the period P is

$$P = \frac{\pi}{p'_F}, \tag{3.68}$$

where

$$p'_F = \sqrt{2m\mu - m^2\Delta^2} \tag{3.69}$$

is the modified Fermi momentum.

This is in agreement with the findings of Brouwer *et.al.* [21] that the lowest energy state oscillates as a function of wire length with a period π/p_F in the limit $2\mu \gg m\Delta^2$, as written in eq. (3.60). The Fermi momentum is usually defined as $p_F = \sqrt{2\mu m}$, but if $2\mu \gg m\Delta^2$ does not hold, the modified Fermi momentum in eq. (3.69) should be used instead. In the TBA, the momentum has been approximated by $p^2 \to \frac{4}{a^2}\sin^2\left(\frac{pa}{2}\right)$, and the modified Fermi momentum is instead given by

$$p'_{F,\mathrm{TBA}} = \frac{2}{a}\arcsin\left(\sqrt{\frac{(2\mu m - \Delta^2 m^2)a^2}{4}}\right) \xrightarrow{2\mu \gg m\Delta^2} p_{F,\mathrm{TBA}} = \frac{2}{a}\arcsin\left(\sqrt{\frac{\mu m a^2}{2}}\right) \tag{3.70}$$

In figure 3.5 we see the oscillating behaviour of the lowest energy eigenvalue for both the tight-binding model and the eigenmode model. The parameters have been tuned such that

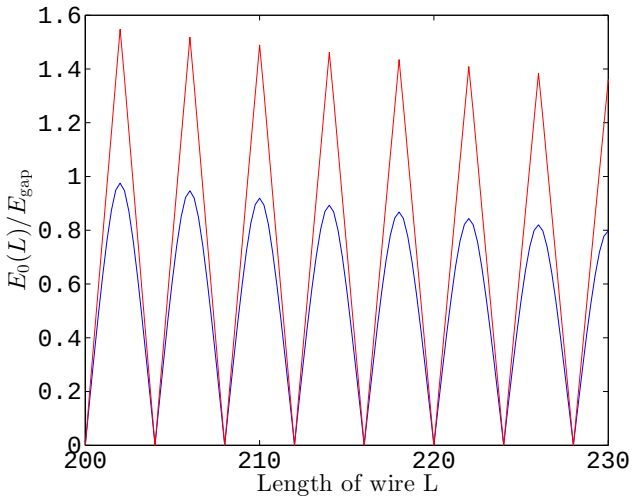

Figure 3.4: Oscillating behaviour of the lowest energy eigenvalue E_0 as a function of the length of the wire L. The red line is obtained by evaluating eq. (3.66) while the blue line is obtained using the eigenmode model. Parameters are $\mu = 0.3084$, $\Delta = 5 * 10^{-3}$, sampling rate $\Delta L = \frac{1}{4}$ and $m = \hbar = 1$.

the period of the oscillations are $P = 4$ for both models. The value of the chemical potential is found by inserting eq. (3.68) into equation (3.69) and (3.70) and solving for μ with $P = 4$. The result is

$$\mu^{\text{TB}}\Big|_{P=4} = \frac{1}{2m}\left(\frac{4}{a^2}\sin\left(\frac{\pi a}{8}\right)^2 + m^2\Delta^2\right) \tag{3.71}$$

$$\mu^{\text{EIG}}\Big|_{P=4} = \frac{1}{2m}\left(\frac{\pi^2}{4} + m^2\Delta^2\right) \tag{3.72}$$

where TB refer to tight-binding and EIG to eigenmode. A smaller sampling rate has been chosen to make the oscillations more detailed and we see that the numerics agree with predicted period of the oscillations.

In the figures of this section we have normalized E_0 by the energy gap E_{gap} which is the minimum of the dispersion relation $E_+(p)$ in eq. (2.16). E_{gap} is found by solving $\frac{\partial E_+(p)}{\partial p}\Big|_{p=p^*} = 0$ for p^* (neglecting the solution $p^* = 0$) and inserting p^* back into $E_+(p)$:

$$\frac{\partial E_+(p)}{\partial p}\Big|_{p=p^*} = 0 \quad \Rightarrow \quad p^* = \sqrt{2m(\mu - \Delta^2 m)} \tag{3.73}$$

$$E_{\text{gap}} = E_+(p^*) = \Delta\sqrt{2m\mu - \Delta^2 m}. \tag{3.74}$$

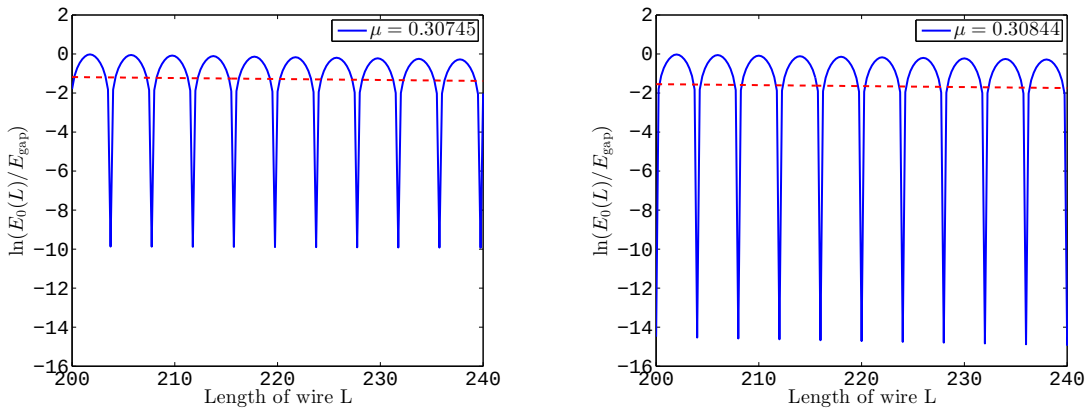

Figure 3.5: Oscillating behaviour of the lowest energy eigenvalue E_0 as a function of the length of the wire L. Left plot is obtained from the tight binding model for lattice constant $a = \frac{1}{4}$. The right plot is obtained from the eigenmode model. For both plots the other parameters are: $\Delta = 10^{-3}$, sampling rate $\Delta L = \frac{1}{4}$, $m = \hbar = 1$ and μ is determined by eq. (3.71) and eq. (3.72) such that the period $P = 4$. The red dashed line is the theoretical prediction from (3.59), and E_{gap} is given in (3.74)

3.5 Comparison of the tight binding model and the eigenmode model

Both numerical methods have some finite numerical precision as well as a restricted domain in parameter space where they give accurate results, due to the finite size of the computational matrices. In this section we will compare the two numerical methods, discuss their different advantages and drawbacks, and locate the domains in parameter space where they give accurate results.

In section 3.2 we saw that the tight binding approximation changes the phase diagram such that there are two topological phase transition points. In the p-wave Hamiltonian there is only one phase transition point at $\mu = 0$ while the tight-binding approximation introduces another phase transition at $\mu = \frac{2}{ma^2}$ where m is the mass and $a = L/N$ is the lattice constant. The phase diagram of the tight binding model is symmetric about $\mu = \frac{1}{ma^2}$. Hence in the tight-binding model we gain no new information by considering μ-values beyond this point. This does however not mean that large values of μ cannot be studied in the tight binding model. In order to do so, the computational matrix size N has to be increased while the length of the wire is kept constant such that the lattice constant a becomes smaller.

In the left plot of figure 3.6, the energy of the Majorana end state and the first bulk state are computed by the tight binding model and the eigenmode model as a function of chemical potential μ. In agreement with the findings in section **??**, the tight binding model goes through another topological phase transition at $\mu = \frac{2}{ma^2}$, where the model goes into the non-topological phase and the zero energy state disappears. We also see that the spectrum of the tight-binding model is symmetric about $\mu = \frac{1}{ma^2}$, as we also observed in figure 3.2. The oscillations of the Majorana state energy is a finite size effect as discussed in section 3.4.

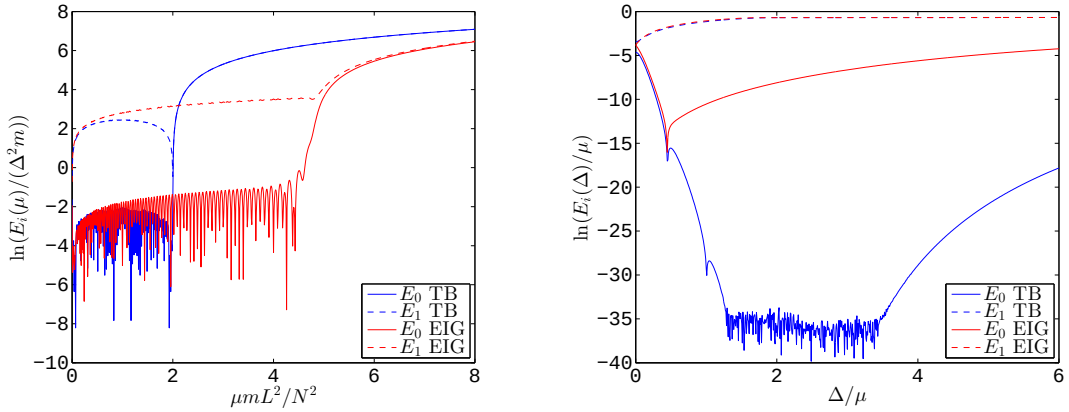

Figure 3.6: Energy (E_i) of the Majorana end state (solid line) and the first bulk state (dashed line) computed with the tight binding model (blue) and eigenmode model (red) as a function of chemical potential μ (left) and pairing potential Δ (right). Both plots are computed for $L = 100$, $m = \hbar = 1$ and $N = 100$. In the left plot the pairing potential is fixed at $\Delta = 0.05$, and in the right plot the chemical potential is fixed at $\mu = 0.25$. The oscillations of the Majorana state energy in the left plot is due to the finite size effect described in section 3.4.

The Majorana end states are well described by the eigenmode model up until

$$\mu \approx \left(\frac{\pi N \hbar}{L}\right)^2 \frac{1}{2m} \tag{3.75}$$

where the Fermi momentum p_F becomes larger than the eigenmode momentum cut-off $p_N = \pi N/L$. This happens because the low-energy degrees of freedom relevant for the Majorana states are at the Fermi momentum. When p_F becomes larger than p_N the states at the Fermi momentum are not included in the model and the Majorana states looses their support. The value of μ where this happens is found by solving $p_F = p_N$ for μ. Increasing the computational matrix size N will enable the eigenmode model to give accurate results for larger values of μ.

In the right plot of figure 3.6, the energy is now computed as a function of pairing potential Δ. We expect the Majorana energy E_0 to decrease for increasing pairing potential, but this might not be obvious. Consider the localization length of the Majorana end state which is given by the coherence length of the superconductor $\xi = (m\Delta)^{-1}$. This can understood by considering the factor of $m\Delta$ outside the parenthesis in eq. (3.61) which determines how fast wavefunction of the Majorana bound state decays from the edge. A stronger pairing potential leads to a smaller localization length, which in turn leads to a smaller Majorana energy due to a smaller overlap between the wavefunctions of the Majorana bound states at opposite end of the wire.

In the right plot of figure 3.6, we see that for a fixed wire length L and computational matrix size N, the Majorana energy decreases with increasing Δ for both models at small Δ, but the tight binding model can describe the Majorana state energy accurately for a larger range of Δ than the eigenmode model. At some point the tight binding model saturates at $E_0/\mu \sim 10^{-35}$, where the numerical precision is the limiting factor, until the Majorana state energy start to increase again when the size of the computational matrix is too small to

provide adequate support for the Majorana. When numerical precision has been reached the eigenvalues smaller than the precision limit will be equivalent to zero and *e.g.* the eigenvectors still contain sensible information.

To get a better understanding of the required computational needed to capture the Majorana physics we plot the Majorana energy E_0 and the energy of the first bulk state E_1 as a function of computational matrix size N in figure 3.7. As discussed above, the computational matrix size in the eigenmode model needs to be large enough that the Fermi momentum is less than the eigenmode cut-off. In the tight-binding model for a fixed wire length L and chemical potential $\mu > 0$, the computational matrix size N must be of a size such that the lattice spacing $a = L/N$ is small enough to satisfy $\mu < \frac{2}{ma^2}$ if the system is to be in the topological non-trivial phase.

In figure 3.7 we see that the energies decrease for increasing N, but eventually converges toward some fixed value when N reaches a certain size. How fast this convergence happens depends on Δ and when it happens depends on μ. By comparing figure 3.7a and 3.7c or figure 3.7b and 3.7d, we see that changing μ will not alter the shape of the curves but only the scale of x-axis. On the contrary, changing Δ has a large impact on have fast E_0 converges in the eigenmode model. Generally, E_0 start to decrease at smaller N in the eigenmode model than in the tight-binding model. In which of the models E_0 converges first depends on the value of the pairing potential Δ. The eigenmode model converges faster for smaller values Δ while the tight binding model converges faster for larger values. For even larger values of Δ the required computational matrix size in the eigenmode model may be to large to perform on the available computers.

The tight binding model can quite easily describe a localised wave function while the eigenmode model apparently requires a larger number of eigenmodes for large Δ to give an equally accurate description of very localised states. Disorder however will delocalize the Majoranas, as we will see in the next chapter, and we will still be able to get accurate result using the eigenmode model without increasing the computational matrix size as much as it seems to be required from the clean wire case.

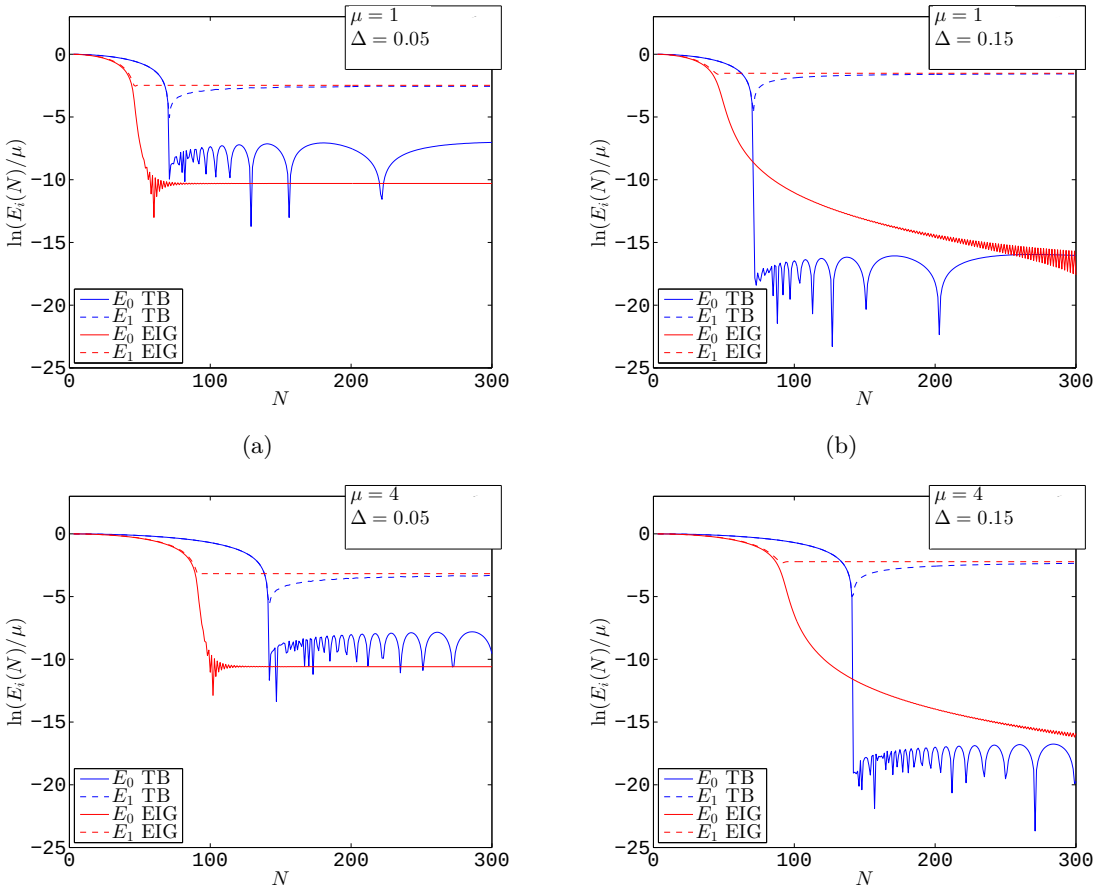

Figure 3.7: Energy of the Majorana end state (E_0) and the first bulk state (E_1) computed with the tight binding model (TB) and eigenmode model (EIG) as a function of computational matrix size N with sampling rate $\Delta N = 1$ for different values Δ and μ, but fixed wire length $L = 100$. The oscillations of the Majorana energies in the tight-binding model is due to the finite wire size oscillation described in section 3.4.

Chapter 4

The p-wave Hamiltonian with disorder

In this chapter we will introduce a model for a disordered 1D p-wave superconductor and investigate how disorder affects the Majorana edge states. Two types of disorder will be introduced: Disorder in the positions dependent chemical potential and in the pairing potential. We implement both types of disorder in both the tight-binding model and the eigenmode model and compare numerical results with theoretical predictions from the literature. We will focus on chemical potential disorder while pairing potential disorder is only examined in minor detail.

4.1 Disorder potential

Disorder in quantum wires can arise in different ways such as imperfections in the atomic crystal structure of the wire or an induced disorder potential by the substrate on which the wire is placed. We will simulate this type of disorder by a Gaussian distributed random chemical potential $\delta\mu(x)$.

The superconducting gap is proximity induced by either placing the quantum wire on a superconductor or coating the wire with a superconductor. The interface between the wire and the superconductor must be perfect in order to induce a hard superconducting gap into the wire. If the interface is imperfect, the induced superconducting gap will vary along the wire. We will model this by a uniform distributed random pairing potential $\Delta(x)$.

4.1.1 Chemical potential disorder

We model the disordered chemical potential $\delta\mu(x)$ as potential consisting of $N_{\delta\mu}$ intervals of length $L/N_{\delta\mu}$. Each interval is of constant value $\delta\mu_j$ which is a Gaussian distributed random variable. This is illustrated in figure 4.1. The Hamiltonian then consist of the two usual terms plus a third:

$$H = H_0 + H_\Delta + H_{\delta\mu}, \tag{4.1}$$

$$H_{\delta\mu} = \int \Psi^\dagger(x)\delta\mu(x)\Psi(x)\,\mathrm{d}x, \tag{4.2}$$

and the disorder potential is modelled as

$$\delta\mu(x) = \sum_{j=1}^{N_{\delta\mu}} \text{rect}\left(\frac{x - a\left(j - \frac{1}{2}\right)}{a}\right)\delta\mu_j, \tag{4.3}$$

where $\text{rect}\left(\frac{x-X}{Y}\right)$ is a rectangular function of height 1, centred at X and of width Y and $a = \frac{L}{N_{\delta\mu}}$. It can also be defined in terms of the Heavyside step function Θ, as $\text{rect}\left(\frac{x-X}{Y}\right) = \Theta(x - X + \frac{Y}{2}) - \Theta(x - X - \frac{Y}{2})$. The $\delta\mu_j$'s are drawn from independent Gaussian distributions with mean zero and variance V_μ^2, *i.e.*

$$dP(\delta\mu_j) \propto \prod_j \exp\left(-\frac{|\delta\mu_j|^2}{2V_\mu^2}\right) d\delta\mu_j. \tag{4.4}$$

V_μ is called the disorder amplitude. We will need the correlator $\langle\delta\mu(x)\delta\mu(x')\rangle$ of the disorder potential later, so we might just as well calculate it now.

$$\begin{aligned}
\langle\delta\mu(x)\delta\mu(x')\rangle &= \sum_{n,j=1}^{N_{\delta\mu}} \text{rect}\left(\frac{x - a\left(n - \frac{1}{2}\right)}{a}\right)\text{rect}\left(\frac{x' - a\left(j - \frac{1}{2}\right)}{a}\right)\langle\delta\mu_n\delta\mu_j\rangle \\
&= \sum_{n,j=1}^{N_{\delta\mu}} \text{rect}\left(\frac{x - a\left(n - \frac{1}{2}\right)}{a}\right)\text{rect}\left(\frac{x' - a\left(j - \frac{1}{2}\right)}{a}\right)V_\mu^2\delta_{n,j} \\
&= \sum_{j=1}^{N_{\delta\mu}} \text{rect}\left(\frac{x - a\left(j - \frac{1}{2}\right)}{a}\right)\text{rect}\left(\frac{x' - a\left(j - \frac{1}{2}\right)}{a}\right)V_\mu^2,
\end{aligned} \tag{4.5}$$

where $\langle\delta\mu_n\delta\mu_j\rangle = V_\mu^2\delta_{n,j}$ because $\delta\mu_n$ and $\delta\mu_j$ are completely uncorrelated for $n \neq j$ and perfectly correlated for $n = j$. It is clear that this sum is different from zero only when x, $x' \in [an, a(n+1)]$, $n \in [0, N-1]$, in which case it is equal to V_μ^2. We rewrite eq. (4.5) in order to consider the limit where $a \to 0$,

$$\langle\delta\mu(x)\delta\mu(x')\rangle = \sum_{j=1}^{N_{\delta\mu}} \frac{1}{a}\text{rect}\left(\frac{x - a\left(j - \frac{1}{2}\right)}{a}\right)\frac{1}{a}\text{rect}\left(\frac{x' - a\left(j - \frac{1}{2}\right)}{a}\right)a^2V_\mu^2. \tag{4.6}$$

In the limit of $a \to 0$ we can exchange $aj \to y$; $a\sum_{j=1}^{N_{\delta\mu}} \to \int_0^L \text{d}y$ and the rectangular functions becomes delta functions,

$$\lim_{a\to 0}\left(\frac{1}{a}\text{rect}\left(\frac{x - a\left(j - \frac{1}{2}\right)}{a}\right)\right) = \delta(x - x_j), \tag{4.7}$$

and the correlator becomes

$$\lim_{a\to 0}\langle\delta\mu(x)\delta\mu(x')\rangle = aV_\mu^2\int_0^L \delta(x - y)\delta(x' - y)\,\text{d}y. \tag{4.8}$$

We define the disorder strength $\gamma_\mu = aV_\mu^2$ to remain constant in the limit $a \to 0$ and perform the integration to get

$$\lim_{a\to 0}\langle\delta\mu(x)\delta\mu(x')\rangle = \delta(x - x')\gamma_\mu. \tag{4.9}$$

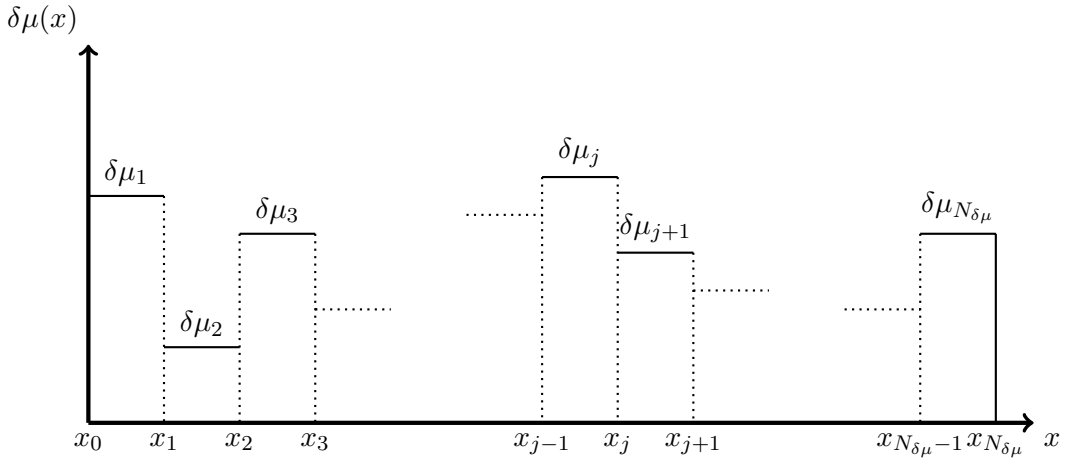

Figure 4.1: The potential $\delta\mu(x)$ along the 1D superconductor. The superconductor is divided into $N_{\delta\mu}$ pieces of length $\frac{L}{N_{\delta\mu}}$ between the endpoints $x_0 = 0$ and $x_{N_{\delta\mu}} = L$, and each piece has a corresponding $\delta\mu_j$ which is given by a Gaussian distributions, independent of the other $\delta\mu_j$'s.

4.1.2 Pairing potential disorder

Disorder in the pairing potential is included in a similar manner, only this time we redefine Δ as a space dependent function instead of adding another term to the Hamiltonian. The disordered pairing potential $\Delta(x)$ is a potential consisting of N_Δ intervals of length L/N_Δ. Each interval is of constant value Δ_j which is a uniformly distributed random variable. This potential is of the same form as $\delta\mu(x)$ pictured in figure 4.1, but Δ_j is uniformly distributed as opposed to $\delta\mu_j$ which is Gaussian distributed. Explicitly, we model the disordered pairing potential as

$$\Delta(x) = \sum_{j=1}^{N_\Delta} \text{rect}\left(\frac{x - a\left(n - \frac{1}{2}\right)}{a}\right)\Delta_j, \tag{4.10}$$

where $a = \frac{L}{N_\Delta}$, $\langle\Delta(x)\rangle = \Delta$ and the Δ_j's are independently uniformly distributed variables on the interval $[\Delta - V_\Delta\,;\,\Delta + V_\Delta]$, *i.e.*

$$\mathrm{d}P(\Delta_j) \propto \prod_j \frac{1}{2V_\Delta}\,\mathrm{d}\Delta_j. \tag{4.11}$$

The variance of Δ_j is $\text{var}(\Delta_j) = \frac{V_\Delta^2}{3}$ and the correlator of the disordered pairing potential is

$$\lim_{a\to 0}\langle\Delta(x)\Delta(x')\rangle = \gamma_\Delta\delta(x - x'), \tag{4.12}$$

where $\gamma_\Delta = \frac{1}{3}aV_\Delta^2$ is the disorder strength of the disordered pairing potential.

4.1.3 Mean free path

In order to compare numerical results of our two models with predictions from the literature, we need the mean free path l associated with the life time (not the conduction) of states close

to the Fermi momentum in a disorder potential. The mean free path l can be found from the scattering time τ by $l = \tau v_F$ where v_F is the Fermi velocity. We calculate the scattering time by using Fermi's golden rule [22], under the assumption that the disorder potential $\delta\mu(x)$ scatters momentum states into states of same energy *i.e.* elastic scattering and that $\Delta = 0$. The inverse transition rate is to first order given by

$$\tau_{k'}^{-1} = \frac{2\pi}{\hbar} \sum_k \left|\langle k'|H_{\delta\mu}|k\rangle\right|^2 \delta(\epsilon_{k'} - \epsilon_k). \tag{4.13}$$

$H_{\delta\mu}$ is written in real space in eq. (4.2), so we write the momentum states in real space, $|k\rangle = c_k\,{}^\dagger|\,0\rangle = \frac{1}{\sqrt{L}}\int_0^L e^{-ikx}\Psi^\dagger(x)\,\mathrm{d}x\,|0\rangle$. Inserting this gives us

$$\begin{aligned}
\langle k'|H_{\delta\mu}|k\rangle &= \frac{1}{L}\langle 0|\int \left(e^{ik'x}\Psi(x)\right)\left(\delta\mu(x')\Psi^\dagger(x')\Psi(x')\right)\left(e^{-ikx''}\Psi^\dagger(x'')\right)\,\mathrm{d}x\,\mathrm{d}x'\,\mathrm{d}x''|0\rangle \\
&= \frac{1}{L}\int e^{ik'x-ikx''}\delta\mu(x')\langle 0|\left(\delta(x-x') - \Psi^\dagger(x')\Psi(x)\right) \\
&\qquad\qquad \times\left(\delta(x'-x'') - \Psi^\dagger(x'')\Psi(x')\right)|0\rangle\,\mathrm{d}x\,\mathrm{d}x'\,\mathrm{d}x'' \\
&= \frac{1}{L}\int e^{ik'x-ikx''}\delta\mu(x')\delta(x-x')\delta(x'-x'')\,\mathrm{d}x\,\mathrm{d}x'\,\mathrm{d}x'' \\
&= \frac{1}{L}\int e^{ix'(k'-k)}\delta\mu(x')\,\mathrm{d}x',
\end{aligned} \tag{4.14}$$

where we have used that the anti-commutation relation is $\{\Psi^\dagger(x), \Psi(x')\} = \delta(x-x')$, that the action of the annihilation operator on the vacuum state returns zero $\Psi(x)|0\rangle = 0$, and that the basis states are normalized $\langle 0|0\rangle = 1$. We then proceed to calculate

$$\begin{aligned}
\langle k'|H_{\delta\mu}|k\rangle\langle k|H_{\delta\mu}|k'\rangle &= \frac{1}{L^2}\int \langle\delta\mu(x)\delta\mu(x')\rangle \exp\left(i(x-x')(k'-k)\right)\,\mathrm{d}x\,\mathrm{d}x' \\
&= \frac{V_\mu^2}{L^2}\sum_{j=1}^{N_{\delta\mu}}\int_{x_{j-1}}^{x_j} \exp\left(i(x-x')(k'-k)\right)\,\mathrm{d}x\,\mathrm{d}x' \\
&= \frac{V_\mu^2}{L^2}\sum_{j=1}^{N_{\delta\mu}}\frac{1}{(k'-k)^2}\left(e^{ix_j(k'-k)} - e^{ix_{j-1}(k'-k)}\right)\left(e^{-ix_j(k'-k)} - e^{-ix_{j-1}(k'-k)}\right) \\
&= \frac{V_\mu^2 N_{\delta\mu}}{L^2(k'-k)^2}\left(2 - \exp\left(i(x_j - x_{j-1})(k'-k)\right)\right. \\
&\qquad\qquad \left. - \exp\left(-i(x_j - x_{j-1})(k'-k)\right)\right) \\
&= \frac{2V_\mu^2}{La(k'-k)^2}\left(1 - \cos\left(a(k'-k)\right)\right),
\end{aligned} \tag{4.15}$$

where we inserted eq. (4.6) and used $a = \frac{L}{N_{\delta\mu}}$ and $x_j - x_{j-1} = \frac{jL}{N_{\delta\mu}} - \frac{(j-1)L}{N_{\delta\mu}} = \frac{L}{N_{\delta\mu}} = a$. We now plug back into eq. (4.13),

$$\tau_{k'}^{-1} = \frac{4\pi V_\mu^2}{\hbar La}\sum_k \frac{1}{(k'-k)^2}\left(1 - \cos\left(a(k'-k)\right)\right)\delta(\epsilon_{k'} - \epsilon_k). \tag{4.16}$$

We assume that L is large, so $\frac{2\pi}{L} = \mathrm{d}k$ is small, and convert the sum into an integral and rewrite the delta function using

$$\delta(f(x)) = \sum_i \frac{\delta(x - x_i)}{\left|\frac{\mathrm{d}f(x)}{\mathrm{d}x}\Big|_{x=x_i}\right|} \tag{4.17}$$

where $f(x_i) = 0$:

$$\tau_{k'}^{-1} = \frac{2V_\mu^2}{\hbar a} \int \frac{1}{(k'-k)^2} \left(1 - \cos\left(a(k'-k)\right)\right) \sum_{k''=\pm k'} \frac{\delta(k-k'')}{\left| \frac{\mathrm{d}\epsilon_k}{\mathrm{d}k} \Big|_{k=k''} \right|} \, \mathrm{d}k. \tag{4.18}$$

The differential of ϵ_k is taken in the non-superconducting case ($\Delta = 0$), so

$$\left| \frac{\mathrm{d}\epsilon_k}{\mathrm{d}k} \Big|_{k=k''} \right| = \left| \frac{m}{k''} \right|^{-1}. \tag{4.19}$$

We insert this and perform the integral gives

$$\begin{aligned} \tau_{k'}^{-1} &= \frac{2V_\mu^2}{\hbar a} \int \frac{1}{(k'-k)^2} \left(1 - \cos\left(a(k'-k)\right)\right) \frac{m}{k'} \left(\delta(k-k') + \delta(k+k')\right) \, \mathrm{d}k \\ &= \frac{2mV_\mu^2}{\hbar a k'} \left(\frac{1 - \cos\left(a(k'-k)\right)}{(k'-k)^2} \Big|_{k=k'} + \frac{1 - \cos(2ak')}{4k'^2} \right). \end{aligned} \tag{4.20}$$

Because both the numerator and the denominator in the first fraction in the parenthesis goes to zero when $k = k'$, we have to take care of this term by considering the limit $k \to k'$. To do this, we use l'Hôpital's rule $\lim_{x\to x_0} \frac{f(x)}{g(x)} = \lim_{x\to x_0} \frac{f'(x)}{g'(x)}$, where $f(x_0) = g(x_0) = 0$:

$$\begin{aligned} \lim_{k\to k'} \frac{1 - \cos(a(k'-k))}{(k'-k)^2} &= \lim_{k\to k'} \frac{a \sin(a(k'-k))}{2(k'-k)} \\ &= \lim_{k\to k'} \frac{a^2 \cos(a(k'-k))}{2} \\ &= \frac{a^2}{2}. \end{aligned} \tag{4.21}$$

The limit is well defined and we can find a closed expression for the inverse transition rate

$$\tau_{k'}^{-1} = \frac{maV_\mu^2}{\hbar k'} \left(1 + \frac{\sin^2(ak')}{(ak')^2}\right), \tag{4.22}$$

where we have rewritten $1 - \cos(2ak') = 2\sin^2(ak')$. We can then find the mean free path from $l = v_F \tau_{k_F}$, where $k_F = \hbar^{-1}\sqrt{2m\mu}$ is the Fermi wavenumber and $v_F = \hbar k_F m^{-1}$ is the Fermi velocity:

$$l = \frac{v_F^2}{\gamma} \left(1 + \frac{\sin^2(ak_F)}{(ak_F)^2}\right)^{-1} \tag{4.23}$$

$$= \frac{2\mu}{m\gamma} \left(1 + \frac{\sin^2(a\sqrt{2m\mu})}{2a^2 m\mu}\right)^{-1}. \tag{4.24}$$

We consider the limit $a \to 0$ while keeping $\gamma =$ cosntant. By applying l'Hôpital's rule again we find

$$\lim_{a\to 0} l = \frac{v_F^2}{2\gamma_\mu} \tag{4.25}$$

where γ_μ is the strength of the disorder potential discussed in section 4.1.1.

4.1.4 Disorder in the tight-binding model

In the tight-binding model, the disorder potential $\delta\mu(x)$ is a simple random onsite potential

$$\mu \to \mu + \delta\mu_i, \tag{4.26}$$

with no correlation between different sites,

$$\langle \delta\mu_i \delta\mu_j \rangle = \delta_{ij} V_\mu^2 a, \tag{4.27}$$

where a is the lattice constant. The random potential therefore only changes the diagonal elements in the tight-binding Hamiltonian:

$$H = \frac{1}{2}\vec{\tilde{c}}^\dagger \mathcal{H} \vec{\tilde{c}}, \tag{4.28}$$

$$\mathcal{H} = \begin{bmatrix} D_1 & T & 0 & 0 & \cdots & 0 \\ T^\dagger & D_2 & T & 0 & \cdots & 0 \\ 0 & T^\dagger & D_3 & T & \cdots & 0 \\ \vdots & \vdots & \ddots & \ddots & \ddots & \vdots \\ 0 & 0 & 0 & T^\dagger & D_{N-1} & T \\ 0 & 0 & 0 & 0 & T^\dagger & D_N \end{bmatrix} \tag{4.29}$$

$$D_i = \left(\frac{1}{ma^2} - \mu - \delta\mu_i \right) \tau_z \,, \qquad T = -\frac{1}{2ma^2}\tau_z - \frac{i\Delta}{2a}\tau_x. \tag{4.30}$$

We assume that disorder in the pairing potential can be included in a similar manner, such that

$$\Delta \to \Delta + \delta\Delta_i \,, \qquad i = 1, ..., N-1 \tag{4.31}$$

where

$$\langle \delta\Delta_i \delta\Delta_j \rangle = \frac{1}{3} V_\Delta^2 a, \tag{4.32}$$

because the $\delta\Delta_i$'s are independent and uniformly distributed on the interval $[-V_\Delta, V_\Delta]$ instead of Gaussian distributed. This changes

$$T \to T_i = -\frac{1}{2ma^2}\tau_z - \frac{i(\Delta + \delta\Delta_i)}{2a}\tau_x, \tag{4.33}$$

in the matrix in eq. (4.30).

Generic examples of the spacial distribution of the wave function of the Majorana bound state and the first bulk state can be seen for different disorder strengths in figure 4.2 (chemical potential disorder) and 4.3 (pairing potential disorder). We see that the wavefunction of the Majorana bound state is located at both ends of the wire. This is because the eigenvector of the Majorana bound state is a superposition of the Majorana bound states at each end in this basis. A different basis where the wavefunction of the two Majoranas are located at opposite ends can be choosen.

In the case of no disorder, the wavefunction of the first bulk state is located throughout the wire, but the wavefunction becomes localized as disorder is introduced. The wavefunction of the Majorana is also affected by the disorder potential but not to the same extend as the bulk state.

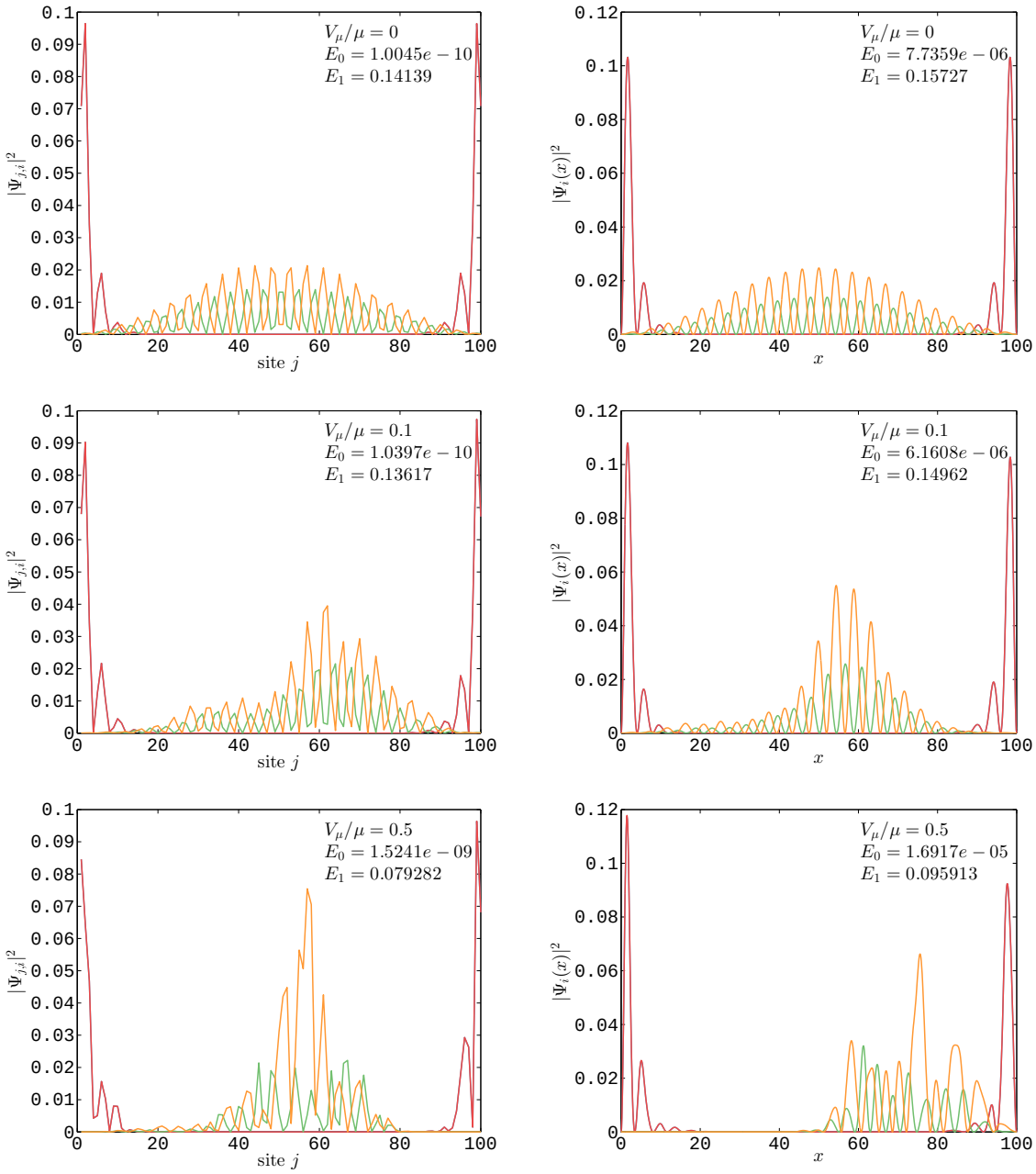

Figure 4.2: Absolute squared values of eigenvectors for eigenvalues Majorana bound state (red) and first bulk state (green and yellow) obtained from the tight-binding model (left) and eigenmode model (right) for a single disorder configuration and for three different disorder amplitudes V_μ. Each eigenvector consist of an electron part and a hole part, which are plotted independently. There is only one curve for the Majorana as the electron and hole parts of its eigenvector are distributed equally. The energy eigenvalues of the Majorana E_0 and first bulk state E_1 for each disorder configuration is written in the plots. Other parameters are $m = 1$, $L = 100$, $a = 1$, $\Delta = 0.2$ and $\mu = 0.3$.

4.1.5 Disorder in the eigenmode model

In order to include the two disorder models in the eigenmode model we have to find their representation in the eigenmode basis. We start with the disordered chemical potential given in eq. (4.3):

$$H = H_0 + H_\Delta + H_{\delta\mu}, \tag{4.34}$$

$$\begin{aligned} H_{\delta\mu} &= \sum_{p_n p_m} \frac{2}{L} \int \sin(p_n x)\delta\mu(x)\sin(p_m x) c^\dagger_{p_n} c_{p_m} \,\mathrm{d}x, \\ &= \vec{c}^{\,\dagger}(\tau_z \otimes \mathscr{H}_{\delta\mu})\vec{c}. \end{aligned} \tag{4.35}$$

We calculate the matrix elements of $\mathscr{H}_{\delta\mu}$:

$$\begin{aligned} (\mathscr{H}_{\delta\mu})_{nm} &= \frac{2}{L}\int \sin(p_n x)\delta\mu(x)\sin(p_m x)\,\mathrm{d}x, \\ &= \sum_{j=0}^{N_{\delta\mu}-1} \frac{2}{L}\int_0^L \sin(p_n x)\mathrm{rect}\left(\frac{x - a\left(j+\frac{1}{2}\right)}{a}\right)\delta\mu_{j+1}\sin(p_m x)\,\mathrm{d}x. \end{aligned} \tag{4.36}$$

Due the the rectangular functions, the integrand is only different from zero on the intervals $x \in [x_j, x_{j+1}]$, where $x_j = aj$. This changes the limits on the integral, which we then perform:

$$\begin{aligned} &= \sum_{j=0}^{N_{\delta\mu}-1} \frac{2\delta\mu_{j+1}}{L}\int_{x_j}^{x_{j+1}} \sin(p_n x)\sin(p_m x)\,\mathrm{d}x \\ &= \sum_{j=0}^{N_{\delta\mu}-1} \frac{\delta\mu_{j+1}}{\pi(m^2-n^2)}\left[(m+n)\left[\sin\left(\frac{m-n}{N_{\delta\mu}}\pi(j+1)\right) - \sin\left(\frac{m-n}{N_{\delta\mu}}\pi j\right)\right]\right. \\ &\qquad \left. -(m-n)\left[\sin\left(\frac{m+n}{N_{\delta\mu}}\pi(j+1)\right) - \sin\left(\frac{m+n}{N_{\delta\mu}}\pi j\right)\right]\right]. \end{aligned} \tag{4.37}$$

In the case of $n = m$, we have to be careful because of the term $(m^2 - n^2)$ in the denominator. Taking the limit $m \to n$ we see that it is well defined and obtain

$$(\mathscr{H}_{\delta\mu})_{nn} = \sum_{j=0}^{N_{\delta\mu}-1} \frac{\delta\mu_{j+1}}{N_{\delta\mu}} - \frac{\delta\mu_{j+1}}{2\pi n}\left[\sin\left(\frac{2n\pi(j+1)}{N_{\delta\mu}}\right) - \sin\left(\frac{2n\pi j}{N_{\delta\mu}}\right)\right]. \tag{4.38}$$

The terms $\sum_{j=0}^{N_{\delta\mu}-1} \frac{\delta\mu_{j+1}}{N_{\delta\mu}}$ are just the average of the disorder potential which is zero from the definition of the disorder potential. The remaining terms in eq. (4.37) can be rewritten on a more compact form by relabelling the indices:

$$\begin{aligned} &\sum_{j=0}^{N_{\delta\mu}-1} \delta\mu_{j+1}\left[\sin\left(\frac{m\pm n}{N_{\delta\mu}}\pi(j+1)\right) - \sin\left(\frac{m\pm n}{N_{\delta\mu}}\pi j\right)\right] \\ &= \sum_{j=1}^{N_{\delta\mu}-1}\left[(\delta\mu_j - \delta\mu_{j+1})\sin\left(\frac{m\pm n}{N_{\delta\mu}}\pi j\right)\right] + \delta\mu_{N_{\delta\mu}}\sin\left(\frac{m\pm n}{N_{\delta\mu}}\pi(N_{\delta\mu}-1+1)\right) \\ &\qquad - \delta\mu_1\sin\left(\frac{m\pm n}{N_{\delta\mu}}\pi\times 0\right) \\ &= \sum_{j=1}^{N_{\delta\mu}-1}(\delta\mu_j - \delta\mu_{j+1})\sin\left(\frac{m\pm n}{N_{\delta\mu}}\pi j\right), \end{aligned} \tag{4.39}$$

where the two last terms in the second line are zero, since $m \pm n$ is an integer. The expression for the elements of $\mathscr{H}_{\delta\mu}$ then becomes

$$(\mathscr{H}_{\delta\mu})_{nm} = \sum_{j=1}^{N_{\delta\mu}-1} \frac{\delta\mu_j - \delta\mu_{j+1}}{\pi(m^2-n^2)} \left[(m+n)\sin\left(\frac{m-n}{N_{\delta\mu}}\pi j\right) - (m-n)\sin\left(\frac{m+n}{N_{\delta\mu}}\pi j\right)\right] \tag{4.40}$$

$$(\mathscr{H}_{\delta\mu})_{nn} = -\sum_{j=1}^{N_{\delta\mu}-1} \frac{\delta\mu_j - \delta\mu_{j+1}}{2\pi n}\sin\left(\frac{2n\pi j}{N_{\delta\mu}}\right). \tag{4.41}$$

The sum is recognized as a discrete sine transform which enables us to use the fast sine transform algorithm in numerical computations to optimize the runtime.

The disordered pairing potential $\Delta(x)$ given in eq. (4.10) is included the same way. Now that $\Delta(x)$ depends on x we have to redo the calculation of $\mathscr{H}_\Delta$ in the basis of eigenmodes. The calculations are quite similar to the case of the disorder potential $\delta\mu(x)$ but require some more algebra:

$$\begin{aligned}(\mathscr{H}_\Delta)_{nm} &= \frac{1}{L}\int_0^L \Delta(x)\left(\sin(p_n x)\partial_x \sin(p_m x) - (\partial_x \sin(p_n x))\sin(p_m x)\right)\,\mathrm{d}x \\ &= \frac{1}{L}\int_0^L \sum_{j=0}^{N_\Delta-1} \mathrm{rect}\left(\frac{x - a\left(j+\frac{1}{2}\right)}{a}\right)\Delta_{j+1}\left[\sin(p_n x)p_m \sin(p_m x) - p_n \sin(p_n x)\sin(p_m x)\right]\,\mathrm{d}x \end{aligned} \tag{4.42}$$

We change the limits on the integral due to the rectangular function, perform the integral, and collect similar terms:

$$\begin{aligned}
&= \sum_{j=0}^{N_\Delta-1} \frac{\pi\Delta_{j+1}}{L^2}\int_{x_j}^{x_{j+1}} \left(m\sin(\tfrac{n\pi}{L}x)\sin(\tfrac{m\pi}{L}x) - n\sin(\tfrac{n\pi}{L}x)\sin(\tfrac{m\pi}{L}x)\right)\,\mathrm{d}x \\
&= \sum_{j=0}^{N_\Delta-1} \frac{m\Delta_{j+1}}{2L(m^2-n^2)}\left[(m+n)\left[\cos\left(\frac{(m-n)}{N_\Delta}\pi(j+1)\right) - \cos\left(\frac{(m-n)}{N_\Delta}\pi j\right)\right]\right. \\
&\qquad \left. -(m-n)\left[\cos\left(\frac{(m+n)}{N_\Delta}\pi(j+1)\right) - \cos\left(\frac{(m+n)}{N_\Delta}\pi j\right)\right]\right] \\
&\quad + \frac{n\Delta_{j+1}}{2L(m^2-n^2)}\left[(m+n)\left[\cos\left(\frac{(m-n)}{N_\Delta}\pi(j+1)\right) - \cos\left(\frac{(m-n)}{N_\Delta}\pi j\right)\right]\right. \\
&\qquad \left. +(m-n)\left[\cos\left(\frac{(m+n)}{N_\Delta}\pi(j+1)\right) - \cos\left(\frac{(m+n)}{N_\Delta}\pi j\right)\right]\right] \\
&= \sum_{j=0}^{N_\Delta-1} \frac{\Delta_{j+1}}{2L(m^2-n^2)}\left[(m+n)^2\left[\cos\left(\frac{(m-n)}{N_\Delta}\pi(j+1)\right) - \cos\left(\frac{(m-n)}{N_\Delta}\pi j\right)\right]\right. \\
&\qquad \left. -(m-n)^2\left[\cos\left(\frac{(m+n)}{N_\Delta}\pi(j+1)\right) - \cos\left(\frac{(m+n)}{N_\Delta}\pi j\right)\right]\right].
\end{aligned} \tag{4.43}$$

We rewrite this expression using the addition theorem for cosines. Let $b = \frac{m\pm n}{N_\Delta}\pi$ and consider the two equations

$$\cos(b((j+1)-\tfrac{1}{2})) = \cos(b(j+1))\cos(b\tfrac{1}{2}) + \sin(b(j+1))\sin(b\tfrac{1}{2}) \tag{4.44}$$
$$\cos(b(j+\tfrac{1}{2})) = \cos(bj)\cos(b\tfrac{1}{2}) - \sin(bj)\sin(b\tfrac{1}{2}). \tag{4.45}$$

We solve eq. (4.44) for $\cos(b(j+1))$ and eq. (4.45) for $\cos(bj)$ and obtain the equations

$$\cos(b(j+1)) = \frac{\cos(b(j+\frac{1}{2})) - \sin(b(j+1))\sin(b\frac{1}{2})}{\cos(b\frac{1}{2})} \tag{4.46}$$
$$\cos(bj) = \frac{\cos(b(j+\frac{1}{2})) + \sin(bj)\sin(b\frac{1}{2})}{\cos(b\frac{1}{2})}. \tag{4.47}$$

Upon subtracting eq. (4.47) from eq. (4.46) we obtain the equation

$$\cos(b(j+1)) - \cos(bj) = -\tan(b\tfrac{1}{2})(\sin(b(j+1)) - \sin(bj)) \tag{4.48}$$

which we see is of the same form as the cosine terms in eq. (4.43) so we make the substitution. It is then seen that the sum takes the same form as in eq. eq. (4.37) and eq. (4.38) and we perform the same trick of relabelling the indices as in eq. (4.39):

$$\begin{aligned}(\mathscr{H}_\Delta)_{nm} = \sum_{j=0}^{N_\Delta-1} \frac{\Delta_{j+1}}{2L(m^2-n^2)} \Bigg[&(m-n)^2\tan\left(\frac{m+n}{2N_\Delta}\pi\right)\left[\sin\left(\frac{(m+n)}{N_\Delta}\pi(j+1)\right)\right.\\ &\left.-\sin\left(\frac{(m+n)}{N_\Delta}\pi j\right)\right]\\ &-(m+n)^2\tan\left(\frac{m-n}{2N_\Delta}\pi\right)\left[\sin\left(\frac{(m-n)}{N_\Delta}\pi(j+1)\right)\right.\\ &\left.-\sin\left(\frac{(m-n)}{N_\Delta}\pi j\right)\right]\Bigg]\end{aligned}$$

$$\begin{aligned}&= \frac{1}{2L(m^2-n^2)}\Bigg[(m-n)^2\tan\left(\frac{m+n}{2N_\Delta}\pi\right)\sum_{j=1}^{N_\Delta-1}(\Delta_j-\Delta_{j+1})\sin\left(\frac{(m+n)}{N_\Delta}\pi j\right)\\ &-(m+n)^2\tan\left(\frac{m-n}{2N_\Delta}\pi\right)\sum_{j=1}^{N_\Delta-1}(\Delta_j-\Delta_{j+1})\sin\left(\frac{(m-n)}{N_\Delta}\pi j\right)\Bigg].\end{aligned} \tag{4.49}$$

The two sums are recognized to have the form of a discrete sine transform, and we can again use the fast sine transform algorithm in numerical computations.

Examples of the spacial distribution of the wave function of the Majorana bound state and the first bulk state can be seen for different disorder strengths in figures 4.2 (chemical potential disorder) and 4.3 (pairing potential disorder) and we make the same observations as in the case of the tight binding model.

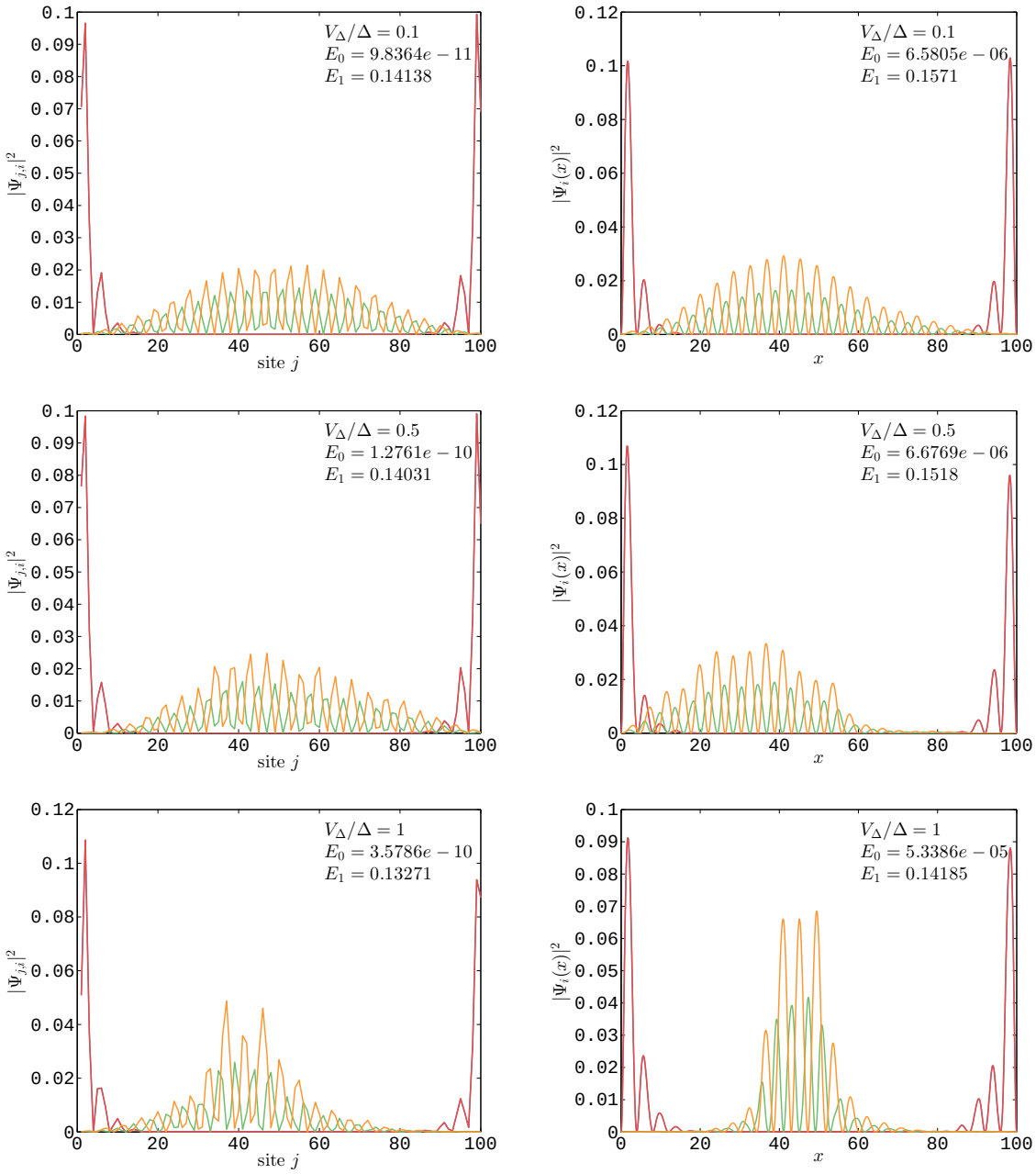

Figure 4.3: Absolute squared values of eigenvectors for eigenvalues Majorana bound state (red) and first bulk state (green and yellow) obtained from the tight-binding model (left) and eigenmode model (right) for a single disorder configuration and for three different disorder amplitudes V_Δ. Each eigenvector consist of an electron part and a hole part, which are plotted independently. There is only one curve for the Majorana as the electron and hole parts of its eigenvector are distributed equally. The energy eigenvalues of the Majorana E_0 and first bulk state E_1 for each disorder configuration is written in the plots. Other parameters are $m = 1$, $L = 100$, $a = 1$, $\Delta = 0.2$ and $\mu = 0.3$.

4.2 Majorana end state energy shift in wire with disorder

Now that we have introduced the disordered chemical potential in our two models we will check if the numerical results in agreement with predictions from the literature. According to Brouwer *et.al.* [23], the dependence of the Majorana bound state energy on wire length is changed by disorder. They found that in the limit $\mu \gg \frac{m}{2}\Delta^2$, the expectation value of the energy in a disordered wire has the following dependence in the wire length

$$\left\langle \ln \frac{E_0}{2\Delta} \right\rangle = -L\left(\frac{1}{\xi} - \frac{1}{2l}\right), \tag{4.50}$$

where ξ is the coherence length and l is the mean free path in the continuous limit $a \to 0$, which we have calculated in section 4.1.3:

$$\xi = \frac{1}{\Delta m}, \qquad l = \frac{v_F^2}{2\gamma}, \qquad v_F = \sqrt{\frac{2\mu}{m}}, \tag{4.51}$$

where $\gamma = V_\mu^2 a$ is the disorder strength.

In figure 4.4 we see that the numerical results obtained with the tight-binding model agree with the prediction in eq. (4.50). The size of the computational matrix scales linearly with the length of the wire and since we cannot use sparse routines in the eigenmode model, we have not been able to obtain numerical results from this model due to the large memory requirement. In hindsight, it would have been wiser to implement chemical potential disorder in the eigenmode model such that the disordered chemical potential is diagonal in the eigenmode basis. In that case, the matrices in the eigenmode model would consist mostly of zeros and sparse routines could be efficiently used to minimize memory requirements. The important property of the disorder potential is that it becomes white noise correlated in the limit of infinite matrix size:

$$\lim_{N_{\delta\mu}\to\infty} \langle \delta\mu(x)\delta\mu(x')\rangle = \gamma_\mu \delta(x - x'). \tag{4.52}$$

A possible model for such a disorder potential might be of the form

$$\delta(x) \propto \sum_{n=1}^{N_{\delta\mu}} \delta\mu_n \sin^2(p_n x), \tag{4.53}$$

where the $\delta\mu_n$'s are random variables of some probability distribution.

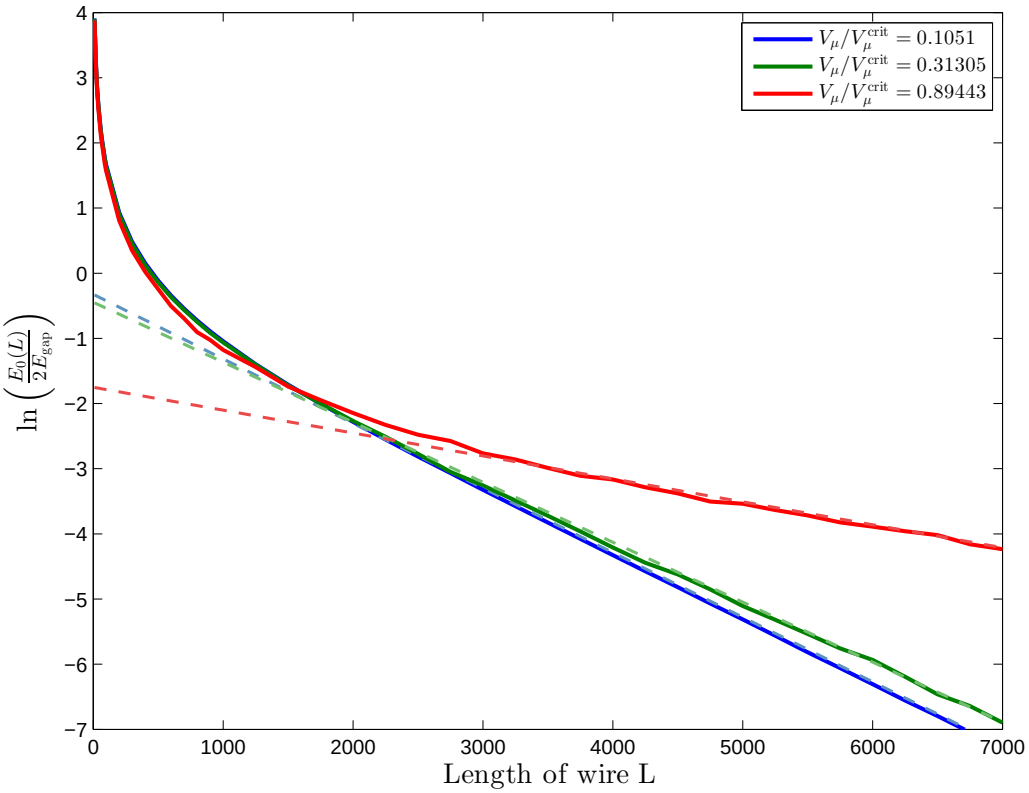

Figure 4.4: The Majorana end state energy E_0 as a function of wire length for different disorder amplitudes V_μ normalized by the critical disorder amplitude given in eq. (4.55). Numerical data are full lines while theoretical predictions from eq. (4.50) are dashed lines. Other parameters are $\Delta = 10^{-3}$, $a = 1$, $\mu = 1$, $m = 1$, sample size 10^3.

4.3 Majorana delocalization and the gap closing

As we have shown analytically (cf. section 2.3 and 3.2) and numerically (cf. section 4.1.4 and 4.1.5) that the Majorana bound states are localised at the ends of the wire. We will now examine how disorder changes the spacial distribution of the wave functions. The spacial extension of the wave function of state the eigenstate $|\psi_j\rangle$ can be quantified by a localization length ζ_j. This can be defined in terms of the inverse participation number, which in turn is defined as the second moment of the absolute square of the wave function (p. 1497 in [24])

$$\zeta_j^{-1} = \int_0^L |\Psi_j(x)|^4 \, \mathrm{d}x. \tag{4.54}$$

In the tight binding model, this integral is substituted by a sum over the entries in the eigenvectors, while the eigenvectors obtained in the eigenmode model must first be represented in real space to get the wave function. To get a sense of what the localization length means, we consider two cases:

- A completely uniform wave function distributed over the entire length of the wire L

with the value $1/\sqrt{L}$, which is required for the wave function to be normalized. The localization length is in this case L.

- A wave function which takes the value $1/\lambda$ on the interval λ and is zero elsewhere. This state is also normalized, but has the localization length λ. When $\lambda = L$ the two cases are the same.

Due to the superconductivity, the eigenstates of the Hamiltonian will be superpositions of particle and hole excitations and ζ_j is a measure of the localization of these quasi-particles. We see in figure 4.2 and 4.3 how the first bulk state becomes localized with increasing disorder. In the clean wire, the wave function is spread over the entire wire in the form of a sine wave, while in a disordered wire, the wave function becomes localised in a smaller part of the wire.

In the clean wire case, the Majorana end state has the localization length $\xi = \frac{1}{\Delta m}$. As long as the localization length of the Majorana bound state is much smaller than the mean free path, the Majoranas are effectively unaffected by the disorder. As disorder is increased, the mean free path becomes smaller and the effect on the Majoranas larger. At some point the disorder will destroy the zero energy states. From eq. (4.50) we see that the energy of the Majoranas decreases with wire length for $2l > \xi$ while it increases for $2l < \xi$. According to Brouwer *et.al.* [23] $2l = \xi$ is the point where disorder destroys the zero energy Majorana. Using eq. (4.51) we find the critical disorder strength

$$\gamma^{\text{crit}} = \frac{2\mu\Delta}{m} \Rightarrow V_\mu^{\text{crit}} = \sqrt{\frac{2\mu\Delta}{ma}}. \tag{4.55}$$

In figure 4.5 we see how the energies and localization lengths of the Majorana end state and the first bulk state change as a function of disorder strength for the tight binding model as well as for the eigenmode model. The tight binding model agrees with the prediction of disorder destroying the zero energy mode when $2l = \xi$, while the energy gap closes at twice the critical disorder strength for the eigenmode model. Both models show that the first bulk state becomes localized as disorder increases and the energy gap closes, while the Majorana end state becomes a delocalized state with non-zero energy.

In figure 4.6 have plotted the energy of the Majorana bound state and the first bulk state for increasing pairing potential disorder. As in the case of chemical potential disorder, the energy gap between the Majorana bound state and the bulk states closes for increasing disorder strength. On the contrary, the Majorana energy does not change much from zero even when the energy gap closes. In the results from the tight-binding model, the spread of Majorana energies seems to oscillate as a function of disorder strength.

In order to focus on the effects of disordered chemical potential, we have not investigated the effects of a disordered pairing potential any further.

We have now tested our numerical models both with and without disorder and the results agree with theoretical predictions, and we are assured of the validity of the models. We are then ready to proceed with the main task of this thesis: Attempting to find a correspondence between the p-wave Hamiltonian and a random matrix model.

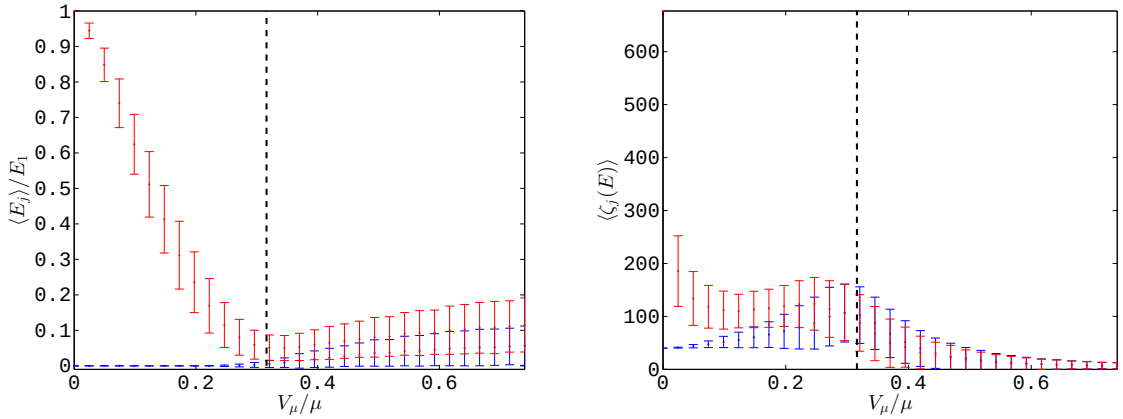

(a) Tight binding model. Parameters are: Wire length $L = 500$, computational matrix size $N = 500$, pariring potential $\Delta = 0.02$, chemical potential $\mu = 1$ and sample size 2×10^3.

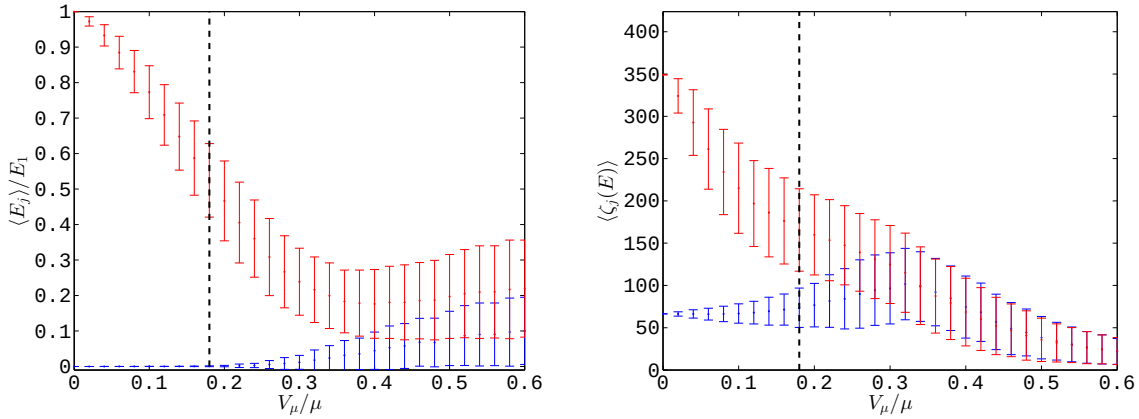

(b) Eigenmode model. Parameters are: Wire length $L = 500$, computational matrix size $N = 500$, pariring potential $\Delta = 0.05$, chemical potential $\mu = 1.23$ and sample size 2×10^3.

Figure 4.5: Energy and localization length of the Majorana bound state (blue) and first bulk state (red) as function of disorder strength. The energy eigenvalues are normalized by the first bulk state in the non-disordered case and error bars are the one standard deviation interval. The critical disorder strength V_μ^{crit}/μ found by eq. (4.55) is indicated with a horizontal dashed black line.

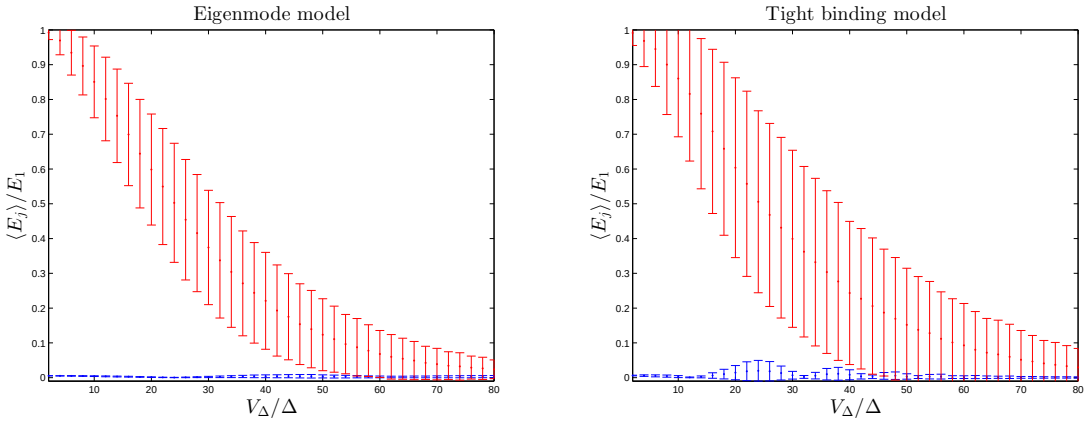

Figure 4.6: Energy of the Majorana and state (blue) and first bulk state (red) as function of disorder strength γ_Δ/Δ. The energy eigenvalues are normalized by the first bulk state in the non-disordered case and error bars are the one standard deviation interval.

Chapter 5

Random Matrix Theory

Random matrix theory (RMT) is, as the name suggest, the study of random matrices and has proven to have widespread applications, ranging from quantum chromo dynamics, to describing the distribution of values of the Riemann zeta function on the critical line, and the distribution of energy levels in heavy atom nuclei, to name a few [18]. The motivation for using RMT to study certain quantum systems is that when the specific form of the Hamiltonian is too complicated to solve or the Hamiltonian is unknown, a RMT with the same symmetries might contain detailed information about the statistical properties of the original system.

The elements of a random matrix are random variables of a given probability distribution only constrained by the symmetry properties of the matrix. The eigenvalues of such matrices can be obtained by numerical diagonalization. When this is done for a large sample of random matrices, the eigenvalues close to zero are distributed in a way that is unique to the set of symmetry constraints of the matrix but to a large extent independent of the probability distribution. For some random matrix ensembles it is possible to obtain analytical results on the statistical properties of these eigenvalues and eigenvectors. Examples of such statistical properties are: The distribution function of all eigenvalues of a random matrix called the average spectral density (ASD) in the limit of the matrix size going to infinity[25] and the probability distribution functions of the individual eigenvalues[26]. In the case of matrices of size $2N \times 2N$, the universality applies only to the first $\approx\sqrt{N}$ eigenvalues closest to zero, but if we are interested in the first few eigenvalues only, it is possible to obtain accurate results by numerical simulations of relatively small matrices.

It is due to the prospect of finding an analytical description of the Majorana end state energy distribution in a disordered quantum wire that we try to establish a correspondence to RMT. Finding a corresponding RMT might prove a useful tool in order to determine whether the experimentally observed zero bias peak is a signature of a Majorana fermion or if it is caused by some other mechanism. We will try to locate an eventual correspondence by searching for a consensus of the ASD of the p-wave Hamiltonian for different parameters and of different random matrix ensembles.

To the extend of our knowledge, no direct correspondence between the average spectrum density of our model of a 1D disordered p-wave superconductor and a RMT has been established yet, and no theoretical predictions have been made of where such a correspondence might be found if it exists. Due to the lack of firm theoretical predictions, we will proceed as follows: We describe the 10 universal symmetry classes and determine which one of them the p-wave Hamiltonian belongs to. We then examine the random matrix ensembles from the same symmetry class. The ASD of the p-wave Hamiltonian is computed for a wide range parameters

in the search of a parameter domain where the features of the ASD are similar to those seen in RMT and it therefore might be possible to design an equivalent random matrix model. When this domain is located, we attempt to design a random matrix model which matches the ASD of the first few energy eigenvalues of the p-wave Hamiltonian closest to zero.

In the previous chapter we considered two types of disorder: chemical potential disorder and pairing potential disorder. In this chapter we will restrict ourselves to chemical potential disorder due to the limited time available. We performed a superficial investigation of pairing potential disorder but did not find any parameter domain where a correspondence to RMT seemed plausible and afterwards focused on chemical potential disorder.

5.1 Universal symmetry classes

In this section we make a short introduction of the 10 Altland-Zirnbauer universal symmetry classes[6, 7] in order to classify the 1D p-wave Hamiltonian.

Non-interacting electron systems can be put into a classification scheme according to the discrete symmetries of the Hamiltonian. The same classification scheme is used in random matrix theory (with a slightly different terminology) to label random matrix ensembles with different symmetry constraints. The interest in the classification of Hamiltonians is due to the existence of certain topological properties which to a large extent does not depend on the explicit form of the Hamiltonian but only its symmetries.

A system of non-interacting fermions is described by a second quantized Hamiltonian

$$H = \sum_{AB} \psi_A^\dagger H_{A,B} \psi_B, \tag{5.1}$$

where $\psi_A^\dagger$ and ψ_B are fermionic creation and annihilation operators satisfying the usual anti-commutations relations. The subscripts A and B can be a set of indices, such as spins, lattice or continuous coordinates, or momenta. In Nambu formalism the sum can be written as a matrix product

$$H = \vec{\psi}^\dagger \mathscr{H} \vec{\psi}, \tag{5.2}$$

where $H_{A,B}$ are the matrix elements of $\mathscr{H}$, which is called the single particle Hamiltonian (SPH). A general classification of Hamiltonians is discussed in [27], where H is said to posses a certain symmetry if the SPH $\mathscr{H}$ can be related to $-\mathscr{H}$, its transpose $\mathscr{H}^T$, and/or its complex conjugate $\mathscr{H}^*$ by a unitary transformation and this transformation squares to one. We consider the following transformations

- P-symmetry: $P\mathscr{H}P^{-1} = -\mathscr{H}$ where $PP^\dagger = P^2 = 1$.
- C-symmetry: $C\mathscr{H}C^{-1} = \epsilon_c \mathscr{H}^T$ where $CC^\dagger = 1$ and $C^T = \eta_c C$ ($\epsilon_c = \pm 1$ and $\eta_c = \pm 1$).
- K-symmetry: $K\mathscr{H}K^{-1} = \epsilon_k \mathscr{H}^*$ where $KK^\dagger = 1$ and $K^T = \eta_k K$ ($\epsilon_k = \pm 1$ and $\eta_k = \pm 1$).

The P-type symmetry is referred to as chiral symmetry, while C is particle-hole symmetry and K is time reversal symmetry. However, when we are dealing with hermitian Hamiltonians, which are the only ones we consider, $\mathscr{H} = \mathscr{H}^\dagger = (\mathscr{H}^*)^T \Rightarrow \mathscr{H}^T = \mathscr{H}^*$. C and K are therefore identical and we will only consider C. When $\epsilon_c = +1$ we will denote C as a time reversal symmetry and when $\epsilon_c = -1$ as a particle-hole symmetry.

Non-interacting fermionic systems are described by a Hamiltonian out of the 10 possible symmetry classes introduced by Altland and Zirnbauer in [6] and [7]. They find the 10 symmetry classes listed in table (5.1).

Symmetry classes	Discrete symmetry relation
A	$H = H^\dagger$
AI	$\epsilon_c = +1\,;\, \eta_c = +1$
AII	$\epsilon_c = +1\,;\, \eta_c = -1$
C	$\epsilon_c = -1\,;\, \eta_c = -1$
D	$\epsilon_c = -1\,;\, \eta_c = +1$
AIII	$P^2 = 1$
BDI	$P^2 = 1\,;\, \epsilon_c = \pm 1\,;\, \eta_c = +1\,;\, PCP^T = C$
CII	$P^2 = 1\,;\, \epsilon_c = \pm 1\,;\, \eta_c = -1\,;\, PCP^T = C$
CI	$P^2 = 1\,;\, \epsilon_c = \pm 1\,;\, \eta_c = \pm 1\,;\, PCP^T = -C$
DIII	$P^2 = 1\,;\, \epsilon_c = \mp 1\,;\, \eta_c = \pm 1\,;\, PCP^T = -C$

Table 5.1: The 10 symmetry classes classified according to the scheme in [27].

An alternative and perhaps more intuitive classification scheme is given in [8], where Hamiltonians are classified according to three symmetry operations: Time reversal symmetry (TRS) Θ, particle-hole symmetry (PHS) Υ and sublattice (or chiral) symmetry (SLS).

The TRS can be represented by an anti-unitary operator, which in general can be written as a product of an unitary operator U and the complex conjugation operator K, $\Theta = UK$,

$$\Theta \mathscr{H} \Theta^{-1} = \mathscr{H}. \tag{5.3}$$

In other words, the system is time reversal invariant if the Hamiltonian is equal to its complex conjugate up to an unitary operator:

$$\Theta \,:\, U^\dagger \mathscr{H}^* U = +\mathscr{H}. \tag{5.4}$$

If the system does not have TRS, we denote it by [TRS] = 0 and if it has TRS, it is denoted by the square of the time reversal operator, $\Theta^2 = \pm 1$. For spinless systems or for integer spin we usually have $\Theta^2 = +1$, which we denote [TRS] = +1. For half-integer spin system we usually have $\Theta^2 = -1$ and we denote this by [TRS] = −1, which in total gives three possibilities.

PHS can also be represented by an anti-unitary operator written as a product of an unitary operator V and the complex conjugation operator K, $\Upsilon = VK$,

$$\Upsilon \mathscr{H} \Upsilon^{-1} = -\mathscr{H}, \tag{5.5}$$

or

$$\Upsilon \,:\, V^\dagger \mathscr{H}^* V = -\mathscr{H}. \tag{5.6}$$

As for TRS, PHS can either be pressent or absent, and if present, the square of the particle-hole operator can be ± 1, and this is denoted in the same way, $[\mathrm{PHS}] = \{-1, 0, +1\}$.

The last symmetry to be introduced is the sublattice or chiral symmetry (SLS). SLS is the product of TRS and PHS, SLS = TRS × PHS. So SLS is already given by TRS and PHS in all but one case. When $[\mathrm{TRS}, \mathrm{PHS}] = [0, 0]$, SLS can be either present [SLS] = 1 or absent [SLS] = 0. This gives in total 10 symmetry classes listed according to this classification scheme in table (5.2), along with the group of their associated topological invariant in one to three dimensions.

		TRS	PHS	SLS	$d=1$	2	3
Standard	A (unitary)	0	0	0	$-$	$\mathbb{Z}$	$-$
	AI (orthogonal)	$+1$	0	0	$-$	$-$	$-$
	AII (symplectic)	-1	0	0	$-$	$\mathbb{Z}_2$	$\mathbb{Z}_2$
Chiral	AIII (unitary)	0	0	1	$\mathbb{Z}$	$-$	$\mathbb{Z}$
	BDI (orthogonal)	$+1$	$+1$	1	$\mathbb{Z}$	$-$	$-$
	CII (symplectic)	-1	-1	1	$\mathbb{Z}$	$-$	$\mathbb{Z}_2$
BdG	D	0	-1	0	$\mathbb{Z}_2$	$\mathbb{Z}$	$-$
	C	0	-1	0	$-$	$\mathbb{Z}$	$-$
	DIII	-1	$+1$	1	$\mathbb{Z}_2$	$\mathbb{Z}_2$	$\mathbb{Z}$
	CI	$+1$	-1	1	$-$	$-$	$\mathbb{Z}$

Table 5.2: The 10 symmetry classes of single particle Hamiltonians classified according to the scheme in [8]. If a topologically non-trivial ground state exist, it is characterized by a topological invariant which belong to either the integers $\mathbb{Z}$ or the group $\mathbb{Z}_2$ consisting of $(0, 1)$ or $(-1, +1)$.

5.1.1 Symmetry classes and their physical realizations

We will now go through a brief description of the ten symmetry classes and examples of physical systems for each class, if any exists.

Standard (Wigner-Dyson) classes

These where the first three symmetry classes considered by Wigner and Dyson[18], to whom they owe their name.

- Class A: The case where the Hamiltonian possesses neither TRS or PHS, it belongs to class A called unitary. Example: The quantum Hall effect observed in a 2D electron gas in a magnetic field.
- Class AI: When $\Theta^2 = +1$ the Hamiltonian belongs to the orthogonal symmetry class and the system can be realized by considering spinless particles or particles of integer spin.
- Class AII: Hamiltonians with $\Theta^2 = -1$ belong to the symplectic symmetry class and may describe spin-half particles with spin-orbit coupling.

Chiral classes

It is conventional to denote a P-type or SLS symmetry as chiral symmetry and the class of Hamiltonians with this symmetry are denoted chiral symmetry classes.

- Class AIII: With chiral symmetry only, this class is simply called chiral unitary class. This may be realized as a disordered tight binding model on a bipartite lattice with broken TRS.
- Class CII: Hamiltonians of this class have TRS and $\Theta^2 = -1$ and the class is called chiral symplectic.

- Class BDI: Hamiltonians of this class have TRS and $\Theta^2 = +1$ and the class is called chiral orthogonal.

Bogoliubov-de Gennes classes

This class consists of Hamiltonians which involve superconductors and it is custom to write it on Bogoliubov-de Gennes-form in terms of Nambu spinors

$$H = \frac{1}{2}(c^\dagger, c) \begin{bmatrix} h & \Delta \\ -\Delta^* & -h^T \end{bmatrix} \begin{pmatrix} c \\ c^\dagger \end{pmatrix}, \tag{5.7}$$

where $h^\dagger = h$ is required by the hermiticity of the Hamiltonian $H^\dagger = H$ and $\Delta^T = -\Delta$ from Fermi statistics. $c^{(\dagger)}$ is the annihilation (creation) operator of either spinless fermions or spin-half electrons $c = (c_\uparrow, c_\downarrow)$. In the examples τ_α, σ_α and r_α will be Pauli matrices.

- Class D: The $(p \pm ip)$-wave pairing superconductor has the symmetry $\tau_x H^T \tau_x = -H$, where

$$H = \frac{1}{2}\sum_k (c_k^\dagger, c_{-k}) \begin{bmatrix} \epsilon_k - \mu & \Delta_0(k_x \pm ik_y) \\ \Delta_0(k_x \mp ik_y) & -\epsilon_k + \mu \end{bmatrix} \begin{pmatrix} c_k \\ c_{-k}^\dagger \end{pmatrix}. \tag{5.8}$$

- Class DIII: A Hamiltonian with $\tau_x H^T \tau_x = -H$ and $i\sigma_y H^T (-i\sigma_y) = H$ can be realized by a superposition of a $(p + ip)$ and a $(p - ip)$-wave pairing superconductor.

- Class C: The $(d \pm id)$-wave pairing superconductor is an example with $r_y H r_y = -H^T$.

- Class CI: A Hamiltonian with $d_{x^2-y^2}$ or d_{xy}-wave pairing has the symmetry $H^* = H$.

5.2 Symmetries of the one-dimensional p-wave superconductor Hamiltonian

In order to construct a relevant random matrix model, we must know which universal symmetry class it should belong to. We will therefore determine the symmetries of the Hamiltonian for the one-dimensional p-wave superconductor. Recalling the p-wave Hamiltonian

$$H = \sum_p \frac{1}{2} \vec{c}_p^\dagger \mathscr{H} \vec{c}_p \tag{5.9}$$

$$\mathscr{H} = \begin{bmatrix} \xi_p & p\Delta \\ p\Delta^* & -\xi_p \end{bmatrix} \tag{5.10}$$

where $\xi_p = \frac{p^2}{2m} - \mu$, Δ is the superconducting pairing potential, μ is the chemical potential and m is the mass of the fermions. In our present case the Hamiltonian is spinless and the particle-hole and time reversal operators are usually defined as

$$\Upsilon = \tau_x \mathcal{K}, \qquad \text{and} \qquad \Theta = \mathcal{K}, \tag{5.11}$$

where $\mathcal{K}$ is the complex conjugation operator and Θ and Υ satisfy $\Theta^2 = \Upsilon^2 = 1$. The complex conjugation operator reverts the sign on the momentum operator as it is defined

as $p = -ihbar\partial$. We see that the single particle Hamiltonian $\mathscr{H}$ is anti-symmetric under particle-hole transformation, but not symmetric under time reversal:

$$\Upsilon \mathscr{H} \Upsilon^\dagger = -\mathscr{H}, \tag{5.12}$$

$$\Theta \mathscr{H} \Theta^\dagger \neq \mathscr{H}. \tag{5.13}$$

We can however define a pseudo time reversal operator $\Theta' = \tau_z K$ with $\Theta'^2 = 1$ under which $\mathscr{H}$ is invariant.

A Hamiltonian with time reversal symmetry and particle-hole symmetry of this type belongs to the symmetry class BDI according to the description of the symmetry classes in the former section. In the next section, we will investigate this symmetry class more closely, but first we will note that the p-wave Hamiltonian can be brought to the same explicit form as matrices from the BDI symmetry class, which is given in eq. (5.18). This is done through a pair of rotations in particle-hole space. The unitary operators which rotates around the τ_x-axis and the τ_z-axis respectively are

$$\mathcal{S}_x = \tfrac{1}{\sqrt{2}}(\tau_0 - i\tau_x)\ , \qquad \mathcal{S}_z = \tfrac{1}{\sqrt{2}}(\tau_0 + i\tau_z), \tag{5.14}$$

where τ_i are Pauli matrices and τ_0 is the identity matrix. If we rotate the single particle Hamiltonian in (5.10) around the τ_x-axis and then the τ_z-axis it becomes:

$$\mathscr{H} = \begin{bmatrix} \xi_p & p\Delta \\ p\Delta^* & -\xi_p \end{bmatrix} \tag{5.15}$$

$$\downarrow \text{ rotate around } \tau_x\text{-axis}$$

$$\mathscr{H}_x = \mathcal{S}_x \mathscr{H} \mathcal{S}_x^\dagger = \begin{bmatrix} 0 & \xi_p + p\Delta \\ -\xi_p + p\Delta^* & 0 \end{bmatrix} \tag{5.16}$$

$$\downarrow \text{ rotate around } \tau_z\text{-axis}$$

$$\begin{aligned} \mathscr{H}_{xz} = \mathcal{S}_z \mathscr{H}_x \mathcal{S}_z^\dagger &= \begin{bmatrix} 0 & \xi_p + p\Delta \\ \xi_p - p\Delta^* & 0 \end{bmatrix} \\ &= \begin{bmatrix} 0 & \xi_p + \Delta_p \\ \xi_p^\dagger + \Delta_p^\dagger & 0 \end{bmatrix} \\ &= \begin{bmatrix} 0 & W \\ W^\dagger & 0 \end{bmatrix}, \end{aligned} \tag{5.17}$$

where we have defined $\Delta_p = p\Delta$ and used that $\xi_p^\dagger = \xi_p$ and $\Delta_p^\dagger = -\Delta_p$. If Δ_p is chosen to be real we have that $W^\dagger = W^T$. We see that this matrix has the same form as the one in eq. (5.18).

5.3 The BDI symmetry class

We have shown in the previous section that the 1D p-wave superconductor Hamiltonian belongs to the BDI symmetry class. In this section we will take a closer look at the random matrix ensemble belonging to the BDI symmetry class in order to get some intuition about the features of the random matrix ensembles of BDI.

The BDI (called chiral orthogonal) symmetry class is described in [25] and consists of all matrices of the form

$$H = \begin{bmatrix} 0 & W \\ W^\dagger & 0 \end{bmatrix}, \tag{5.18}$$

where W is a rectangular $p \times q$ matrix with real elements given by independent Gaussian distributions

$$\mathrm{d}P(W) \propto \prod_{a,b} \exp\left(-\frac{|W_{ab}|^2}{2v^2}\right) \mathrm{d}W_{ab}. \tag{5.19}$$

The average distance between eigenvalues, called the interlevel distance, near zero is, in the limit of large N,

$$\delta_E = \frac{v\pi}{2\sqrt{N}}, \tag{5.20}$$

with N being $\min(q,p)$[25]. It is customary to choose either $\delta_E = \pi$ or $\delta_E = 1$ and we choose the later.

The matrix H has $2N$ eigenvalues symmetrically distributed around zero (N on each side) and m zero-eigenvalues, where $m = |p-q|$. For an ensemble of matrices of finite size N and matrix elements given by eq. (5.19) the ASD will globally have the form of a semi-circle, as seen in figure 5.1. The shape of the ASD close to zero will be independent of the given probability distribution of the matrix elements as long as $\langle \rho(x \sim 0) \rangle \neq 0$[28, 29]. The entire ASD only becomes universal in the limit of the matrix size $N \to \infty$. The analytical expression for the ASD in the limit of $N \to \infty$ is derived by Ivanov [25] for the random matrix ensembles BDI, m:

$$\begin{aligned} \langle \rho(x) \rangle_{\mathrm{BDI},m} = \frac{\pi}{2} \Big(y \left[J_m^2(y) - J_{m-1}(y) J_{m+1}(y) \right] + J_m(y) R_m(y) \Big) \\ + m\delta(x), \end{aligned} \tag{5.21}$$

where $y = \pi|x|$, J_n is the n'th Bessel function of the first kind and

$$R_n(z) = 1 - \int_0^z J_n(z')\ \mathrm{d}z. \tag{5.22}$$

In the case of finite N, the ASD takes the form of a semicircle and only the $\approx\sqrt{N}$ eigenvalues closest to zero are given by this expression. The numerically computed ASD of a matrix ensemble with $m = 1$ and $N = 20$ is plotted along the analytic function for the ASD in figure 5.1. We see that only the first few eigenvalues follow the analytical curve.

Every matrix from the symmetry class BDI has m zero eigenvalues, represented by the delta-function in eqn. (5.21), while the remaining states, called bulk states, are on average

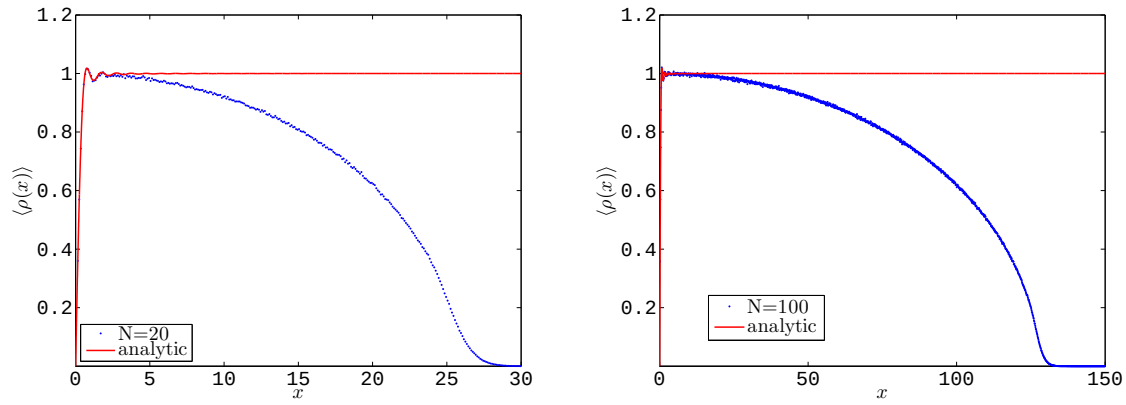

Figure 5.1: Average spectral density for the RMT ensemble BDI, $m = 1$. Numerical results (blue dots) are obtained from data of sample of 10^6 matrices, with $N = 20$ (left) and $N = 100$ (right). The analytic functions (full red line) for $m = 1$ is given i eq. (5.25). Note that there is a eigenvalue from each matrix in the sample located at exactly zero and the analytical function has a delta function at zero.

distributed equidistantly with the interlevel distance given in eq. (5.20). Choosing a different δ_E amounts to a scaling of the ASD, but does not change its form:

$$\langle \rho(x) \rangle \xrightarrow{\delta_E \to \delta'_E} \frac{\delta_E}{\delta'_E} \left\langle \rho\left(\frac{\delta'_E}{\delta_E} x\right) \right\rangle . \tag{5.23}$$

We numerically generate three samples of matrices with $m = 0, 1, 2$ of the form given in eq. (5.18) with elements given by eq. (5.19) and compute the average spectral density. We compare these numerical results with the analytical functions in figure 5.2. We calculate the explicit expression for the ASD for $m = 0, 1, 2$ from eq. (5.21):

$$\langle \rho(x) \rangle_{\mathrm{BDI},m=0} = \frac{\pi}{2} \left(y \left[J_0^2(y) + J_1^2(y) \right] + J_0(y) \left[1 - \frac{y}{2} \left(\pi J_1(y) H_0(y) + J_0(y) \left[2 - \pi H_1(y) \right] \right) \right] \right), \tag{5.24}$$

$$\langle \rho(x) \rangle_{\mathrm{BDI},m=1} = \frac{\pi}{2} \left(y \left[J_1^2(y) - J_0(y) J_2(y) \right] + J_1(y) J_0(y) \right) + \delta(x), \tag{5.25}$$

$$\langle \rho(x) \rangle_{\mathrm{BDI},m=2} = \frac{\pi}{2} \left(y \left[J_2^2(y) - J_1(y) J_3(y) \right] + J_2(y) \left[1 - \tfrac{1}{2} \left(J_1(y) \left[\pi y H_0(y) - 4 \right] + y J_0 \left[2 - \pi H_1(y) \right] \right) \right] \right) + 2\delta(x) \tag{5.26}$$

where H_n is the n'th Struve function [30].

As we see in the figure 5.2, a relative small computational matrix size returns results in good agreement with the analytical curves for the first few eigenvalues.

We denote the matrix ensembles BDI, m as the "principal" ensembles of the BDI symmetry class. It is possible to construct more complex matrix ensembles where the matrix elements are subject to more constraints, while the matrix retains the same symmetries. The average

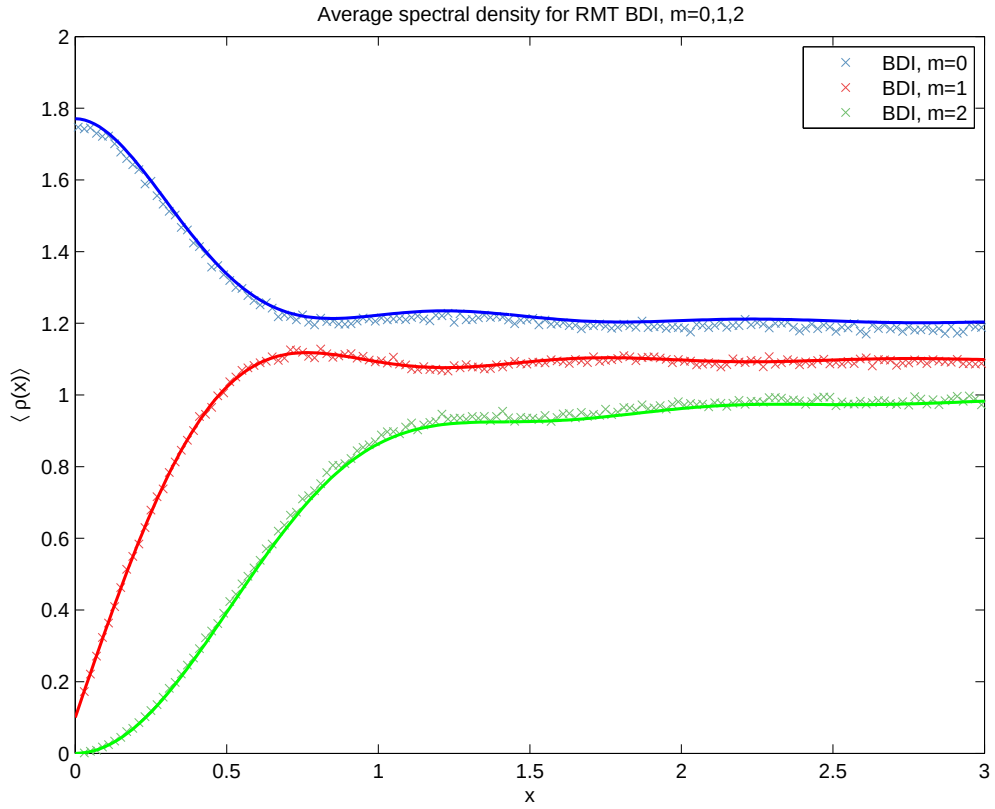

Figure 5.2: Average spectral density for an ensemble of 10^6 matrices of size $p \times q$, with $p = 20$ and $q = p + m$, from the universal symmetry class BDI, $m = 0, 1, 2$ of the form ineq. (5.18). For the curves of BDI, $m = 1$ and $m = 2$, there are delta functions located at $x = 0$ with weight 1 and 2 respectively. Numerical data (crosses) and analytic functions (full line) for $m = 1$ and $m = 0$ has been shifted by $+0.1$ and $+0.2$ on the $\langle \rho(x) \rangle$-axis, to make it easier to distinguish them from each other. The analytical expressions are given i eq. (5.24), (5.25) and (5.26).

spectral density of such a matrix ensemble could be quite different from the "principal" ensembles of BDI described in eq. (5.21). To establish some intuition on how to construct a random matrix ensemble corresponding to the p-wave Hamiltonian with disorder, we will first compare the ASD of the p-wave Hamiltonian with the "principal" ensembles of BDI.

5.4 Comparing with BDI, $m = 1$

We have shown in section 2.3 and 3.4 that the energy of a Majorana end state is only equal to zero in the case of a semi-infinite wire while it is non-zero and exponentially small in the wire length L for a finite wire. Based on this knowledge, one might reason that the BDI, $m = 1$ ensemble could possibly describe the case of the semi-infinite wire since this is a system with only one zero energy state.

It is however not possible to simulate a semi-infinite system with our two models, but if

the overlap between the bound edge state at each end of a finite wire is small, they will be almost zero energy modes and the bulk spectrum should not differ significantly from that of the semi-infinite case. We will in this section test if this assumption holds by comparing the ASD of the p-wave Hamiltonian with the ASD of the BDI, $m = 1$ ensemble. We do not expect to find perfect agreement with this ensemble, but if there are compelling similarities it might serve as a foundation for a more sophisticated random matrix ensemble.

At first, it might seem like wishful thinking to find a direct correspondence between the eigenvalues of simple random matrices from the BDI symmetry class and the energy spectrum of the p-wave Hamiltonian. The average spectral density of the random matrix ensemble from BDI, m is completely determined for each m, and tuning δ_E only amounts to a simple rescaling $f(x) \to \delta_E f(x\delta_E^{-1})$. The energy spectrum of the p-wave superconductor has a whole variety of details, depending on the chosen set of parameters: The size of the gap in the energy spectrum depends on the chemical potential μ and on the pairing potential Δ while the distance between energy levels depends on the length of the wire L, the mass of the fermions m and the pairing potential Δ. When disorder is included, the energy levels are broadened and with increasing disorder strength γ the individual eigenenergy distributions change from non-overlapping to the point where different levels cannot be distinguished from each other any more.

We compute the eigenenergies of the p-wave Hamiltonian by numerical diagonalization of the eigenmode model and tight binding model of a large sample of disorder configurations. The average spectral density (ASD) is obtained by making a histogram of the obtained eigenvalues normalized by the sample size. Examples of average spectral densities for different sets of parameters can be seen in figure 5.3. In the three plots on the left, all parameters except the chemical potential μ is kept constant to illustrate how the energy gap opens up and the lowest energy mode becomes a zero energy mode as we move from the phase transition point at $\mu = 0$ into the topological phase. Increasing Δ linearises the spectrum close to zero, as seen in the plots to the right where the bulk states become equidistant for larger Δ.

Indeed; it is not possible to have a simple random matrix model that is able to match the ASD of the p-wave superconductor for an arbitrary set of parameters. It does however seem plausible that we can find a small domain or point in parameter space where the ASD of the p-wave superconductor is matched by that of a simple random matrix ensemble. In order to locate this domain, we review the features of the ASD of BDI, $m = 1$. Two common features of all of this ensembles is: One that the average level spacing between bulk states is constant (δ_E) and two that there is only a small "gap" for $m > 0$ created by the level repulsion from the zero energy mode, as seen in figure 5.2.

Based on our previous observations of how the energy spectrum of the p-wave Hamiltonian model depends on its parameters, we can deduce the set of parameters where the ASD takes the most "BDI, $m = 1$"-like form. We need to be at a point where there is no gap in the energy spectrum and since we have $\Delta \neq 0$ the energy gap therefore only closes when $\mu = 0$ as we saw in section 2.1. The second feature can be realized for a superconductor where $\Delta \gg \frac{1}{2m}$ and $\mu \approx 0$, as the energy spectrum will be linear close to $E = 0$ which is shown in figure 5.3. The last "ingredient" we need is the disorder to broaden the energy levels, but the appropriate disorder strength cannot be deduced a priori and has to be determined by computing ASDs for different disorder strengths.

Comparing the ASDs in figure 5.2 and 5.3, we see that the energy scales are quite different. However, a simple rescaling of the form

$$\langle \rho(E) \rangle \to \alpha \langle \rho(E\alpha^{-1}) \rangle \tag{5.27}$$

which does not change the shape the ASD and keep the density constant can make the ASD of the p-wave Hamiltonian and BDI, $m = 1$ comparable. If the ASDs are very similar it will be a very likely that a corresponding random matrix model can be constructed.
When we use the term rescaling, it will always mean a rescaling of the form in eq. (5.27) unless specified otherwise. We call α the rescaling factor.

In figure 5.4 we plot the rescaled $\langle\rho(E)\rangle$ for different disorder strength in order to find the appropriate disorder strength. For zero or low disorder strength, the lowest energy mode is a bulk mode with a narrow density distribution at a non-zero value. As disorder is increased the energy of the lowest energy mode goes towards zero energy faster and has a much narrower density distribution than the rest of the bulk modes. For a particular disorder strength $\gamma_\mu = 25600$, there seems to be a qualitative agreement between the ASD of the p-wave superconductor and the BDI $m = 1$ ensemble, seen in the middle right plot. Increasing disorder strength further closes the small "gap" around zero completely and washes out any distinction between energy levels.

Even though the bulk spectrum in the plot with disorder strength $\gamma = 25600$ in figure 5.4 seems to agree qualitatively with the analytical expression of the ASD for BDI, $m = 1$, it is clear that the lowest energy state is an almost-zero energy state, as opposed to the delta function at $E = 0$ in the BDI, $m = 1$ ensemble. If this almost-zero energy mode only deviates slightly from a delta function, it should not have a significant effect on the bulk modes and they should agree with the bulk ASD of BDI, $m = 1$. The weak level repulsion of the BDI ensembles however makes it difficult to distinguish the average level densities (ALD) of distinct bulk levels from one another when they are plotted together as the ASD. Plotting the ALD $\langle\rho_i(E)\rangle$ for each mode separately will make comparison easier.

We expect to find the highest degree of similarity for the ALDs of the lowest bulk modes, but not at higher energy due to the kinetic term in the p-wave Hamiltonian, which will make the average distance between levels larger for higher bulk modes than for the lower modes. We will therefore only compare the ALDs with the first two bulk modes of BDI $m = 1$. We choose the scaling factor α which gives the best fit with the first bulk mode, as we assume that the ALD of the first bulk state has not been deformed by the distorted almost-zero energy mode. The analytic expressions for the first and second bulk eigenvalue are [26]

$$\langle\rho_1(x)\rangle = \frac{\pi}{4} y \exp\left(-\frac{y^2}{8}\right) \tag{5.28}$$

$$\begin{aligned}\langle\rho_2(x)\rangle &= \frac{\pi}{8} y^2 \exp\left(-\frac{y^2}{8}\right) \int_0^1 \frac{z}{\sqrt{1-z^2}} I_3(y\sqrt{1-z^2})\, \mathrm{d}z \\ &= \frac{\pi}{8} \exp\left(-\frac{y^2}{8}\right) (y(1 + I_2(y)) - 2I_1(y))\end{aligned} \tag{5.29}$$

where $y = \pi|x|$ and $I_j(t)$ is the j'th modified Bessel function [30]. The ALDs are plotted with the analytical expressions for the first and second bulk eigenvalue in figure 5.5. The plots are representative for a wide range of parameters, satisfying the ratio in eq. 5.31. There is a large degree of similarity between the numerical results from the eigenmode model and the analytical curves of BDI, $m = 1$, while the ALDs of the tight binding model lie closer to each other than in BDI, $m = 1$. We do not expect complete agreement because the lowest eigenenergy is not an exact delta function distribution at zero energy. Our assumption was however that the almost-zero energy mode not would effect the bulk spectrum significantly

and we would therefore expect that the bulk ASD of the p-wave Hamiltonian and BDI, $m = 1$ to be almost identical. This does not seem to be the case, but was not fully realized until later in the project. We will come back to this matter before the end of the chapter. For now we will proceed in the hope of finding a random matrix model that matches the ASD of the p-wave Hamiltonian which is not entirely unthinkable. We will make more detailed observations of the ALDs of the p-wave Hamiltonian which are quiet general and are valuable information for further work on finding a corresponding random matrix model.

We have conducted an extensive investigation of the entire parameter space where Majorana bound states exists with both the tight binding model and the eigenmode model and compared ASDs and ALDs with BDI, $m = 1$ as well as $m = 0$ and $m = 2$. Since we only found a compelling similarity with the BDI, $m = 1$ ensemble, we have not included plots of comparison with BDI, $m = 0$ and $m = 2$.
Previously we deduced that the pairing potential Δ must be much greater than the kinetic term in the Hamiltonian, in order to have a linear energy spectrum for low energies. We have found that this happens for $m\Delta L > 15$ in the eigenmode model and for $m\Delta L > 25$ in the tight binding model. In this limit, the Hamiltonian effectively becomes a Dirac Hamiltonian consisting of a random potential term and a mass term:

$$\mathscr{H}|_{\Delta L \gg \frac{1}{2m}} = \delta\mu(x)\tau_z + \Delta p \tau_x. \tag{5.30}$$

In this limit only the relative strength between the two terms determines the shape of the ASD. The energy scale is proportional to the strength of the pairing potential Δ and inverse proportional to the length of the wire L, while the ASD is invariant to changes in the disorder amplitude V_μ, as long as the disorder strength $\gamma_\mu = V_\mu^2 a$ is constant and $a \ll L$. a is the coherence length of the disorder potential $\delta\mu(x)$, which in the tight binding model is equal to the lattice spacing. From these quantities we create a unitless ratio

$$R = \frac{\sqrt{\gamma_\mu L}}{\Delta} = \frac{V_\mu \sqrt{aL}}{\Delta}, \tag{5.31}$$

which uniquely determines the ASD in the limit $\Delta L \gg \frac{1}{2m}$, $\mu = 0$. Since only this ratio is important, we can set $L = m = 1$ without loss of generality. Searching through sets of parameters with different R-values, we have empirically located the R-value where the ASD of the p-wave Hamiltonian and the BDI, $m = 1$ ensemble have a strong similarity. We found

$$R^{\mathrm{TB}} = 3.6\,, \qquad R^{\mathrm{EIG}} = 3.2 \tag{5.32}$$

for the tight binding and eigenmode model respectively. This is a general property of the p-wave Hamiltonian that the form of the ASD is invariant under changing parameters in the limit $\Delta L \gg \frac{1}{2m}$ as long as the R-value is constant.

A simple comparison of average spectral densities for different parameters for the p-wave Hamiltonian and different random matrix ensemble will not suffice to determine if there truly is a correspondence between the p-wave Hamiltonian and a random matrix model. We need a quantitative measure of how well the density distributions agree.
Kolmogorov-Smirnov test[31]: We have the zero hypothesis that a given test sample is generated by a certain probability distribution or that two samples are generated by the same probability distribution. The Kolmogorov-Smirnov (KS) test determines if the zero hypothesis can be rejected at the chosen significance level and the corresponding p-value. The p-value is the probability of obtaining the test sample or one more extreme with the given probability

distribution we test against.
Since we are working with very large samples of data, when the KS test rejects the zero hypothesis it often returns a p-value smaller than the smallest positive double-precision float point value which is $2.2251 \cdot 10^{-308}$. This makes it difficult to compare test results of different samples to determine which is the better fit.
We therefore need another measure of how well two probability distributions agree and define the integrated absolute difference between the cumulative average level densities (IAD for short) as

$$|\delta P_j| = \int \left| \langle P_j^{\mathrm{RMT}}(E) \rangle - \langle P_j^{\mathrm{p-wave}}(E) \rangle \right| \, \mathrm{d}E, \tag{5.33}$$

where

$$\langle P_j(E) \rangle = \int_0^E \langle \rho_j(E') \rangle \, \mathrm{d}E' \tag{5.34}$$

is the cumulative average level density of the j'th eigenvalue. $|\delta P_j|$ will tend to zero if the two ALD distributions are identical.

We will use the KS-test to determine the extent of which the ASD of the p-wave Hamiltonian and a random matrix model agree and the IAD to locate the best fit among different samples.

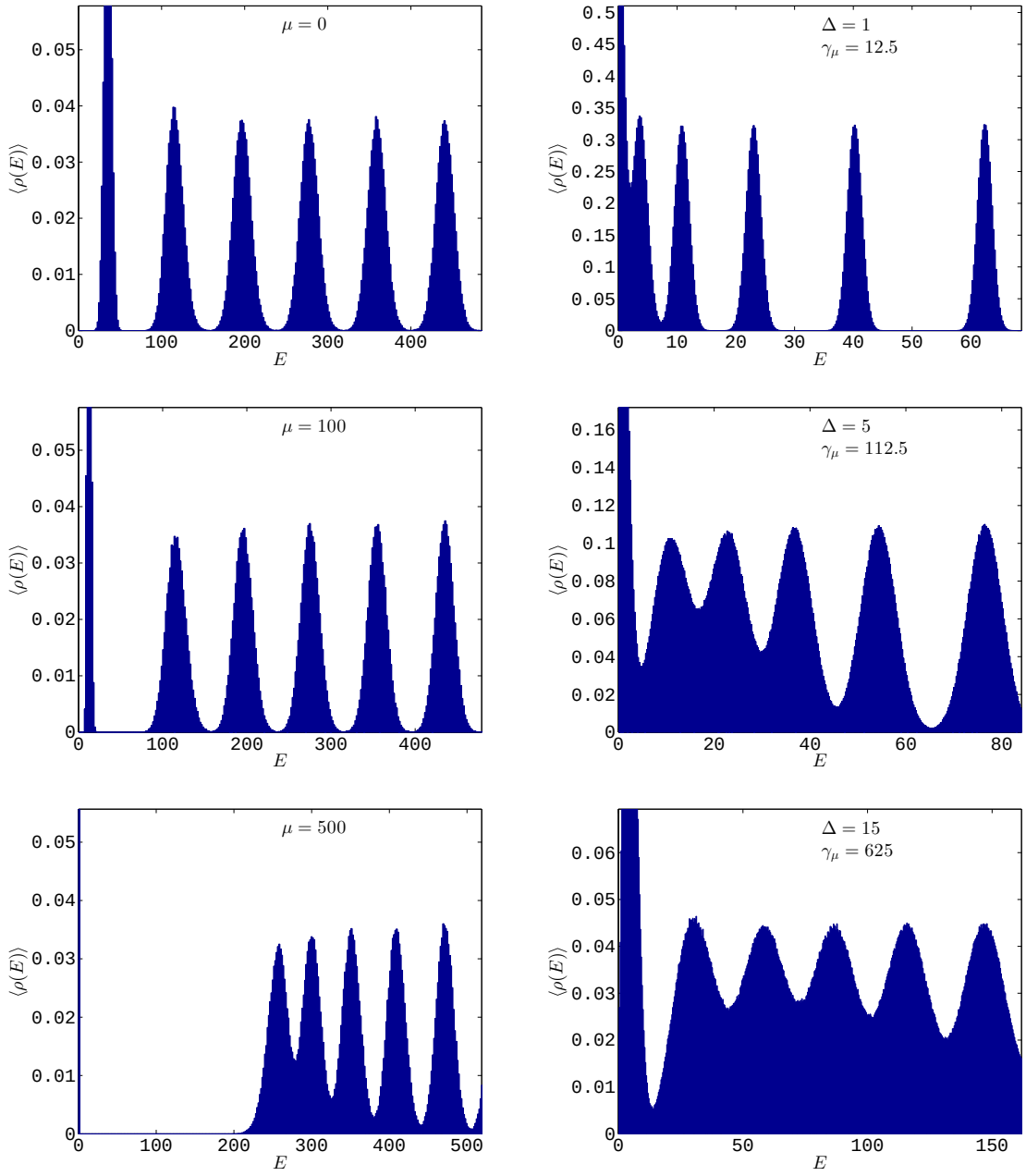

Figure 5.3: Average spectral density $\langle\rho(E)\rangle$ for different sets of parameters obtained with the eigenmode model. For all plots the wire length $L = 1$ and mass $m = 1$. For the left plots we vary μ while $\gamma_\mu = 900$, $\Delta = 50$ and computational matrix size $N = 100$ are constant. For the right plots we vary Δ and γ_μ while $\mu = 0$ and $N = 50$ are constant. Note that there is a very narrow peak at $E \approx 0$ in the lower left plot.

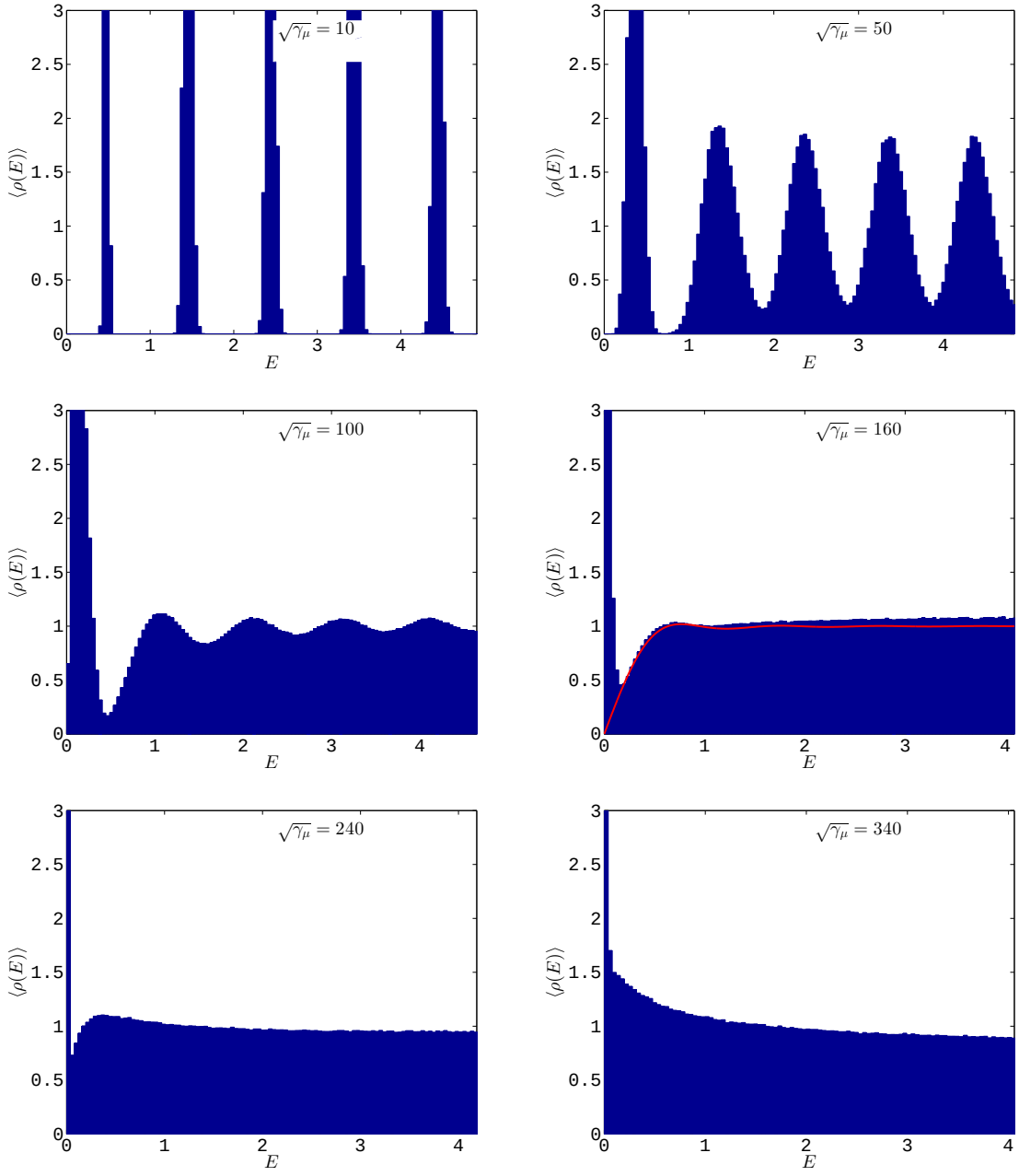

Figure 5.4: Average spectral density $\langle\rho(E)\rangle$ for different disorder strengths γ_μ computed with the eigenmode model. The analytical curve for BDI $m = 1$ (red) has been plotted alongside the data for disorder strength $\sqrt{\gamma_\mu} = 160$ where we have observed the greatest similarity. Other parameters are $L = 1$, $m = 1$, $\mu = 0$, $\Delta = 50$, scaling factor $\alpha = 96$ and computational matrix size $N = 100$.

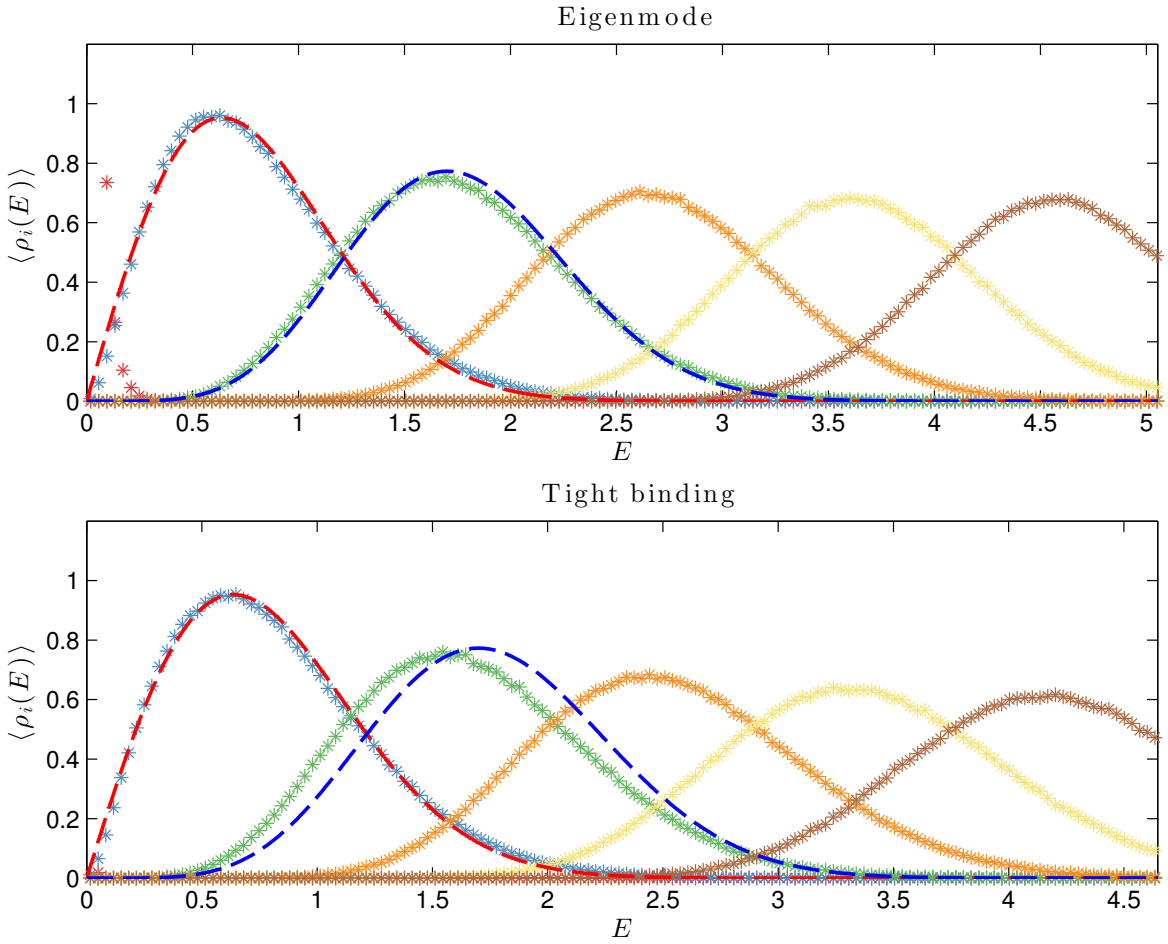

Figure 5.5: Average spectral density of individual eigenenergies for an ensemble of 10^6 disorder configurations computed by numerical diagonalization of the eigenmode and tight binding model. The parameters are wire length $L = 1$, chemical potential $\mu = 0$ and computational matrix size $N = 100$ for both plots. Eigenmode: Pairing potential $\Delta = 25$, disorder strength $\sqrt{\gamma_\mu} = 80$ and scaling factor $\alpha = 50.4$. Tight Binding: $\Delta = 100$ and $\sqrt{\gamma_\mu} = 360$ and scaling factor $\alpha = 186.4$. Analytic curves for the first (red dashed) and second (blue dashed) bulk eigenvalues of BDI $m = 1$ are given in eq. (5.28) and (5.29).

5.5 Comparing with custom random matrix model

As we have seen in the previous section, it is possible to find a set of parameters where the average spectral density of the p-wave superconductor Hamiltonian computed with the eigenmode model is almost identical to that of the random matrix ensemble BDI, $m = 1$. A fundamental difference however remains: The p-wave Hamiltonian has two eigenenergies at $\pm E_0$ close to zero, while BDI, $m = 1$ has only a single eigenvalue at exactly zero. Because of the high degree of similarity between the spectrum of the bulk eigenvalues, we believe it is possible to construct a more suitable random matrix ensemble by a slight deformation of the BDI, $m = 1$ ensemble. In this section we will test two of such ensembles against the numerically computed ASDs of the tight-binding model and the eignenmode model. We will focus on the results from the eigenmode model, since this model has shown greatest similarity with BDI, $m = 1$.

5.5.1 Model A

In section 5.3 we went through the properties of matrices of the BDI ensemble. We introduce a bit of notation in order to write the explicit matrices more compactly. The explicit form of a matrix from BDI $m = 1$ is

$$\begin{bmatrix} 0 & \cdots & 0 & W_{11} & \cdots & W_{1q} \\ \vdots & \ddots & \vdots & \vdots & \ddots & \vdots \\ 0 & \cdots & 0 & W_{p1} & \cdots & W_{pq} \\ W_{11} & \cdots & W_{p1} & 0 & \cdots & 0 \\ \vdots & \ddots & \vdots & \vdots & \ddots & \vdots \\ W_{1q} & \cdots & W_{qp} & 0 & \cdots & 0 \end{bmatrix} = \begin{bmatrix} \overline{\overline{0}}^{p\times p} & \overline{\overline{W}}^{p\times q} \\ \overline{\overline{W}}^{q\times p} & \overline{\overline{0}}^{q\times q} \end{bmatrix}, \tag{5.35}$$

where $\overline{\overline{0}}^{m\times l}$ is a $(m \times l)$-matrix of zero elements and $\overline{\overline{W}}^{p\times q} = (\overline{\overline{W}}^{q\times p})^\dagger$ is a $(p \times q)$-matrix. $|p - q| = 1$ and the elements W_{ij} are real and independently Gaussian distributed. Every matrix of this form has exactly one eigenvalue equal to zero and $n = \frac{p+q-1}{2}$ pairs of eigenvalues of $\pm E_i$, $i = 1, ..., n$. An artificial extra zero eigenvalue can be created by inserting an additional row and column in the matrix

$$H_A^a = \begin{bmatrix} \overline{\overline{0}}^{p\times p} & \overline{\overline{0}}^{p\times 1} & \overline{\overline{W}}_a^{p\times q} \\ \overline{\overline{0}}^{1\times p} & 0 & \overline{\overline{0}}^{1\times q} \\ \overline{\overline{W}}_a^{q\times p} & \overline{\overline{0}}^{q\times 1} & \overline{\overline{0}}^{q\times q} \end{bmatrix}, \tag{5.36}$$

such that H_A^a is a $(N \times N)$-matrix, where $N = q + p + 1$. This new zero eigenvalue is artificial in the sense that the corresponding eigenvector does not couple to the eigenvectors of the other eigenvalues and therefore does not change the average density spectrum of the matrix ensemble, except by adding an additional delta function of weight 1 at $E = 0$. The artificial zero eigenvalue can be coupled to the rest of the spectrum by adding a matrix from the BDI, $m = 0$ ensemble

$$H_A^b = \begin{bmatrix} \overline{\overline{0}}^{t\times t} & \overline{\overline{W}}_b^{t\times t} \\ \overline{\overline{W}}_b^{t\times t} & \overline{\overline{0}}^{t\times t} \end{bmatrix} \tag{5.37}$$

where $t = \max(p, q)$. The proposed matrix ensemble consist of matrices of the form

$$H_A = \frac{1}{\sqrt{(1-b)^2 + b^2}} \left((1-b) H_A^a + b H_A^b \right), \tag{5.38}$$

where $b \ll 1$. Matrices of this form will have $N/2$ pairs of eigenvalues $\pm E_j$, $j = 1, ..., N/2$. In the limit of interest $b \ll 1$, the bulk ASD will be almost identical to the bulk spectrum of BDI, $m = 1$, while the lowest eigenvalue has a very narrow distribution close to zero, as seen in figure 5.6b. The ALD of the lowest eigenvalue is plotted for different values of b in figure 5.10. The functional form of the ALD of the lowest eigenvalue is invariant under changing b, as seen in the right plot where a rescaling $f(x) \to \alpha^{-1} f(x\alpha)$ has brought the four curves to lie on top of each other. The ADS will be invariant under changing the matrix size, if b scales with the inverse square root of the matrix size, $b \sim \frac{1}{\sqrt{N}}$ and the width of the Gaussian distributions in eq. (5.19) scales as $v \sim \sqrt{N}$, as seen in figure 5.6a.

We use the KS test to determine the validity the zero hypothesis, that the average spectral densities of the first three eigenvalues of the RMT ensemble of model A and the first three eigenenergies of the p-wave Hamiltonian come from the same probability distribution. The data used for this test is plotted in figure 5.7. The hypothesis can be rejected at a high significance level ($< 10^{-6}$) for a wide range of parameters in both the eigenmode and tight-binding model against a range of values of b-values that gives the right amount of broadening to the lowest eigenvalue.

In order to get a more detailed picture of the difference between the random matrix model and the p-wave Hamiltonian, we consider a single set of parameters ($\Delta = 100$, $V_\mu \sqrt{a} = 340$, $N = 200$) and find the b-values with the smallest IAD. In figure 5.7 we see a comparison of the cumulative average level density, given in eq. (5.34), of the first three eigenenergies computed with the eigenmode model and RMT model A. The first and second bulk eigenenergies have similar form, as we also saw in the case of BDI, $m = 1$, but there seems to be a qualitative difference for the lowest eigenvalue close to zero. Taking a closer look at the ALD of the lowest eigenenergy reveals that it has a quite different form in the eigenmode model, compared to the tight-binding and RMT model A, as seen in figure 5.8, 5.9 and 5.10.

In figure 5.8, the ALD of the lowest energy mode has been computed using the eigenmode model for increasing computational matrix size to see if the feature was an artifact of the computational matrix size being to small. As N is increased the lowest energy mode becomes more sharply peaked close to zero, but retains its characteristic form. If this was a feature due to the N being to small the shape of the almost-zero mode ALD should change as N changes, but we see that the form is consistent. We conclude that the feature is not due to a small N, but we cannot completely rule out the possibility of the ALD will converge to a different shape in the limit of N becoming very large. We can however not explore that limit with the current model because of computational limitations.

In figure 5.9, the ALD has been computed using the tight-binding model for increasing paring potential Δ, to see if the same feature might arise in this model for large Δ. This does not happen in the examined range of Δ and is not expected to happen even for larger Δ as long as N is increased accordingly.

The ALD of the lowest eigenvalue of the RMT model A are more similar to that of the tight-binding model, than the eigenmode model. In figure 5.11 we compare the cumulative average level density of the tight-binding model to the random matrix model A. Besides the difference in the average energy difference between the bulk modes, which has been noted before, we additionally see that the ALD of the lowest energy mode has a heavier tail than

the random matrix model A. Changing b will only amount to a scaling of the curve along the E-axis and we see that this can never yield a perfect agreement with the tight-binding model since the two curves intersect.

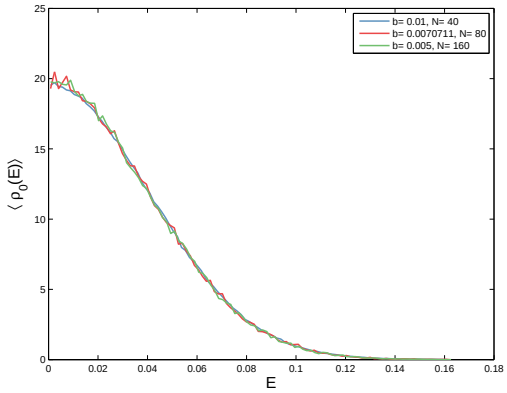

(a) Average level density of the lowest eigenvalue for different computational matrix sizes. b scales as $\frac{1}{\sqrt{N}}$ such that the ALD is invariant. Sample size is 10^6 for $N = 40$ and 10^5 for $N = 80$ and $N = 160$.

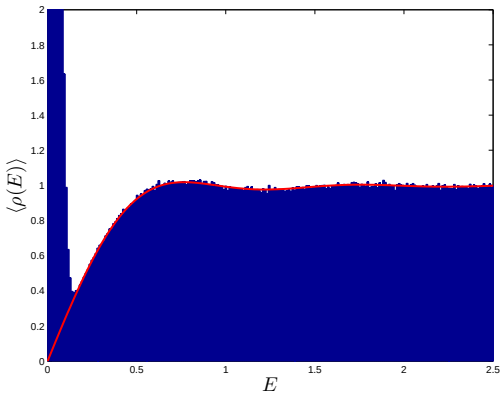

(b) Average spectral density for RMT model A. $b = 0.01$, sample size is 10^6 and computation matrix size is 42×42

Figure 5.6: Model A.

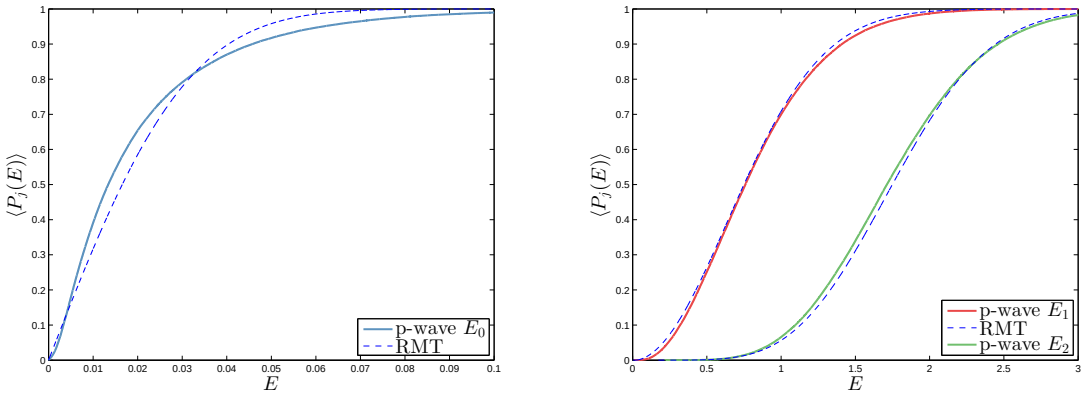

Figure 5.7: Comparing the cumulative average level density distributions of the first three eigenenergies computed with the eigenmode model and RMT model A. The lowest eigenenergy (blue) and the first (red) and second (green) bulk modes of the eigenmodel are plotted as solid lines with parameters $\Delta = 100$, $\sqrt{\gamma} = 340$, $N = 200$ of an ensemble of 10^5 disorder configurations. RMT model A with $b = 6 \times 10^{-4}$ are plotted with blue dashed lines in both plots.

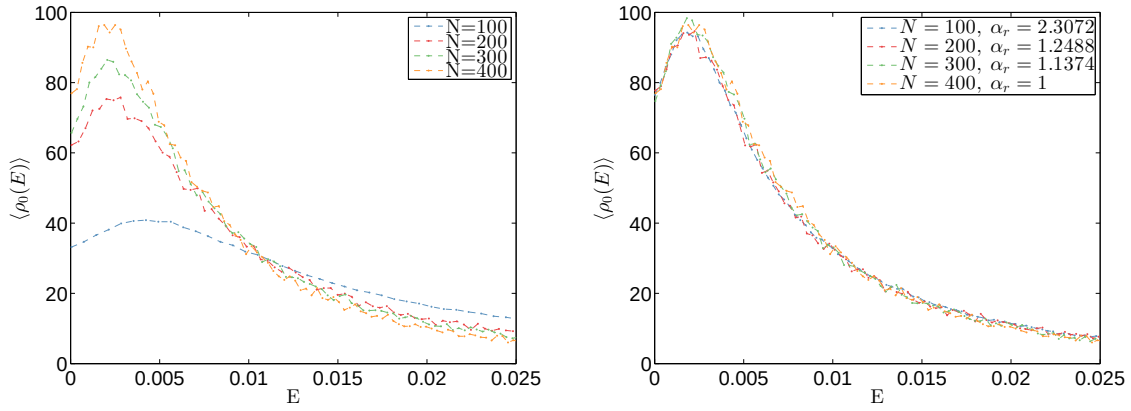

(a) (b)

Figure 5.8: Average level density distributions of the lowest eigenenergy computed with the eigenmode model for different computational matrix sizes $N = 100, 200, 400, 800$. Other parameters are $\sqrt{\gamma_\mu} = 160$, $\Delta = 50$, $\alpha = 96$. Same data is plotted in both plots, but in the right plot the data is rescaled by α_r to lie on top of each other in order to see that the functional form is the same.

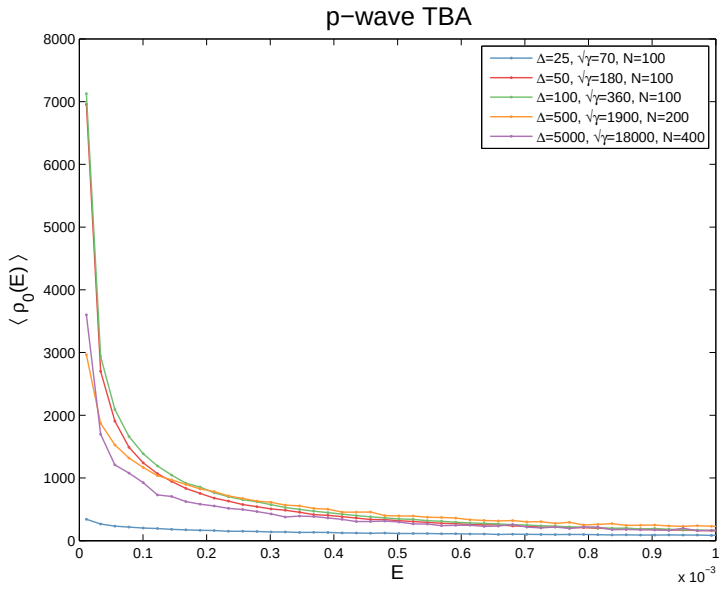

Figure 5.9: Average level density distributions of the lowest eigenenergy computed with the tight-binding model for different pairing potentials Δ . Disorder strength is set for each Δ such that the bulk spectrum is closest to the form of BDI, $m = 1$ and computational matrix size is increased for increasing Δ to ensure accurate results.

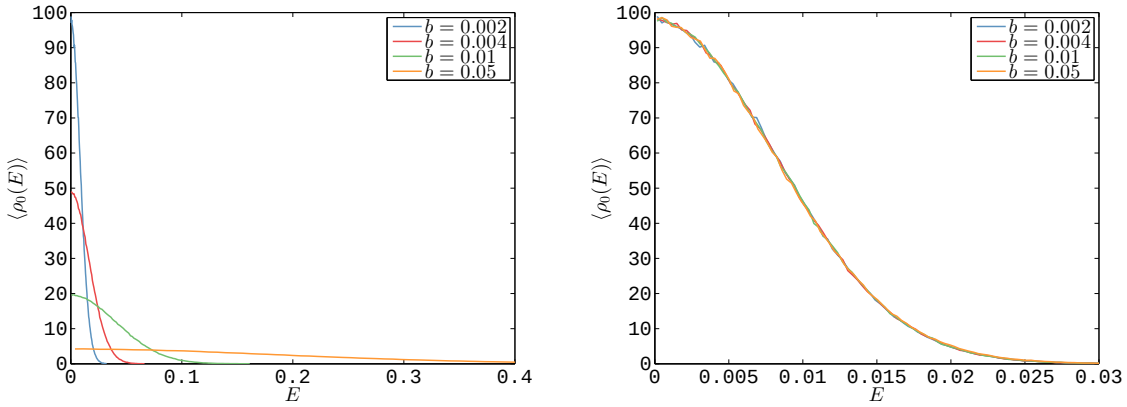

Figure 5.10: Average level density for the lowest eigenvalue in RMT model A for different values of b. The data has been rescaled in the right plot, to illustrate that the ALD has the same functional form independent of b, for $b \ll 1$. The rescaling parameter α is explained in the text.

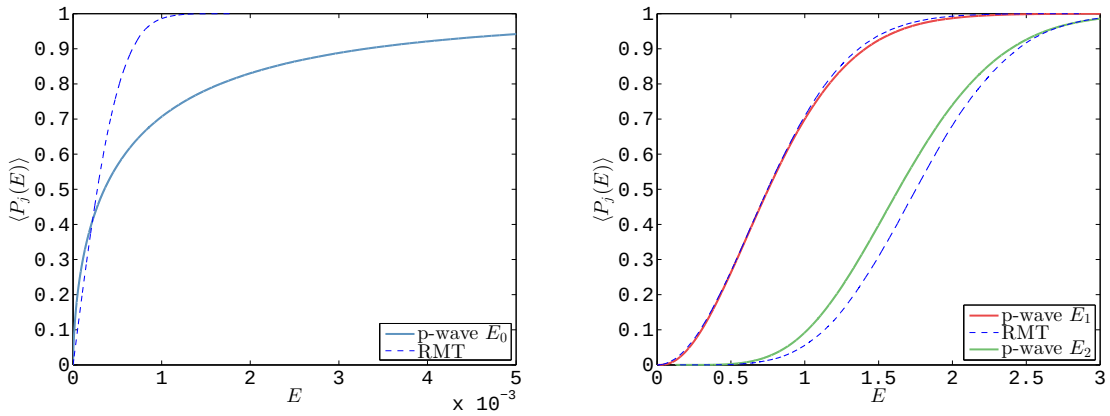

Figure 5.11: Comparing the cumulative average level density distributions of the first three eigenenergies computed with the tight-binding model and RMT model A. The lowest eigenenergy (blue) and the first (red) and second (green) bulk modes of the tight-binding model are plotted as solid lines with parameters $\Delta = 100$, $\sqrt{\gamma} = 360$, $N = 100$ of an ensemble of 10^6 disorder configurations. RMT model A with $b = 1 \times 10^{-4}$ are plotted with blue dashed lines in both plots.

5.5.2 Model B

When constructing a random matrix model where the broadening of the lowest eigenvalue ALD depends on some mixing parameter b the model must also agree with the p-wave model in the limit $b = 0$, corresponding to no mixing of the end state Majoranas. In the former model, we had to put in an extra zero mode by hand, which in the limit $b = 0$ makes it kind of artificial since it does not couple to any other mode.

Let us consider a property of eigenvectors of matrices from BDI. A property of the ensembles of BDI is that there exists a hermitian unitary matrix γ_5 which anti-commutes with all matrices in a given ensemble:

$$H\gamma_5 + \gamma_5 H = 0, \tag{5.39}$$

where H is a matrix from an ensemble of BDI. This can also be written as $\gamma_5 H \gamma_5^{-1} = -H$ and is called chiral symmetry. Let $|\psi_k\rangle$ be an eigenvector of H with eigenvalue $E_k \neq 0$:

$$H|\psi_k\rangle = E_k|\psi_k\rangle. \tag{5.40}$$

The chirality of an eigenvector is defined as its expectation value with respect to γ_5. Since H anti-commutes with γ_5 we get

$$\langle\psi_k|\gamma_5 H|\psi_k\rangle = E_k\langle\psi_k|\gamma_5|\psi_k\rangle \tag{5.41}$$

and

$$\langle\psi_k|\gamma_5 H|\psi_k\rangle = -\langle\psi_k|H\gamma_5|\psi_k\rangle = -E_k\langle\psi_k|\gamma_5|\psi_k\rangle \tag{5.42}$$

and we see that $|\psi_k\rangle$ has chirality zero or no chirality

$$\langle\psi_k|\gamma_5|\psi_k\rangle = 0. \tag{5.43}$$

This only applies when $E_k \neq 0$ and in fact[32]

$$\langle\psi_k|\gamma_5|\psi_k\rangle = \pm 1 \qquad \text{for} \qquad E_k = 0, \tag{5.44}$$

depending on whether $p < q$ or $p > q$ in eq. (5.18).

The p-wave Hamiltonian has both time reversal and particle-hole symmetry so it has also chiral symmetry (see sec. 5.1) and we would expect the Majorana mode to share the chiral properties of the zero modes of the BDI ensemble when they (the Majoranas) are exact zero modes. So in the case of a p-wave Hamiltonian with two exact zero energy Majoranas modes their wavefunctions should have chirality ± 1 and a corresponding random matrix model should share this feature.

The random matrix model A will in the limit $b = 0$ have two zero modes, but only one of them has chirality ± 1, since the other zero mode does not couple to the other modes. This model does therefore not seem like sensible model to describe the p-wave Hamiltonian.

We should then keep in mind that the almost-zero mode eigenvectors should have chirality in the limit of them becoming exact zero modes, when we construct the next random matrix model. The base of the next random matrix model will be two independent BDI, $m = 1$

matrices ensembles, with zero modes of opposite chirality. Consider the matrices

$$\begin{bmatrix} \overline{\overline{0}}^{p\times p} & \overline{\overline{W}}_a^{p\times(p+1)} \\ \overline{\overline{W}}_a^{(p+1)\times p} & \overline{\overline{0}}^{(p+1)\times(p+1)} \end{bmatrix}, \tag{5.45}$$

$$\begin{bmatrix} \overline{\overline{0}}^{(p+1)\times(p+1)} & \overline{\overline{W}}_b^{(p+1)\times p} \\ \overline{\overline{W}}_b^{p\times(p+1)} & \overline{\overline{0}}^{p\times p)} \end{bmatrix}, \tag{5.46}$$

from which we create a larger matrix

$$H_B^a = \begin{bmatrix} \ddots & \vdots & \overline{\overline{W}}_b^{p\times(p+1)} & \overline{\overline{0}}^{p\times p} \\ \cdots & \overline{\overline{0}}^{(2p+1)\times(2p+1)} & \overline{\overline{0}}^{(p+1)\times(p+1)} & \overline{\overline{W}}_a^{(p+1)\times p} \\ \overline{\overline{W}}_b^{(p+1)\times p} & \overline{\overline{0}}^{(p+1)\times(p+1)} & \overline{\overline{0}}^{(2p+1)\times(2p+1)} & \cdots \\ \overline{\overline{0}}^{p\times p} & \overline{\overline{W}}_a^{p\times(p+1)} & \vdots & \ddots \end{bmatrix}. \tag{5.47}$$

The two BDI, $m = 1$ matrices are still uncoupled in this matrix, but they can be mixed by adding a matrix H_B^b of the form

$$H_B^b = \begin{bmatrix} \overline{\overline{0}}^{(2p+1)\times(2p+1)} & \overline{\overline{M}}^{(2p+1)\times(2p+1)} \\ \left(\overline{\overline{M}}^{(2p+1)\times(2p+1)}\right)^T & \overline{\overline{0}}^{(2p+1)\times(2p+1)} \end{bmatrix}, \tag{5.48}$$

from the BDI, $m = 0$ ensemble. The model B ensemble will consist of matrices of the form

$$H_B = \frac{1}{\sqrt{(1-b)^2 + b^2}} \left((1-b)H_B^a + bH_B^b\right), \tag{5.49}$$

where $b \ll 1$. Matrices of this form will always have $2p + 1$ pairs of eigenvalues with opposite chirality sign even in the case $b = 0$ where there are two exact zero modes. In the case of $b = 0$ there is no coupling between the two matrices from BDI, $m = 1$ and as a result the bulk ASD will have twice the density, but the eigenvalues are non-degenerate. When $b > 0$, the two zero modes becomes an eigenvalues pair with eigenvalues $\pm E_0$ close to zero, while the bulk spectrum will be almost unchanged. The bulk eigenvalues should therefore be weighted by $1/2$ while the lowest eigenvalue have weight 1 in order to compare with the ASD of the p-wave Hamiltonian. In figure 5.12a we compare the model B with the analytic curve of BDI, $m = 1$. The bulk ASD keeps the same shape as BDI, $m = 1$ while the first eigenvalue is narrow distribution colse to zero. In plot 5.10 we see how the ALD of the first eigenvalue broadens for increasing values of b and by rescaling we see that the functional form is consistent for different values of b.

We compare the ALD of the first eigenvalue of model A and model B in figure 5.12b where we see that the curves are identical up to a rescaling and it is therefore possible to find a relation between the values of b in model A and the b in model B such that the ALDs are equal. The ASD of the two models is therefore equivalent and it is unnecessary to compare with the data from the p-wave Hamiltonian.

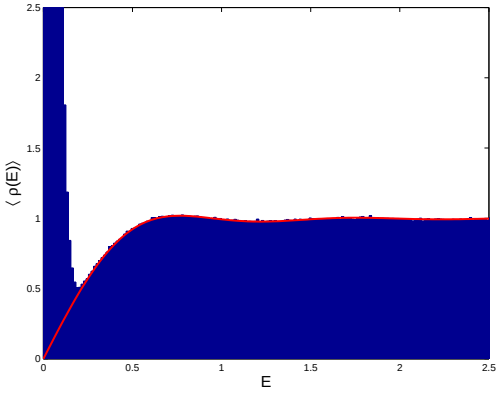

(a) Average spectral density of random matrix model B with $b = 0.01$, computational matrix size 42×42 and sample size 10^6. The analytic curve for BDI, $m = 1$ (red line) is plotted for reference

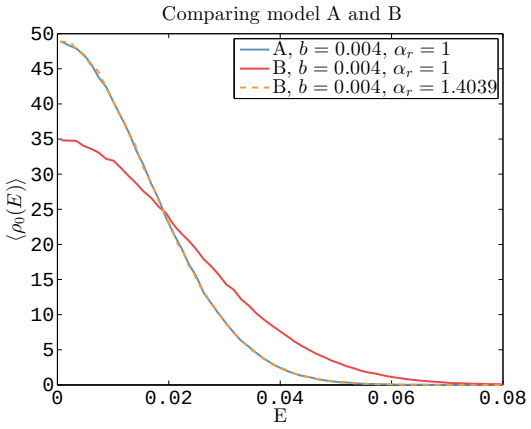

(b) Average level density of the first eigenvalue for random matrix model A and B with $b = 0.004$. Sample size is 10^6 and computational matrix size is 40×40 for model A and 42×42 for model A. The data of model B has been plotted both not rescaled (red) and rescaled (dashed yellow) to see that the curves are identical up to a rescaling.

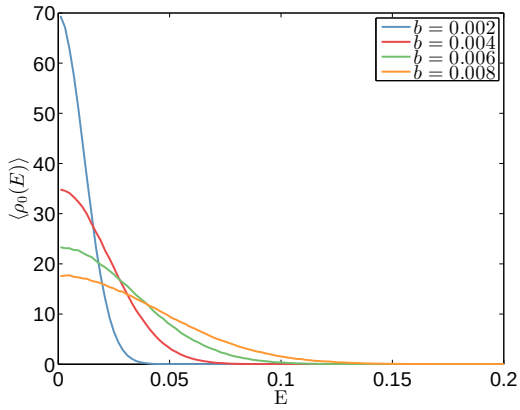

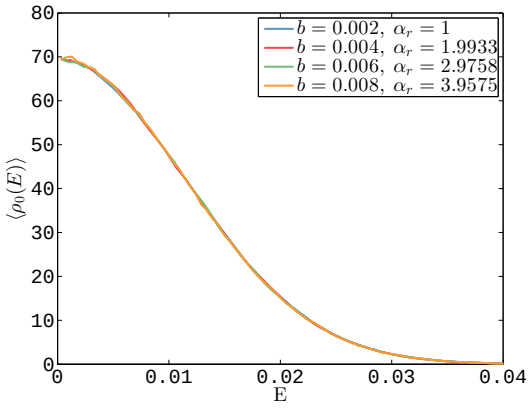

Figure 5.13: Model B. Average level density of the first eigenvalue for different values of b. Other parameters are computational matrix size 42×42 and sample size 10^6. Data is the same for both plots, but we have rescaled the data by α_r in the right plot to see that the shape of the ALD is consistent for different values of b.

5.6 Re-comparing with BDI, $m = 1$

In the previous section we designed two random matrix models and found that their ASD were in qualitative agreement with the p-wave Hamiltonian, but the agreement was not satisfactory. We now take a step back and reconsider our initial assumptions rather than constructing further models. Two assumptions we made are: One that the distorted zero energy mode repels the bulk modes the same way as the exact zero mode of BDI, $m = 1$ do, and two that the average distance between the lowest bulk modes of the p-wave Hamiltonian are equidistant. We examine the validity of the second assumption first.

We build the second assumption on the observation that if $\Delta L \gg \frac{1}{2m}$, the energy spectrum is linear close to zero as seen in figure 5.3. We check this assumption by plotting the average distance between energy levels also called the interlevel distance for increasing values of Δ while the disorder strength is fixed such that the ASD is similar to BDI, $m = 1$. In figure 5.14 we plot the average distance between the first 9 bulk modes for different values of pairing potential along data from numerical simulations of the BDI, $m = 1$ ensemble. The average distance between bulk modes is normalized by the average distance between the two first bulk modes:

$$\delta E_i = \frac{\langle E_{i+1} - E_i \rangle}{\langle E_2 - E_1 \rangle}, \tag{5.50}$$

where $\langle E_{i+1} - E_i \rangle$ is the mean of the distance between the $(i + 1)$'th and the i'th energy eigenvalue of the p-wave Hamiltonian obtained by the eigenmode model or the tight binding model.
Contrary to our assumption, the average distance between bulk modes does not converge towards a constant interlevel distance as Δ is increased. Instead the interlevel distance decreases as we go from lower to higher bulk modes when Δ is larger than ≈ 15. For $\Delta \geq 100$ the relative interlevel distance seems to be consistent as data points for larger values of Δ lie roughly on top of each other. The data of the RMT ensemble BDI, $m = 1$ has been plotted for comparison and we see that the interlevel distance is 1 except for the distance between the first and second bulk mode which is a bit smaller. A corresponding random matrix model must exhibit the same interlevel distance at least for the first few eigenvalues as observed for the p-wave models.

The other assumption was that the distorted almost-zero energy mode of the p-wave Hamiltonian repels the bulk modes the same way as the exact zero mode of the BDI, $m = 1$ ensemble. If this assumption is false, the ALD of the bulk modes might be distorted compared to the bulk states of BDI, $m = 1$. However, if only the repulsion between the distorted almost-zero mode and the first bulk mode is different from the BDI, $m = 1$ ensemble while the repulsion between the other bulk modes is the same, the bulk modes beyond the first bulk mode should not be distorted significantly. If that is the case, we expect to find a greater similarity between the ALDs of the p-wave Hamiltonian and the BDI, $m = 1$ ensemble for bulk modes beyond the first bulk mode.

In figure 5.15 we plot the ALD of the p-wave models which have been rescaled such that the average of the distances between the second to sixth bulk modes is equal to 1. We fit the analytical expression for the second bulk mode of BDI $m = 1$ by making a shift of the analytical curve along the E-axis. The analytical curve for the first bulk mode has been plotted to see the distortion of the ALD of the first bulk mode. Explicitly the data of the

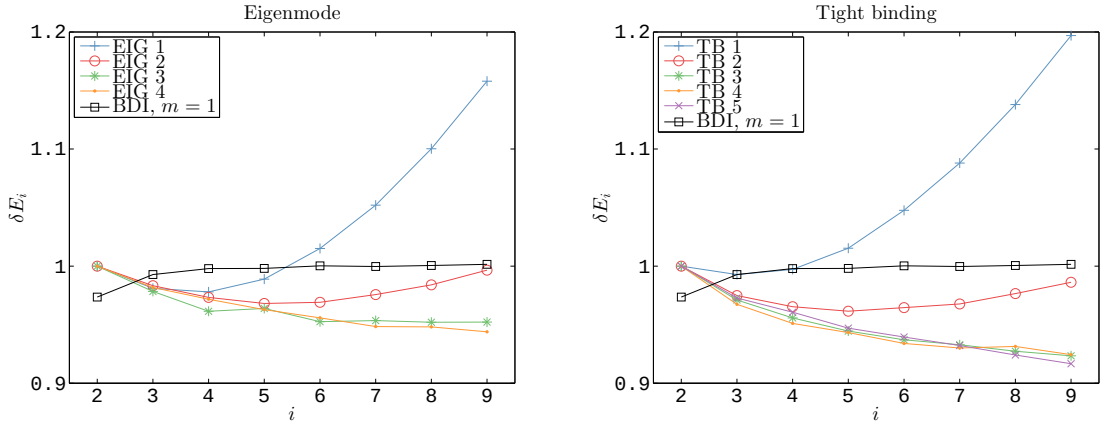

Figure 5.14: Average distance between the first 9 bulk modes for different values of Δ and γ_μ with approximately the ratios $R^{\mathrm{TB}} = 2.6$ and $R^{\mathrm{EIG}} = 2.75$ which are defined in eq. (5.31). Parameters for the data sets EIG and TB are listed in table 5.3 and the data of BDI, $m = 1$ is obtained by numerical simulations of a random matrix ensemble with $N = 100$ and sample size 10^6 matrices. The one standard deviation uncertainty on each data point is of the order 10^{-3}. δE_i on the y-axis is defined in eq. (5.50).

Eigenmode					Tight binding				
legend	Δ	$\sqrt{\gamma_\mu}$	N	sample size	legend	Δ	$\sqrt{\gamma_\mu}$	N	sample size
EIG 1	25	65	100	10^6	TB 1	25	70	100	10^6
EIG 2	50	138	100	10^6	TB 2	50	130	100	10^6
EIG 3	100	276	200	10^5	TB 3	100	260	100	10^6
EIG 4	500	1400	400	10^5	TB 4	500	1300	400	10^5
					TB 5	5000	13000	400	10^5

Table 5.3: Table of parameters used for the plots in figure 5.14.

p-wave Hamiltonian has been rescaled such that

$$\frac{1}{4}\sum_{i=2}^{6}\langle E_{i+1} - E_i\rangle = 1, \tag{5.51}$$

where $\langle E_{i+1} - E_i\rangle$ is the mean of the distance between the $(i+1)$'th and the i'th energy eigenvalue.

It is clear from figure 5.15 that the ALD of the first bulk mode of the p-wave Hamiltonian does not match the ALD of the first bulk mode of the BDI, $m = 1$ ensemble, but there is an overwhelming similarity between the ALDs of the second bulk mode. A comparison of higher bulk modes is needed in order to determine if only the first bulk mode is distorted, but at the present we lack the analytical expressions for higher bulk mode. We do though believe that there will be the same functional agreement as seen with the second bulk mode, but the interlevel distance will be different from the BDI, $m = 1$ as we saw in figure 5.14.

Even though we have now shown that our former assumptions do not hold, we have also gained further knowledge about the ASD of the p-wave Hamiltonian. One being how the interlevel distance between bulk modes of the p-wave Hamiltonian is not constant but instead decreases going from first bulk modes upwards. Two being that the distorted almost-zero energy mode repels the bulk modes in a different way than the exact zero mode of BDI, $m = 1$, and this leads to a deformation of the ALD of the first bulk mode of the p-wave Hamiltonian as compared to the first bulk mode of BDI, $m = 1$. Three that the ALD of the second and possibly higher bulk modes agree with the functional form of the ALD of the BDI, $m = 1$ ensemble, but that the interlevel distance is different.

These observations will be important in the design of a random matrix ensemble corresponding to the p-wave Hamiltonian if a random matrix ensemble with these properties exists. Time is however a limited resource, and we therefore have to discontinue our pursuit of the random matrix model.

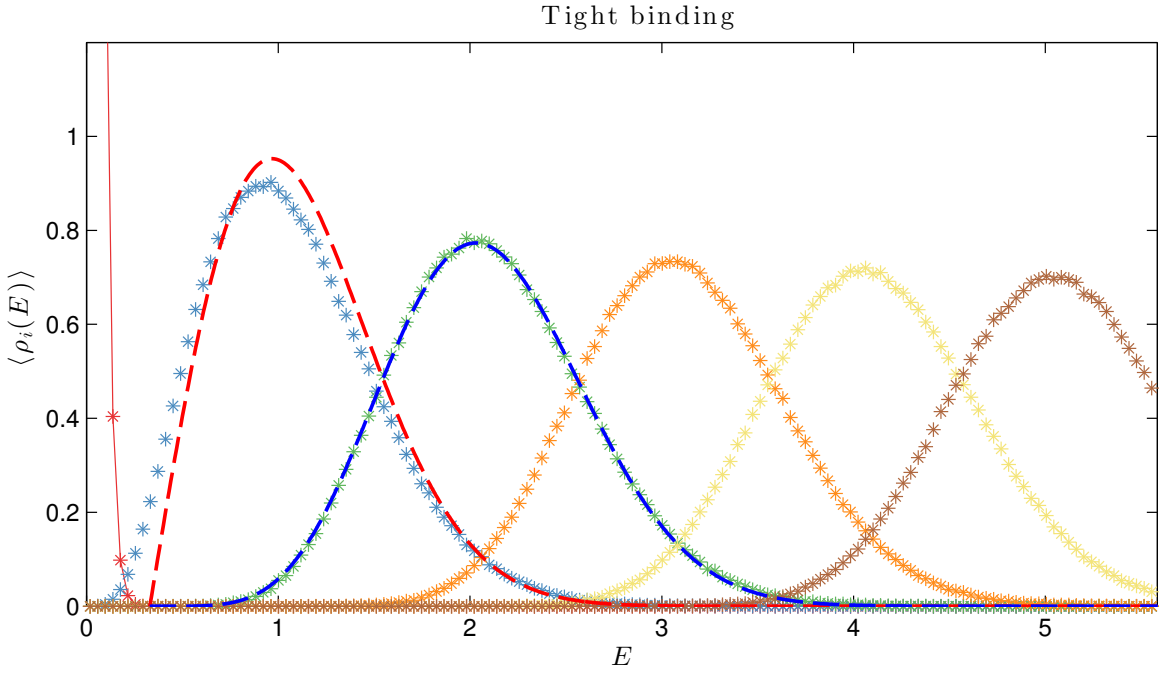

(a) Samplesize is 10^6 disorder configurations, computational matrix size $N = 100$, and disorder strength $\sqrt{\gamma} = 260$. The anaytical curves of BDI $m = 1$ has been shifted $E_{\text{shift}} = 0.33$ along the E-axis.

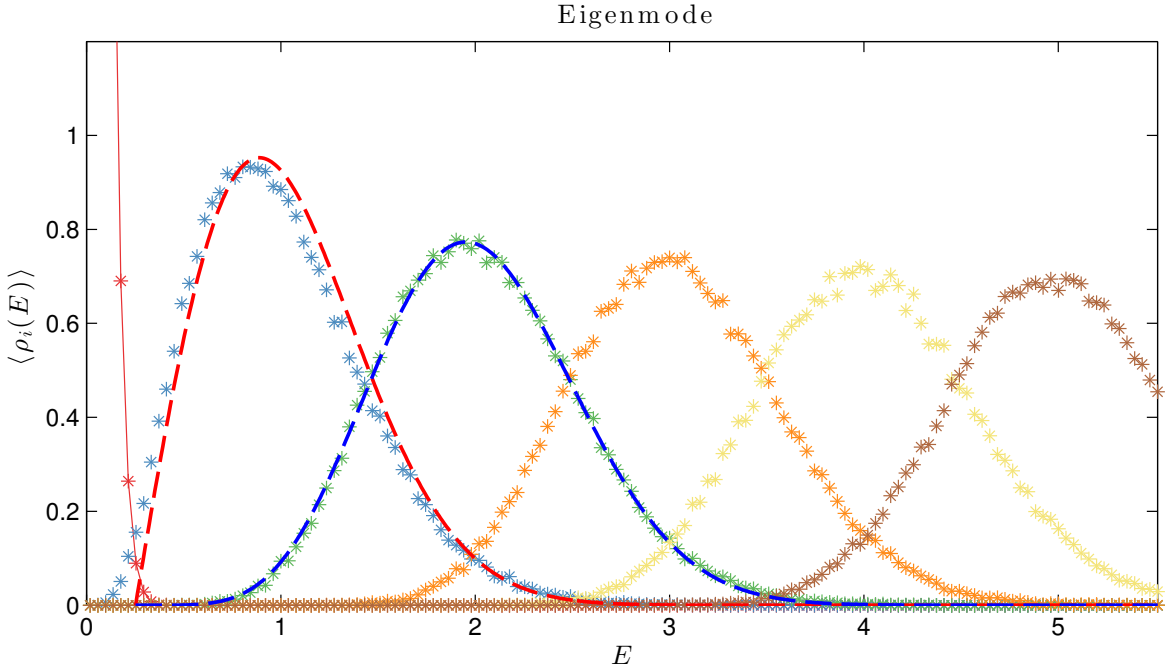

(b) Samplesize is 10^5 disorder configurations, computational matrix size $N = 200$ and disorder strength $\sqrt{\gamma} = 276$. The anaytical curves of BDI $m = 1$ has been shifted $E_{\text{shift}} = 0.25$ along the E-axis.

Figure 5.15: Average level densities of individual energy eigenvalues computed by numerical diagonalization of the eigenmode and tight binding model. The parameters are wire length $L = 1$, $\Delta = 100$, chemical potential $\mu = 0$ for both plot. Analytic curves for the first (red dashed) and second (blue dashed) bulk eigenvalues of BDI $m = 1$ (eq. (5.28) and (5.29)) have been shifted E_{shift} along the E-axis.

Chapter 6

Concluding remarks

6.1 Summary

In this thesis we have shown that the 1D p-wave Hamiltonian model is an effective low-energy model of the semiconductor-superconductor device of a quantum wire with strong spin-orbit coupling and induced s-wave superconductor pairing and subject to a magnetic field. The p-wave Hamiltonian model has two topologically distinct phases, and the topological non-trivial phases exhibit unpaired zero energy Majorana bound end states. This is shown for both a continuous Hamiltonian model and a tight binding Hamiltonian.
Two numerical models were introduced to describe the p-wave Hamiltonian model: The tight binding model and the eigenmode model. Both models were consistent with the theoretical prediction of the Majorana end mode energy dependence on wire length by Kitaev[11].
Next we introduced two models of disorder in the system, a random chemical potential disorder model and a random pairing potential disorder model, and we implemented the disorder in the numerical models. It was seen for the tight binding model that the chemical potential disorder changed the Majorana energy dependence on wire length in accordance with the findings of Brouwer et. al. [23]. Numerical computations of the Majorana end state and first bulk state energies for increasing chemical disorder strength showed that the energy gap closes at a critical disorder strength of the same order as predicted in [23]. It was also observed that increasing the pairing potential disorder strength closes the superconducting energy gap around the Majorana end state.

In chapter 5 we showed that the p-wave Hamiltonian model belongs to the universal symmetry class BDI. The average spectral density of the two numerical models were examined for a wide range of parameters in the search of a domain where it is possible to construct a simple corresponding random matrix model. The average spectral densities of the p-wave Hamiltonian and the random matrix ensemble BDI, $m = 1$ where compared, and a large degree of similarity was observed for a certain domain of parameters. The similarities are sufficiently convincing that we believe it is possible to construct a corresponding random matrix model.
Two random matrix models were introduced in the attempt of establishing a corresponding random matrix model to the p-wave Hamiltonian, but both were only partially successful. Further details about the average spectral density of the p-wave Hamiltonian were found on a second comparison with the BDI, $m = 1$ ensemble. These details might be useful in the future search for a random matrix model corresponding to the p-wave Hamiltonian.

6.2 Outlook

Even though we were not able to present a perfectly equivalent random matrix model to the numerical disordered p-wave Hamiltonian model description of the Majorana modes in this thesis, the matter has not been thoroughly investigated to the extent that the existence of such a random matrix model can be ruled out. Given the extensive similarities between the average spectral densities of the p-wave Hamiltonian and the considered random matrix models, it seems very likely that such a random matrix model can be constructed. Given more time, we would proceed with the following.

The first thing would be to investigate the possibility of constructing a random matrix model with the same properties as those found for the p-wave Hamiltonian in section 5.6. If it proved possible to find a corresponding random matrix model in this rather restricted domain of parameter space, we would then attempt to extent this domain by implementing a gap around the almost-zero mode in the average spectral density of the random matrix model. If such a random matrix model can be found, it is our hope that it is possible to obtain analytical results regarding the Majorana modes.

Through the work of this thesis we have gained a great deal of understanding of the dynamics of the Majorana modes in the p-wave Hamiltonian and the similarities between average spectral densities of the p-wave Hamiltonian and the BDI, $m = 1$ ensemble. The p-wave Hamiltonian was introduced as an effective low-energy model of the more complicated Hamiltonian model of the quantum wire with strong spin-orbit coupling and induced s-wave superconductor pairing and subject to a magnetic field. The methods used in this thesis is applicable to other Hamiltonians, and it would also be very interesting to investigate the possibility of finding a corresponding random matrix model to the more complex Hamiltonian in eq. (1.10).

In this thesis, we have worked on the disordered p-wave superconductor model as an isolated system and investigated the dynamics of the energy eigenvalues through numerical diagonalization of a Hamiltonian model. Another approach is the use of transfer matrices or scattering matrices which have already been used extensively in the study of Majorana bound states in topological systems in recent years [33, 17, 23]. Investigating the possibility of an equivalent random matrix description to these models would also be an interesting pursuit.

Bibliography

[1] A.Yu. Kitaev. Fault-tolerant quantum computation by anyons. *Annals of Physics*, 303(1):2 – 30, 2003.

[2] Frank Wilczek. Quantum mechanics of fractional-spin particles. *Phys. Rev. Lett.*, 49:957–959, Oct 1982.

[3] Frank Wilczek. Majorana returns. *Nature Physics*, 5(9):614–618, September 2009.

[4] Martin Leijnse and Karsten Flensberg. Introduction to topological superconductivity and Majorana fermions. *Semiconductor Science and Technology*, 27(12):124003, December 2012.

[5] Chetan Nayak, Steven H. Simon, Ady Stern, Michael Freedman, and Sankar Das Sarma. Non-abelian anyons and topological quantum computation. *Rev. Mod. Phys.*, 80:1083–1159, Sep 2008.

[6] Alexander Altland and Martin R. Zirnbauer. Nonstandard symmetry classes in mesoscopic normal-superconducting hybrid structures. *Phys. Rev. B*, 55:1142–1161, Jan 1997.

[7] Martin R. Zirnbauer. Riemannian symmetric superspaces and their origin in random matrix theory. *Journal of Mathematical Physics*, 37(10):4986–5018, 1996.

[8] Andreas P. Schnyder, Shinsei Ryu, Akira Furusaki, and Andreas W. W. Ludwig. Classification of topological insulators and superconductors in three spatial dimensions. *Phys. Rev. B*, 78:195125, Nov 2008.

[9] Liang Fu and C. L. Kane. Superconducting proximity effect and majorana fermions at the surface of a topological insulator. *Phys. Rev. Lett.*, 100:096407, Mar 2008.

[10] D. A. Ivanov. Non-abelian statistics of half-quantum vortices in p-wave superconductors. *Phys. Rev. Lett.*, 86:268–271, Jan 2001.

[11] A Yu Kitaev. Unpaired majorana fermions in quantum wires. *Physics-Uspekhi*, 44(10S):131, 2001.

[12] Jason Alicea, Yuval Oreg, Gil Refael, Felix von Oppen, and Matthew P. a. Fisher. Non-Abelian statistics and topological quantum information processing in 1D wire networks. *Nature Physics*, 7(5):412–417, February 2011.

[13] Yuval Oreg, Gil Refael, and Felix von Oppen. Helical liquids and majorana bound states in quantum wires. *Phys. Rev. Lett.*, 105:177002, Oct 2010.

[14] Jay D. Sau and S. Das Sarma. Density of states of disordered topological superconductor-semiconductor hybrid nanowires. *Phys. Rev. B*, 88:064506, Aug 2013.

[15] V. Mourik, K. Zuo, S. M. Frolov, S. R. Plissard, E. P. A. M. Bakkers, and L. P. Kouwenhoven. Signatures of majorana fermions in hybrid superconductor-semiconductor nanowire devices. *Science*, 336(6084):1003–1007, 2012.

[16] Olexei Motrunich, Kedar Damle, and David Huse. Griffiths effects and quantum critical points in dirty superconductors without spin-rotation invariance: One-dimensional examples. *Physical Review B*, 63(22):224204, May 2001.

[17] C. W. J. Beenakker. Random-matrix theory of Majorana fermions and topological superconductors. *ArXiv e-prints*, July 2014.

[18] Madan Lal Mehta. *Random Matrices, 3rd Ed.* 2004.

[19] Shun-Qing Shen. *Topological Insulators.* 2012.

[20] Piet W. Brouwer, Mathias Duckheim, Alessandro Romito, and Felix von Oppen. Topological superconducting phases in disordered quantum wires with strong spin-orbit coupling. *Physical Review B*, 84(14):144526, October 2011.

[21] Mathias Duckheim and Piet W. Brouwer. Andreev reflection from noncentrosymmetric superconductors and majorana bound-state generation in half-metallic ferromagnets. *Phys. Rev. B*, 83:054513, Feb 2011.

[22] H. Bruus and K. Flensberg. *Many body quantum theory in condenced matter physics, an introduction.* 2004.

[23] Piet W. Brouwer, Mathias Duckheim, Alessandro Romito, and Felix von Oppen. Probability distribution of majorana end-state energies in disordered wires. *Phys. Rev. Lett.*, 107:196804, Nov 2011.

[24] B Kramer and A MacKinnon. Localization: theory and experiment. *Reports on Progress in Physics*, 56(12):1469, 1993.

[25] D. A. Ivanov. The supersymmetric technique for random-matrix ensembles with zero eigenvalues. *Journal of Mathematical Physics*, 43(1):126–153, 2002.

[26] Poul H. Damgaard and Shinsuke M. Nishigaki. Distribution of the kth smallest dirac operator eigenvalue. *Phys. Rev. D*, 63:045012, Jan 2001.

[27] D. Bernard and A. LeClair. A classification of 2d random dirac fermions. *Journal of Physics A: Mathematical and General*, 35(11):2555, 2002.

[28] G. Akemann, P.H. Damgaard, U. Magnea, and S. Nishigaki. Universality of random matrices in the microscopic limit and the dirac operator spectrum. *Nuclear Physics B*, 487(3):721 – 738, 1997.

[29] G. Akemann, P.H. Damgaard, U. Magnea, and S.M. Nishigaki. Multicritical microscopic spectral correlators of hermitian and complex matrices. *Nuclear Physics B*, 519(3):682 – 714, 1998.

[30] Milton Abramowitz and Irene A. Stegun. *Handbook of Mathematical Functions*. 1972.

[31] Roger Barlow. *Statistics, A Guide to the Use of Statistical Methods in the Physical Sciences*. 1989.

[32] G. Akemann, P. H. Damgaard, K. Splittorff, and J. J. M. Verbaarschot. Spectrum of the wilson dirac operator at finite lattice spacings. *Phys. Rev. D*, 83:085014, Apr 2011.

[33] Wade DeGottardi, Diptiman Sen, and Smitha Vishveshwara. Topological phases, majorana modes and quench dynamics in a spin ladder system. *New Journal of Physics*, 13(6):065028, 2011.